This electronic thesis or dissertation has been downloaded from Explore Bristol Research, http://research-information.bristol.ac.uk

Author:
Hedges, Jade A J

Title:
Investigating synaptic tau localisation in neurodegeneration using Expansion Microscopy

Investigating synaptic tau localisation in neurodegeneration using Expansion Microscopy

Jade Hedges

University of Bristol

A dissertation submitted to the University of Bristol in accordance with the requirements for award of the degree of *Master of Science by Research* in the Faculty of Life Sciences

September 2021

Word Count: 18,902

Declaration

I declare that the work in this dissertation was carried out in accordance with the requirements of the University's *Regulations and Code of Practice for Research Degree Programmes* and that it has not been submitted for any other academic award. Except where indicated by specific reference in the text, the work is the candidate's own work. Work done in collaboration with, or with the assistance of, others, is indicated as such. Any views expressed in the dissertation are those of the author.

SIGNED: Jade Hedges   DATE: 01/09/21

Acknowledgements

I would like to thank my supervisor, Dr Mike Ashby, for the invaluable support and guidance I have received whilst undertaking this project. Not only have I been able to develop my understanding and continue pursuing my passion for science and research, but I have been extremely lucky to do so in the great company of the Ashby Lab. Everyone that I have benefitted from working with this year have been supportive, and their hard work and expertise is inspiring.

I couldn't complete a research degree without acknowledging my best bud, Erin, a fantastic anatomist and the OG lab partner. Finally, thank you to my no. 1 fan, Oliver, who has provided and toiled this year to support me and this work. You're the best.

Abstract

Tauopathies are a class of neurodegenerative diseases characterised by the progressive accumulation of misfolded tau protein into neurofibrillary tangles (NFTs). The dissociation of tau from microtubules disrupts axonal transport whilst intracellular NFTs displace organelles resulting in cell death. Evidence from mouse tauopathy models (i.e. rTg4510) indicate that prior to substantial NFT accumulation, tau is mislocated to synapses. This correlates temporally with an early disruption to synaptic function in rTg4510 mice, and it has been hypothesised that synaptic tau presence could contribute to the early synapse loss that occurs in tauopathy-driven neurodegeneration.

Previous studies aiming to resolve pathological tau at dendritic spines have been limited by light resolution. However, in recent years, a new technique, Expansion Microscopy (ExM), has been established by which fixed tissue and cell samples can be physically expanded 4.0-4.5 fold to enable imaging of subcellular structures probed with fluorophores on conventional light microscopes.

Here, Protein Retention Expansion Microscopy (ProExM) has been optimised and applied to fixed brain tissue slices from 4-month-old rTg4510 mice, with the purpose of increasing the resolution of cell ultrastructure so that tau fibrils at synapses could be identified. rTg4510 fixed tissue was immunolabelled for tau and synaptic markers and expanded via ProExM. It was shown that ExM is effective in increasing the resolution of molecular tau fibrils. In addition, tau fibrils were localised to some putative synapses however these findings were still limited by resolution.

The full potential of ExM has not yet been fully realised, and future studies could utilise updated ExM protocols with higher expansion factors to further improve the resolution of synaptic tau. By identifying synaptic tau presence in mouse models of neurodegeneration, the relationship between mislocated synaptic tau and the disruption of synaptic function early in tauopathies could be elucidated.

Word count: 291

Table of contents

List of figures

List of tables

Abbreviations

(p)tau	phosphorylated tau
4HT	4-Hydroxy-TEMPO
AcX	6-((acryloyl)amino)hexanoic acid
AD	Alzheimer's disease
ADDL	amyloid-beta derived diffusible ligands
ALS	amyotrophic lateral sclerosis
AMPA	α-amino-3-hydroxy-5-methyl-4-isoxazolepropionic acid
ANOVA	analysis of variance
AP	action potential
APP	Amyloid precursor protein
APS	ammonium persulfate
Aβ	Amyloid β
BACE1	beta-site amyloid precursor protein cleaving enzyme 1
CaMKIIα	Calcium/calmodulin-dependent protein kinase IIα
cDNA	complementary DNA
CSF	cerebrospinal fluid
DAPI	4′,6-diamidino-2-phenylindole
DMSO	Dimethyl sulfoxide
Dox	doxycycline
DT	digestion time
EDTA	ethylenediaminetetraacetic acid
EM	electron microscopy

ExM	Expansion Microscopy
F-actin	filamentous actin
FDG PET	fludeoxyglucose positron emission tomography
FTDP-17	frontotemporal dementia with parkinsonism linked to chromosome 17
GFP	green fluorescent protein
GluA1	glutamate receptor 1
htau	human tau
iExM	Iterative Expansion Microscopy
IHC	immunohistochemistry
iRFP	Near-infrared fluorescent protein
LM	light microscopy
LTD	long term depression
MAP	microtubule associated protein
MAP2	Microtubule-associated protein 2
MAPT	microtubule associated protein tau
MND	motor neuron disease
mppv	minimum peak prominence value
MRI	magnetic resonance imaging
NaCl	sodium chloride
NFT	neurofibrillary tangle
NMDA	N-Methyl-D-aspartic acid or N-Methyl-D-aspartate
NMDAR	N-Methyl-D-aspartic acid or N-Methyl-D-aspartate receptor
NT	non-transgenic

PALM   Photoactivated Localization Microscopy

PART   primary age-related tauopathy

PBS   phosphate buffered saline

PET   positron emission tomography

PFA   paraformaldehyde

PFC   prefrontal cortex

PHF   paired helical filaments

ProExM   Protein Retention Expansion Microscopy

rpm   rotations per minute

RT   room temperature

SD   standard deviation

SEM   standard error of the mean

ShRNA   short hairpin RNA

SIM   Structured Illumination Microscopy

SRLM   super resolution light microscopy

SSC   somatosensory cortex

STED   Stimulated emission depletion microscopy

STORM   Stochastic Optical Reconstruction Microscopy

TEMED   tetramethylethylenediamine

TG   transgenic

TO-PRO-3   TO-PRO™-3 Iodide

TRE   tetracycline responsive element

TREx   Ten-fold Robust Expansion Microscopy

tTA   tetracycline-controlled transactivator

U-ExM   Ultra-Expansion Microscopy

vGlut1   Vesicular glutamate transporter 1

WT   wildtype

X10   x10 expansion microscopy

YFP   yellow fluorescent protein

1. Introduction

1.1. Neurodegenerative diseases

Neurodegenerative diseases are characterised by the progressive loss of central nervous system structure and function, typically a loss of selectively vulnerable populations of neurons (Agrawal et al, 2015; Dugger & Dickson, 2017). This heterogenous class of diseases share common features including pathological protein misfolding and aggregation, cell loss and tissue atrophy, and progressive cognitive impairment (Ross & Poirier, 2004; Wilson et al, 2010).

Examples of neurodegenerative diseases include Alzheimer's disease (AD) and other dementias, Parkinson's disease, amyotrophic lateral sclerosis (ALS) and motor neuron disease (MND). The incidence of many neurodegenerative diseases increases significantly with age, and therefore prevalence within the population has continued to rise with increasing life expectancy (Hou et al, 2019). Currently ~50 million individuals are living with dementia worldwide, and this is projected to increase to 131.5 million by 2050 (Hansson et al, 2021; Prince, 2015). This comes at a significant societal cost; in England, average costs of mild, moderate, and severe dementia care are £24400, £27450, and £46050, respectively, per person per year (Wittenberg et al, 2019).

1.2. Tauopathies

Tauopathies are a group of progressive neurodegenerative diseases characterised by tau-positive deposits in the brain (Orr et al, 2017). Such diseases included AD, primary age-related tauopathy (PART), frontotemporal dementia with parkinsonism linked to chromosome 17 (FTDP-17) and Pick disease (Arendt et al, 2016).

1.2.1. Physiological functions of tau

Humans express six isoforms of tau proteins as a result of alternative splicing of the MAPT gene located on chromosome 17q21 (Goedert et al, 1989; Neve et al, 1986). Tau functions primarily as a microtubule associated protein (MAP) in the axons of neurons where it stabilises microtubules and regulates microtubule dynamics such as assembly and spatial organisation (Weingarten et al, 1975; Binder et al, 1985; Black et al, 1996; Barbier et al, 2019). Under normal conditions, the binding affinity of tau to microtubules is regulated in part by phosphorylation of different residues via kinase/phosphatase activity (Ding et al, 2006).

Endogenous tau in mice has also been localised to dendrites and dendritic spines, and has been implicated here in additional physiological functions such as the targeting of Fyn, a Src kinase, to the post-synapse where it regulates NMDA receptor (NMDAR) function via

GluN2B subunit phosphorylation (Ittner et al, 2010) and the regulation of postsynaptic long-term depression (LTD) *in vitro* and *in vivo* (Kimura et al, 2013).

1.2.2. Tau-mediated pathology

1.2.2.1. Hyperphosphorylation, dissociation and aggregation

Pathological aggregates of tau proteins form due to the hyperphosphorylation of tau and subsequent dissociation from microtubules (Figure 1.1) (Ittner & Ittner, 2018). Hyperphosphorylation of tau depends on dysregulated kinase and phosphatase activity, which in turn are influenced by local environment, molecular chaperones, and cell stress (Figure 1.1) (Spires-Jones et al, 2009; Ittner & Ittner, 2018). Phosphorylation at Ser-262 localised in the first repeat domain of tau in particular is thought to be an early event in the progressive pathological phosphorylation of tau at other sites (hyperphosphorylation) (Schwalbe et al, 2013). Hyperphosphorylation of tau reduces the binding affinity to microtubules resulting in increased unbound tau (Spires-Jones et al, 2009).
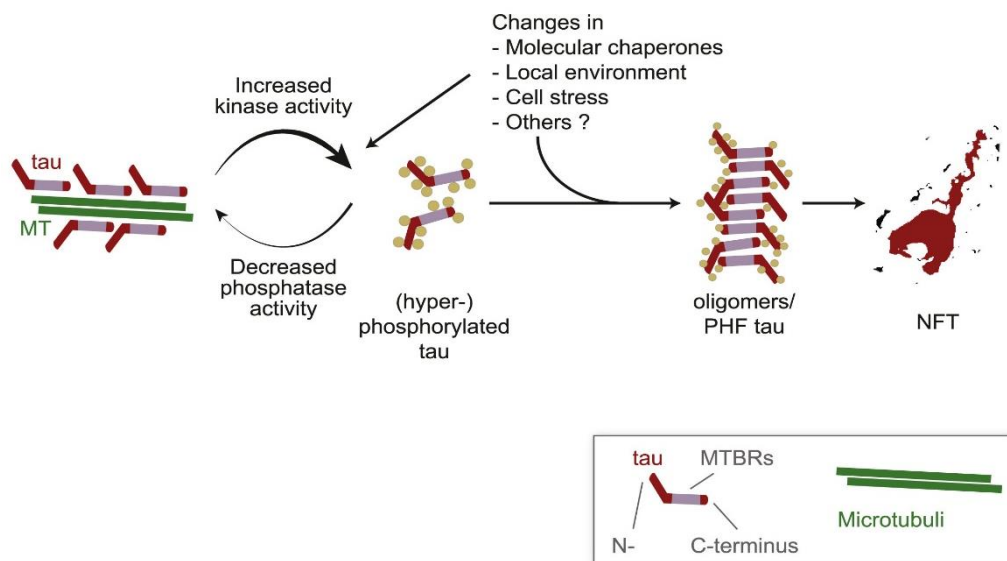
Figure 1.1: Schematic of neurofibrillary tangle formation.
Tau associated to microtubules become progressively phosphorylated at multiple sites due to altered kinase and phosphatase activity. Hyperphosphorylated tau is prone to oligomerise into paired helical filaments (PHFs) and eventually neurofibrillary tangles (NFTs). This process is influenced by changes in local environment, cell stress and other factors. Adapted from Ittner & Ittner, 2018.

Under normal conditions, tau is highly soluble and natively unfolded (Jeganathan et al, 2008). However, increased dissociated tau will aggregate to form insoluble, hyperphosphorylated pairs of filaments approximately 10-22 nm wide (paired helical filaments, PHFs) (Figure 1.2.C-E) (DeTure & Dickson, 2019; Crowther, 1991; Sadqi et al, 2002). Further tau misfolding and aggregation results in intracellular, non-fibrillary 'pre-tangle' formation (Bancher et al, 1991), preceding the formation of mature neurofibrillary tangles (NFTs) containing bundles of cross-linked tau filaments (Figure 1.2.A-B) (DeTure & Dickson, 2019). The morphology of NFTs is determined by the neuron type in which it forms; 'flame-shaped' tangles are found in the pyramidal cells of the hippocampus and cortex (layers II/III and V) whilst globoid NFTs are found in regions containing rounded neurons such as the raphe nucleus of the brainstem (Perl, 2010). Following cell death, extracellular ghost tangles remain (Figure 1.2.A) (DeTure & Dickson, 2019).
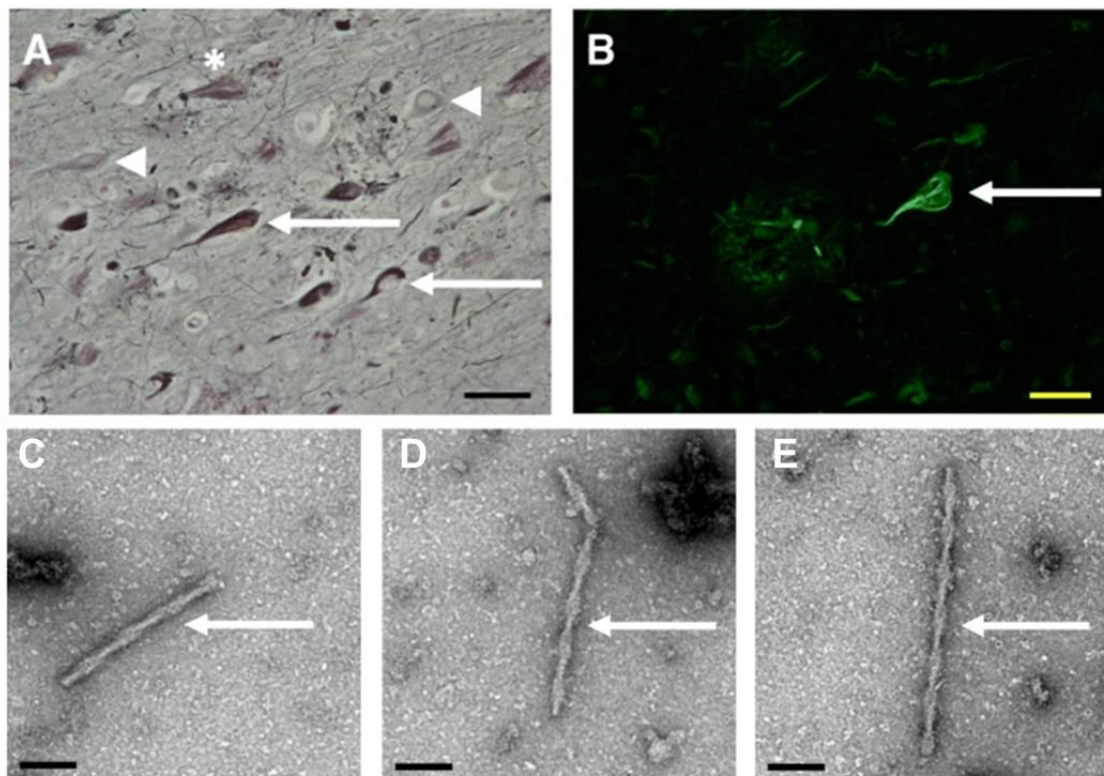
Figure 1.2: Tau aggregation in post-mortem AD brain tissue.
(A-B) Neurofibrillary tangle conformations in post-mortem AD brain tissue, visualised with (A) silver staining and (B) Thioflavin S; arrows: mature NFTs, arrowheads: pre-tangles, asterisk: ghost tangles. Top scale bar = 40 μm. C-E) Purified PHFs from AD patient brains visualised with EM and negative staining (2% uranyl acetate); arrows: PHFs. Bottom scale bar: 100 nm. Adapted from DeTure & Dickson, 2019.

1.2.2.2. Pathological consequences of tau aggregation

Pathological tau aggregation disrupts normal neuronal physiology via a loss of function and toxic gain of function. Misfolded phosphorylated tau ((p)tau) conformers isolated from AD brains lose the normal ability to bind to tubulin and therefore assemble and stabilise microtubules, which in turn inhibits axonal microtubular transport (Alonso et al, 1994). In addition, the presence of intracellular NFTs displaces cellular components including the nucleus, contributing to cell death (DeTure & Dickson, 2019).

1.2.2.3. Synaptic tau in Alzheimer's disease

Alzheimer's disease is the most common form of dementia accounting for 60-80% of cases (Alzheimer's Association, 2020). AD is defined and diagnosed by the deposition of amyloid plaques and neurofibrillary tangles (NFTs) in the brain, and significant atrophy at medial temporal regions and across the cortex (Alzheimer, 1906; Hippius & Neundörfer, 2003; DeTure & Dickson, 2019). Amyloid β (Aβ) is produced by the misprocessing of the amyloid precursor protein (APP) by beta-site amyloid precursor protein cleaving enzyme 1 (BACE1) and γ-secretase (Kent et al, 2020).

Clinical research has demonstrated that amyloid plaques accumulate 10-15 years prior to the onset of mild cognitive impairment (MCI) and upstream of progressive accumulation of tau-mediated neuronal disfunction and tissue loss (Figure 1.3) (Jack et al, 2010; 2013). However, it has been shown across several studies that Aβ accumulation does not correlate well with neuronal loss or AD symptoms, and that healthy patients suffering no cognitive impairment can have significant amyloid deposition (Delaère et al, 1990; Aizenstein et al, 2008; Villemagne et al, 2011). The degree of NFT accumulation and synapse loss in neocortical regions are better correlates for disease severity (Terry et al, 1991; Bierer et al, 1995).

There is increasingly substantial evidence from animal models of tauopathy-neurodegeneration that soluble tau mislocalised to synapses could play an active role in AD pathogenesis at an early stage in neurodegeneration prior to significant NFT accumulation. As an example, Ittner et al, 2016 showed increased site-specific phosphorylation of postsynaptic tau may function to protect neurons from Aβ toxicity in AD mouse models, but speculate that as the disease progresses, (p)tau could dissociate from the postsynaptic density and become a substate for other kinases resulting in hyperphosphorylation (Ittner et al, 2016; Ittner & Ittner, 2018).
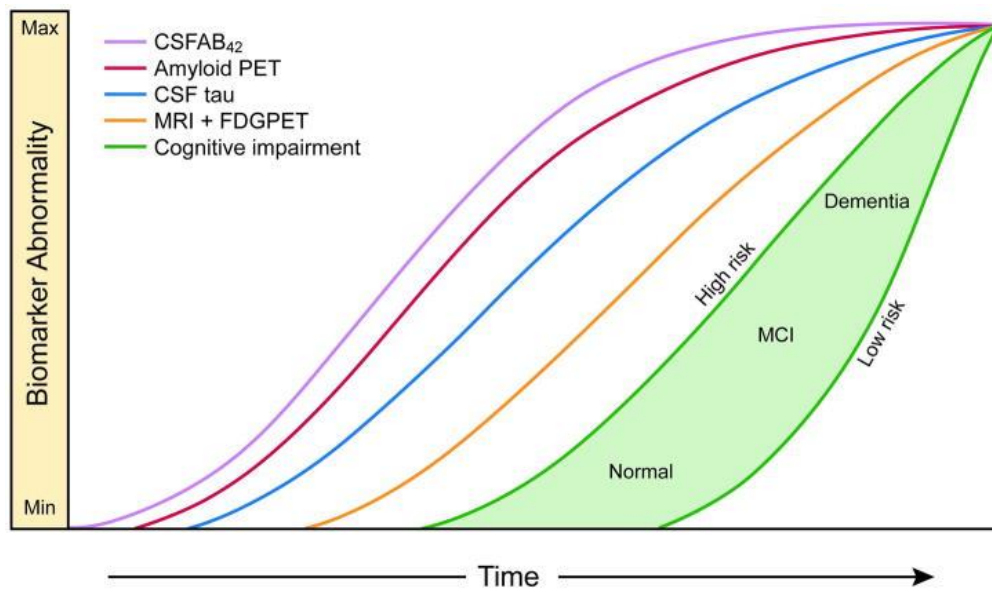
Figure 1.3: Alterations in AD biomarkers and symptoms over time.
Amyloid and tau load were determined by measurement of cerebrospinal fluid (CSF) Aβ42 (purple) and elevated tau (blue). Amyloid was also measured using PET imaging of patients (red line). Progressive neurodegeneration was measured using fludeoxyglucose (FDG) PET and structural MRI imaging (orange). The green filled area represents the cognitive impairment of patients over time. MCI: mild cognitive impairment. (Adapted from Jack et al, 2013).

Whilst the role of soluble synaptic tau has been studied more extensively in animal models for AD, it is likely that other tauopathies including FTDP-17 share a common pathological mechanism due to similarities in molecular tau disruption, such as post-translational modifications of tau resulting in disrupted phosphorylation (Saha & Sen, 2019). In addition, it has been shown in *in vitro* and *in vivo* tauopathy models that tau aggregates can be transferred trans-synaptically to neighbouring cells and induce misfolding of healthy tau proteins (Iba et al, 2013; Calafate et al, 2015; Brunello et al, 2020).

1.3.   rTg4510 mouse model of tauopathy

The rTg4510 transgenic mouse model was first described in 2005 (Ramsden et al, 2005; SantaCruz et al, 2005). rTg4510 mice (aka rTg(tauP301L)4510) express a repressible form of human tau (htau) containing a P301L mutation that causes FTDP-17. This mouse line was produced by crossing a 4510 responder line carrying human MAPTP301L cDNA downstream of a tetracycline responsive element (TRE) to an activator line expressing a tetracycline-controlled transactivator (tTA) under the control of the CaMKIIα promotor (Ramsden et al, 2005; Alzforum, 2019). This allows mice to constitutively express human tauP301L unless doxycycline (dox) is administrated which inactivates transgene expression.

1.3.1. Phenotype of rTg4510 mice

rTg4510 mice phenotypically resemble several features of neurodegenerative disorders. They develop progressive NFT deposition starting at ~4 months of age, followed by neuronal loss and forebrain atrophy (Ramden et al, 2005; Spires et al, 2006). Cortical thickness in rTg4510 mice is reduced almost 50% from 4 to 13 months (Figure 1.4) (Ludvigson et al, 2011). Mice also exhibit progressive behavioural impairments with age including impaired spatial reference memory and locomotor hyperactivity (Ramsden et al, 2005; Blackmore et al, 2017). Dox administration can arrest progressive neuronal loss, increases in tau pathology, and cognitive decline (Spires et al, 2006; Blackmore et al, 2017).
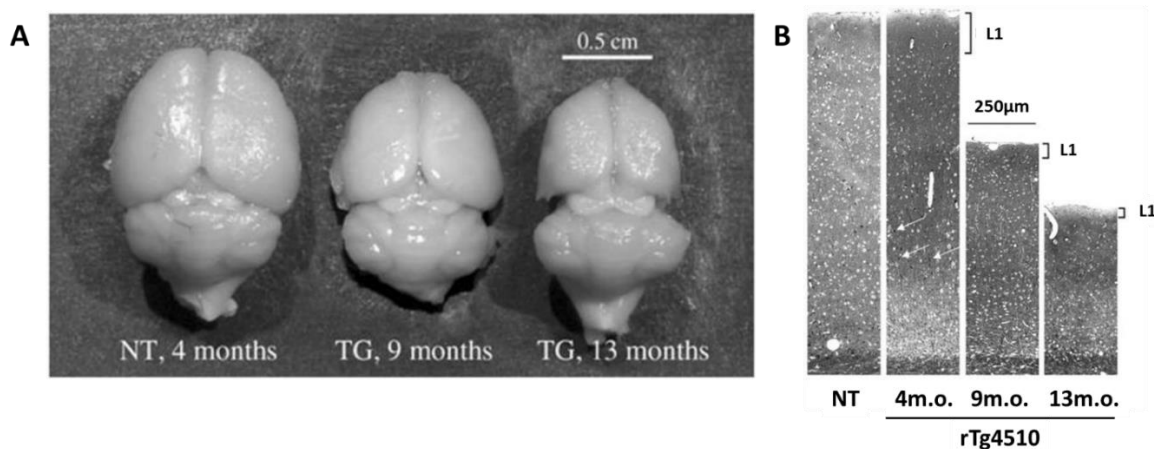
Figure 1.4: Forebrain atrophy in the rTg4510 mouse brain.
(A) Reduction in the size of the forebrain due to atrophy in rTg4510 transgenic (TG) mice at 9 months and 13 months of age in comparison to non-transgenic (NT) mice. (B) Vertical sections through NT mouse cortex, compared to rTg4510 mouse cortex at 4, 9 and 13 months of age. Cortex is stained with 1% toluidine blue. L1: Layer 1 of cortex. Adapted from Ludvigson et al, 2011.

1.3.2. Disrupted synaptic function in the rTg4510 model

The best correlate of a biomarker to cognitive decline in AD patients is synapse loss (Terry et al, 1991). Many studies have employed electrophysiology and imaging techniques to characterize synaptic disfunction, synapse loss and potential compensatory mechanisms responding to the pathological changes in the rTg4510 model with the purpose of elucidating the role of tau overexpression in synaptic dysfunction.

Whole cell patch clamp recordings of individual pyramidal neurons and morphological analysis of these cells have previously shown that tauP301L overexpression in the rTg4510 model results changes in action potential (AP) dynamics indicative of hyperexcitability, reduced dendritic complexity and length (Rocher et al, 2010) and reduced dendritic diameter

(Crimins et al, 2011). These electrophysiological and morphological changes occur independently of mature intracellular NFT formation therefore these pathological changes begin early in the disease process and before substantial cell loss (<4.5 months) (Rocher et al, 2010). Electrophysiological changes in pyramidal cells precede morphological changes such as reduced spine density (Crimins et al, 2012).

It is argued by Crimins et al, 2011; 2012 that increased intrinsic excitability of pyramidal cells acts as a homeostatic compensatory mechanism in response to loss of afferent input in progressive tauopathy so that overall network excitability is maintained (Crimins et al, 2011; 2012). This is not a consistent finding when other electrophysiological configurations are employed; Menkes-Caspi et al, 2015 used *in vivo* intracellular and extracellular recordings to show a reduction in the activity of single neocortical pyramidal cells, and the neocortical network (Menkes-Caspi et al, 2015).

Reduction in spontaneous pyramidal cell activity is supported by subsequent *in vivo* studies. Jackson et al, 2017 measured somatic Ca^{2+} transients in individual rTg4510 mouse neurons at 22 weeks of age (~5 months) to show both a reduction in the proportion of cells displaying spontaneous neuronal activity, and, in active cells, a reduction in the frequency and amplitude of spontaneous events (Jackson et al, 2017). In addition, 2-photon *in vivo* imaging demonstrated increased presynaptic and postsynaptic turnover and a reduction in spine size at this stage of tauopathy (Jackson et al, 2017).

1.3.3. Potential mechanisms of synaptic disruption in the rTg4510 model

Based on the findings summarised in 1.3.2, it is clear that rTg4510 mice at early stages of tauopathy, prior to significant deposition of mature NFTs, have disruption in the functional and morphological properties of synapses. There has been increasing evidence that soluble tau conformers mislocated in dendrites and dendritic spines may directly or indirectly cause disruptions in synaptic function.

One potential mechanism by which tau may disrupt synaptic function is via changes in glutamate receptor trafficking. In rat hippocampal cultures transfected with htauP301L, tau is mislocalised to dendritic spines in a phosphorylation-dependant manner resulting in the removal of GluA1 AMPA receptors from the postsynaptic density and decreased AMPA receptor-mediated synaptic currents (Hoover et al, 2010). This could result in synapse loss via postsynaptic LTD (Collingridge et al, 2010).

Another potential mechanism is that (p)tau could drive an increase in glutamate-induced excitotoxicity. Overexpression of tau from the P301L mutation has been linked to network hyperexcitability via an increase in potassium evoked glutamate release and reduction in glutamate clearance (Hunsberger et al, 2015). This preceded neuronal loss, suggesting glutamate excitotoxicity as an upstream cause of tauopathy-induced neurodegeneration. Miyamoto et al, 2017 related this to disrupted postsynaptic function by demonstrating that tau phosphorylated at Y18 promotes this glutamate-induced excitotoxicity by increasing

NMDAR dependant Ca^{2+} influence, and this can be reduced by shRNA-mediated knockdown of tau (Miyamoto et al, 2017).

Other studies have linked dendritic tau to F-actin depolymerisation, and hence the regulation the synaptic cytoskeleton, directly or indirectly via LTD induction (Regan et al, 2015). As a consequence, synaptic NMDARs could move to extrasynaptic regions where they contribute to ambient glutamate levels (Pallas-Bazarra et al, 2019) and mediate extracellular amyloid-β toxicity in AD (Ittner et al, 2010).

1.3.4. Visualising tau at dendritic spines in the rTg4510 model and beyond

If tau is exerting a local disruption at post-synapses as suggested by (Miyamoto et al, 2017; Pallas-Bazarra et al, 2019) confirmation of tau or (p)tau presence at dendritic spines should be achievable, but light microscopy (LM) studies are limited by standard light resolution as determined by the wavelength of visible light (λ) and numerical aperture of the objective. For standard light microscopes, the maximum resolution achievable is ~200 nm, allowing the resolution of dendritic spines (width ~<1 μm) but not molecular tau filaments (width ~10-20 nm).

Array tomography is a technique in which ultra-thin sections of tissue are independently imaged using LM and computationally reconstructed into a 3D z-stack but with increased axial resolution to match the resolution in the X-Y plane (Micheva & Smith, 2007). This technique in combination with immunohistochemistry for (p)tau and total tau has been used to demonstrate tau presence at dendritic spines in the rTg4510 mouse model (Figure 1.5A-C, Kopeikina et al, 2013).

This finding is relevant to AD pathogenesis in other rodent models and in human AD patients. The presence of endogenous tau at dendrites has been shown in rat primary hippocampal neurons undergoing amyloid-β induced spine loss via application of Aβ-derived-diffusible-ligands (ADDLs) (Figure 1.5E, Zempel et al, 2010). Tau has also been identified at synapses in human post-mortem tissue of both healthy and AD patients using electron microscopy (EM); DA9 antibody labelling for total tau demonstrated tau presence in pre and post-synapses in fixed permeabilized synaptoneurosomes from this tissue (Figure 1.5D, Tai et al, 2012).
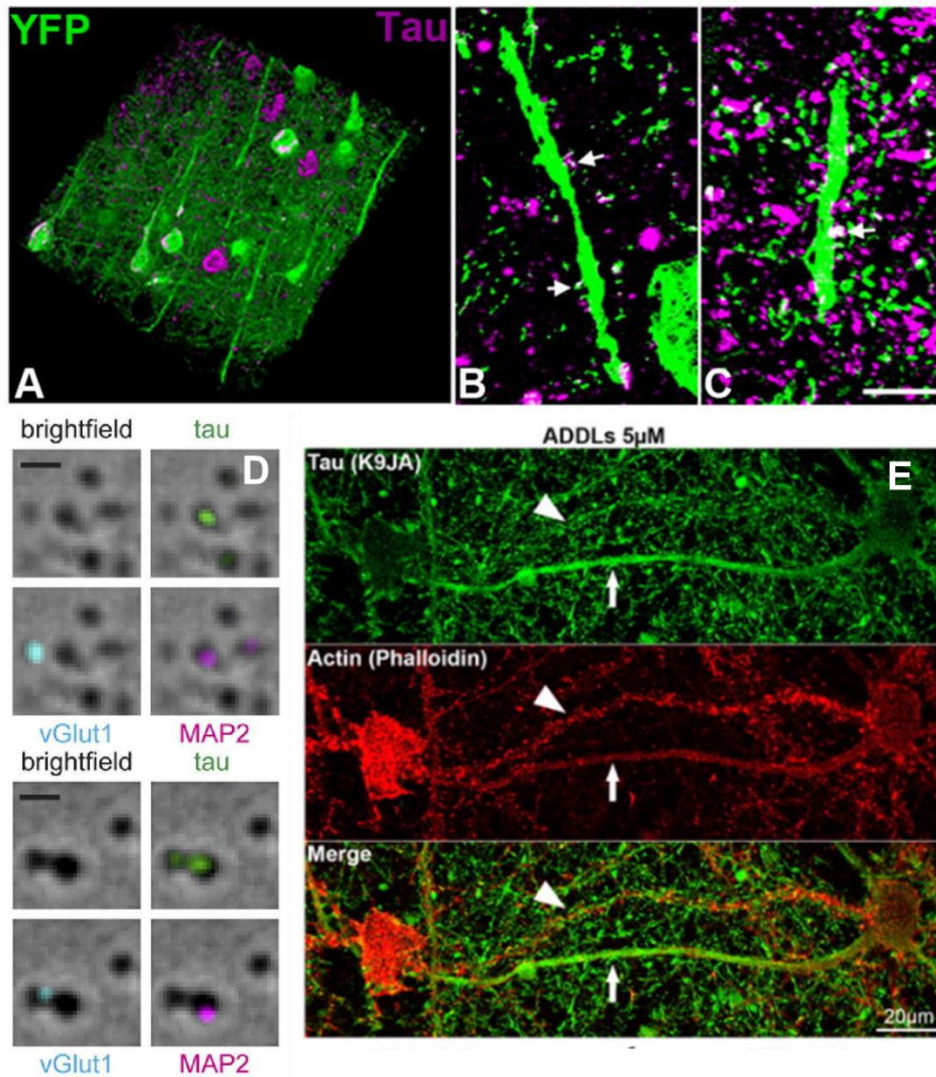
Figure 1.5: Tau presence at dendritic spines and synapses.

Studies demonstrating the presence of tau species at synapses/dendritic spines across different models of AD pathology and in human AD post-mortem tissue. (A) Array tomography stack reconstructed from 100 serial sections of 100 nm thick cortical tissue stained with PHF-1 and containing YFP+ neurons. Maximum intensity projections of 3 100 nm sections show the presence of (B) (p)tau and (C) total tau at dendritic spines (arrows). Scale bar = 5 µm (adapted from Kopeikina et al, 2013). (D) Synaptoneurosomes from brains affected with AD immunolabelled for a presynaptic marker (vGlut1), a postsynaptic marker (MAP2), and total tau (DA9 antibody). Tau proteins are detected in both MAP2+ (postsynaptic) and vGlut1+ (presynaptic) terminals. Scale bars = 1 µm (adapted from Tai et al, 2012). (E) Example of two nearby dendrites in a primary hippocampal culture after treatment with ADDLs (5 µM). The bottom dendrite (arrow) shows significant tau load and loss of dendritic spines, whilst the other dendrite (arrowhead) contains almost no tau, and has typical dendritic spine presence (adapted from Zempel et al, 2010).

The use of array tomography to demonstrate tau presence at dendritic spines in Figure 1.5.A-C (Kopeikina et al, 2013), improves axial resolution but is still limited by light resolution in

the X-Y plane. Since this finding, an alternative technique, Expansion Microscopy, has been developed and refined to increase resolution of fixed tissue samples using conventional light microscopes whilst retaining the advantages of LM, such as compatibility with immunohistochemistry (Chen et al, 2015).

1.4.   Expansion microscopy

Expansion microscopy (ExM) is a technique, first described by Chen et al, 2015, in which a biological specimen is physically expanded ~4.0-4.5x to enable imaging of sub-diffraction-limited structures probed with fluorophores on conventional light microscopes (Figure 1.6; Figure 1.7.A) (Chen et al, 2015). By expanding tissue 4.0-4.5 fold, the limit of resolution of subcellular structures is decreased to ~60-70 nm. The expansion of fixed tissue and cells is linear, three-dimensional, and uniform. The isotropy (uniformity in all directions) of tissue expansion has been validated by scaling post-expansion images of microscopic structures, such as microtubules, to match pre-expansion images, and measuring whether the length of these structures after expansion was equivalent to the pre-expanded condition when normalised by expansion factor. Over lengths of 10s and 100s of microns, the distortion of biological structures post-expansion was ~1-2%, therefore validating that the ExM retains nanoscale isotropy of the original tissue or cell sample (Chen et al, 2015; Tillberg et al, 2016; Wassie et al, 2018). Post-expansion, samples are transparent as the expanded material is >99% water, allowing index-matching to water-immersive objectives (Tillberg, 2021).

Since its conception, variants of the original protocol have been developed to improve accessibility of the technique and/or increase the factor by which samples can be expanded, achieving resolution as low as 20-30 nm (original ExM protocol= ~70 nm) (Tillberg et al, 2016; Chang et al, 2017; Truckenbrodt et al, 2018; Truckenbrodt et al, 2019; Gambarotto et al, 2019; Damstra et al, 2021). A brief outline of these ExM variants is summarised in Table 1.1.

1.4.1. Protein Retention Expansion Microscopy (ProExM)

The first expansion microscopy protocol published in 2015 devised a method of synthesizing a polymer network within and around a tissue sample, which would set as a swellable gel that would expand when dialysed with water (Chen et al, 2015). Fluorescently conjugated labels bound to the tissue or cell sample would be covalently linked to the polymer network allowing expansion and visualisation of the tissue or cell sample (Chen et al, 2015). Whilst this method introduced the potential of ExM for super-resolution imaging, native proteins and fluorescent labels could not be retained in the expanded tissue sample. This issue was overcome by use of custom oligonucleotide probes not widely available which limited the amenability of the protocol (Chen et al, 2015).

To resolve this, Protein Retention Expansion Microscopy, or ProExM, was developed in which native proteins in the sample are anchored to the swellable polymer network allowing

the use of conventional fluorescently labelled antibodies, streptavidin, and fluorescent proteins (Figure 1.6) (Tillberg et al, 2016). As is the case with the original ExM method, the expansion of tissue is typically a 4.0-4.5 fold increase from the original sample, reducing the light resolution limit by this same magnitude (i.e., ~300 nm / 4 = ~75 nm resolution) (Chen et al, 2015; Tillberg et al, 2016).

In ProExM, samples are first labelled with fluorophores which could involve expression of fluorescent proteins or immunohistochemistry (Figure 1.6). Following labelling, samples are treated with the succinimidyl ester of 6-((acryloyl)amino)hexanoic acid (acryloyl-X, SE, or AcX) which modifies amines on proteins with an acrylamide functional group (Figure 1.6, 1.7.D) (Tillberg et al, 2016). A polyacrylamide gel is synthesised by in situ polymerisation of monomer units: acrylamide, sodium acrylate, and N,N′-Methylenebis(acrylamide), a crosslinking agent for acrylamide. The polymerisation reaction is initiated by APS and TEMED. 4HT, an inhibitor of polymerisation, is also used to allow the pre-polymerised solution to perfuse the tissue sample. Polymerisation incorporates AcX anchoring groups into the gel material (Figure 1.6) (Tillberg, 2021).

Technique	Description	Expansion Factor	Reference(s)
Expansion Microscopy	Original protocol using custom oligonucleotide labels that can be incorporated into the polymer network	4.0-4.5	(Chen et al, 2015)
Protein Retention Expansion Microscopy	Adaptation of ExM where AcX anchors to native proteins (including fluorophores) in the sample	4.0-4.5	(Tillberg et al, 2016)
Iterative Expansion Microscopy	A similar protocol as (Chen et al, 2015), but after the initial expansion a second swellable polymer mesh is formed in the space created by the first expansion, so that the tissue is expanded twice in series	16-20	(Chang et al, 2017)
X10 Expansion Microscopy	An alternative gel of similar properties that can expand thin tissue sections tenfold	10	(Truckenbrodt et al, 2018) (Truckenbrodt et al, 2019)
Ultra-Expansion Micoscopy (U-ExM)	ExM protocol variant optimised for enabling isotropic expansion of molecular assembles, for example labelling the sample post-expansion to reduce antibody competition issues and fluorescence loss	4.0-4.5	(Gambarotto et al, 2019)
Ten-fold Robust Expansion Microscopy (TREx)	ExM gel recipe that can achieve tenfold expansion of thick tissue sections and cells whilst retaining gel firmness/ease of handling	10	(Damstra et al, 2021)

Table 1.1: Summary of ExM techniques.

Proteins within the polymerised gel-tissue complex are partially digested with Proteinase K allowing isotropic expansion of the tissue without resistance that may cause distortions or cracking (Figure 1.6) (Tillberg et al, 2016). This digestion stage of ProExM can differentially reduce fluorescence intensity of fluorophores (Figure 1.7.B). When the resulting sample is dialysed in water, the gel-tissue complex will expand due to the elongation of polymer chains that form the mesh-like structure of the polyacrylamide gel from a collapsed to an expanded state (Figure 1.7.C).
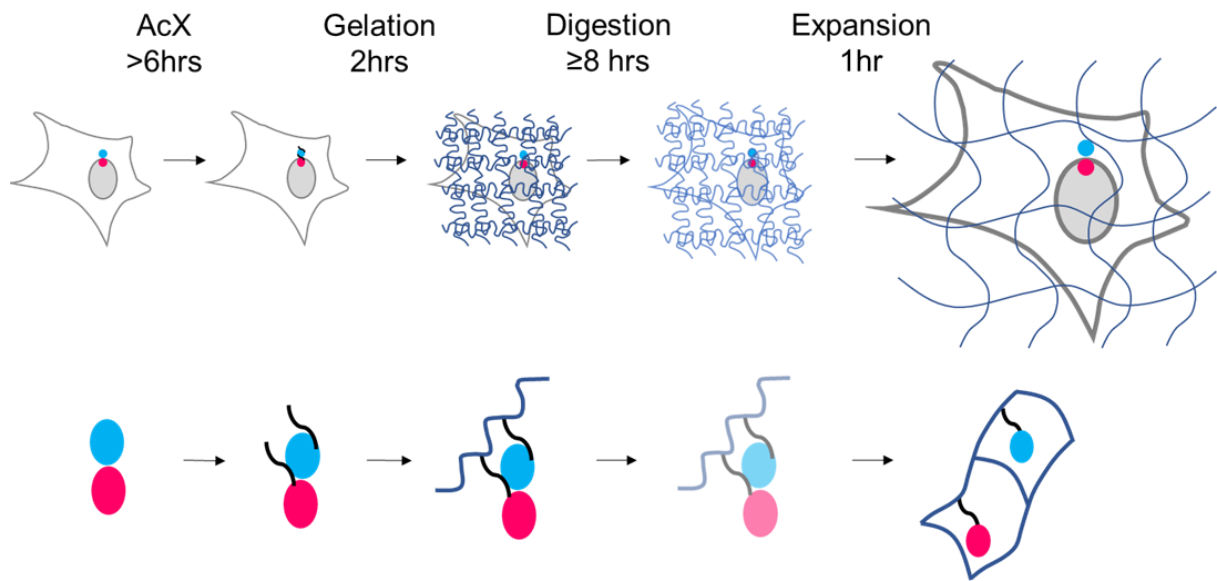
Figure 1.6: Schematic of ProExM protocol for expanding tissue samples.
A fixed, immunolabelled tissue sample is incubated in AcX which anchors to the amide groups of proteins. Monomers are assembled into a polyacrylamide gel mesh. The sample is digested in a dilution of Proteinase K overnight at room temperature. Following this, the sample is ready for expansion by dialysing with deionised water. Adapted from Tillberg et al, 2016.
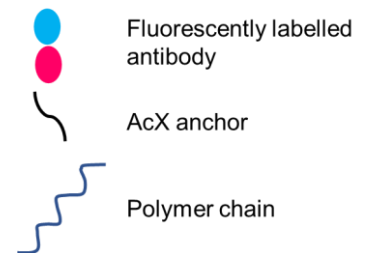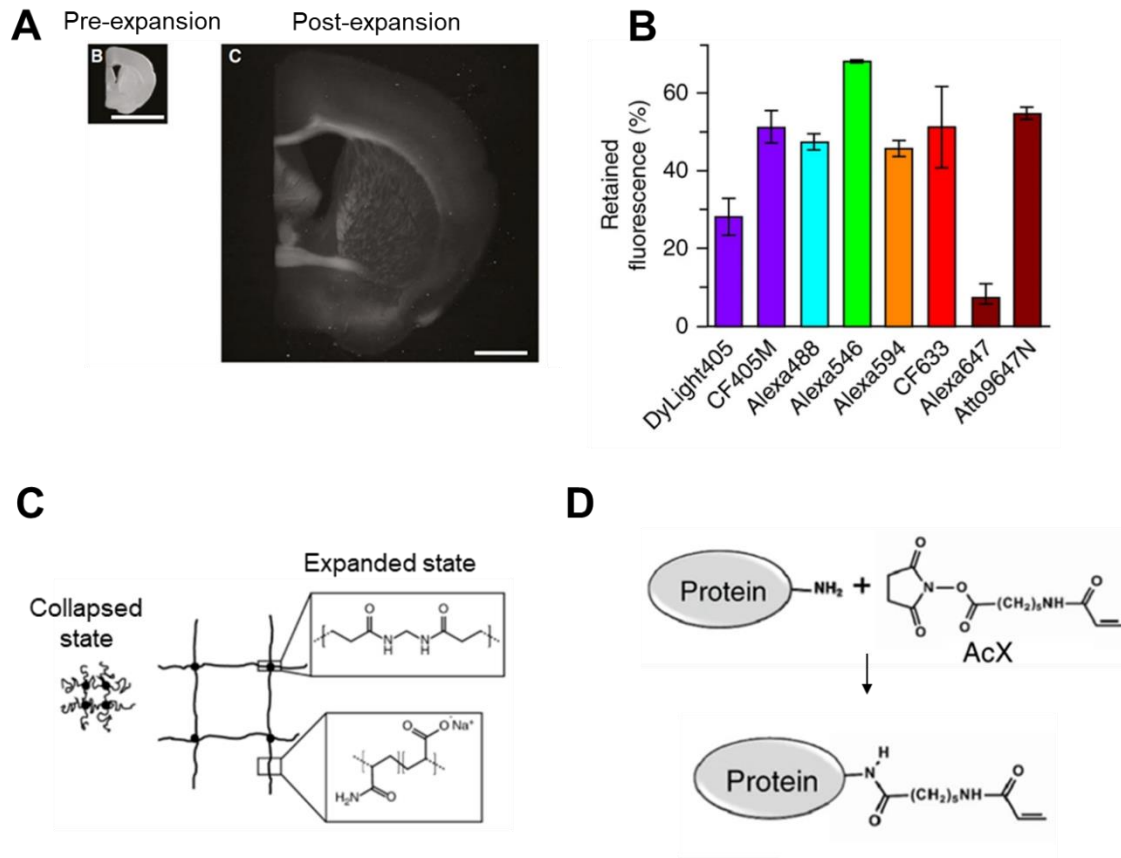
Figure 1.7: Features of ProExM tissue expansion.

(A) Photographs of a fixed mouse brain slice pre- and post-expansion. Scale bars: 5 mm. (adapted from Chen et al, 2015). (B) Retained fluorescence for selected fluorophores conjugated to antibodies after ProExM treatment (mean ± SD, n = 3 samples each) (adapted from Tillberg et al, 2016). (C) Schematic of the ExM hydrogel showing the cross-linker (dots) and polymer chains (lines) in the pre-expanded collapsed state (left) and the expanded state (right) (adapted from Wassie et al, 2018). (D) AcX links to amide groups of proteins within the tissue so that they can anchor to the polyacrylamide gel (adapted from Tillberg et al, 2016).

1.4.2. Using Expansion Microscopy to achieve ultrastructural resolution

Early ExM research validating the protocol demonstrated that ultrastructural features of mouse brain tissue could clearly be resolved, including synapses labelled with presynaptic and postsynaptic markers, and dendritic spines of neurons expressing virally delivered Brainbow3.0 (Chen et al, 2015; Tillberg et al, 2016). Studies that have imaged cell ultrastructure, such as actin filaments, before and after ProExM cell expansion have clearly demonstrated an improvement in resolution, and quantified this by plotting intensity profiles of images before and after expansion (Figure 1.8) (Park et al, 2020).

Iterative expansion microscopy (iExM) and X10 expansion microscopy (Table 1.1) have shown that by increasing the expansion factor, ultrastructure can be resolved in considerably greater detail. For example, when using immunohistochemistry for Bassoon and Homer1, the synaptic cleft (~20 nm) between these markers could be resolved (Chang et al, 2017; Truckenbrodt et al, 2018). Over time, new adaptions of these ExM variants have also been describe that retain the benefit of larger expansion factors as in Truckenbrodt et al, 2018, but aim to reduce the technical difficultly of setting and handling ExM gels (Damstra et al, 2021).
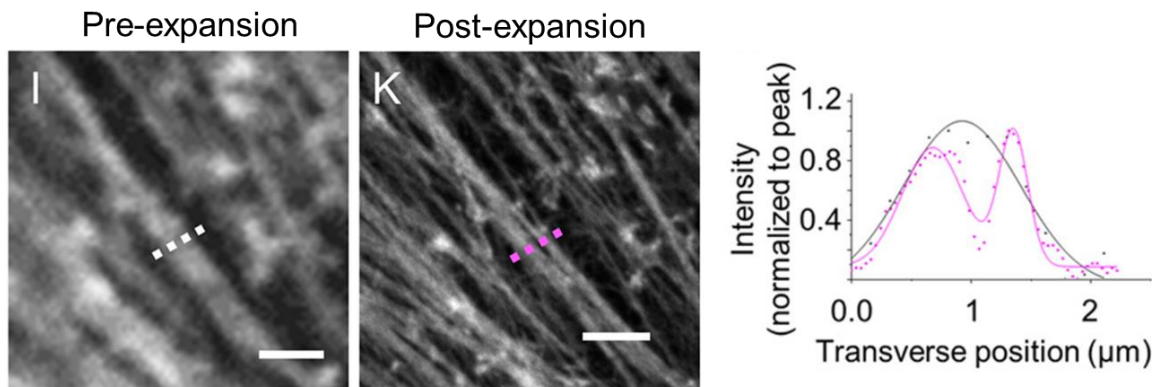
Figure 1.8: Improved resolution of actin filaments via ProExM.

Comparing the resolution of actin filaments labelled with Alexa Fluor 488-conjugated phalloidin and goat anti-rabbit Alexa Fluor 546 in BS-C-1 cells. The same cells were imaged using confocal microscopy (I) pre-expansion and (K) post-expansion. The graph (right) shows intensity profiles corresponding to the dotted lines in (I) and (K). The black dots correspond to the white dotted line in (I). The pink dots correspond to the pink dotted line in (K). Black dots have been fitted with a single Gaussian (black line). Pink dots have been fitted with a sum of two Gaussians (pink line). Scale bars: 2 μm. Scales are presented in pre-expansion dimensions. Adapted from Park et al, 2020.

1.5. Aims

Overall aim: To use Protein Retention Expansion Microscopy and immunohistochemistry to resolve pathological tau conformers at synapses in cortical tissue of 4-month-old rTg4510 mice.

1.) To validate that ProExM can improve the resolution of sub-diffraction-limited structures within mouse brain tissue without distortion of the biological sample. To demonstrate that this tissue expansion is reproducible, increasing the size of the sample by ~4.0-4.5x across multiple trials.

2.) To test whether expanding mouse rTg4510 tissue by ProExM results in improved resolution of PG-5 labelled tau fibrils probed with fluorophores.

3.) To use ProExM and immunohistochemistry for synaptic markers and (p)tau to investigate whether pathological tau conformers can be localised to synapses in rTg4510 mouse tissue at an early stage of pathogenesis before significant NFT deposition in the cortex.

2. Materials and Methods

2.1. Experimental animals

All mouse lines used were provided by Charles River, UK. During the optimisation of ProExM (Results 3.1.1), brain tissue from 5 week old female C57BL/6J/Thy1- (number of animals, n=2) and male P18 Emx1-IRES-cre (GCamP6) (n=1) mice were used. These mice were killed by cervical dislocation and brains were rapidly dissected, drop-fixed in 4% paraformaldehyde (PFA) for ~24 hours at 4°C and stored in 0.1M PBS.

To observe tau aggregation in early tauopathy (Results 3.2; 3.3.), 4-month old male rTg(tetO-TauP301L)4510 (n=4) transgenic mice were used. This mouse line is a cross between a responder line carrying human MAPTP301L cDNA downstream of TRE to an activator line expressing tTA under control of the CaMKIIα promoter (Ramsden et al, 2005; Santa-Cruz et al, 2005; Alzforum, 2019). Age matched wildtype (WT) littermates (n=2) were used as a control for tauopathy neurodegeneration (Results 3.2, 3.3.). rTg4510 and WT mice were killed by terminal anaesthesia and brains fixed by perfusion fixation using 4% PFA.

A P16 Gad2-IRES-cre/Ai95D-/Thy1- mouse (n=1) was used to test synaptic marker immunolabelling in young tissue (Results 3.3.3). This mouse was killed by cervical dislocation and the brain was rapidly dissected, drop fixed in 4% PFA for ~24 hours at 4°C and stored in 0.1M PBS. Mice were housed with ad libitum availability to food and water in a 12hr light/dark cycle. All procedures followed animal care and ethical guidelines approved by the Home Office and complied with the Animal Scientific Procedures Act (ASPA) 1986.

2.2. Tissue labelling

2.2.1. Sectioning

Fixed mouse brains were separated into four by cutting vertically via the midline to separate hemispheres and horizontally to remove the cerebellum and brainstem. The two frontal sections of brain tissue were embedded in 4% low melting point agarose and a vibratome was used to cut 100 μm tissue coronal slices from the prefrontal cortex to somatosensory cortex. Tissue slices were transferred to 24-well plates using a clean paintbrush and stored in 0.1M PBS until ready for staining.

2.2.2. Nuclear staining

For widefield imaging, 100 μm brain tissue slices were stained for cell nuclei using a 1:10000 dilution of 10mg/ml 4′,6-diamidino-2-phenylindole (DAPI) (Thermo Fisher, #D1306) in

0.1M PBS with 0.3% TritonX-100 for 15 minutes. Slices were then washed 2 x 15mins in 0.1M PBS.

For confocal imaging, TO-PRO™-3 Iodide (TO-PRO-3) (Thermo Fisher, #T3605) was used to label cell nuclei. 100 μm brain tissue slices were incubated in TO-PRO-3 diluted 1:1000 in 0.1M PBS with 0.3% TritonX-100 for 15 minutes and washed 2 x 15mins with 0.1M PBS.

To visualise nuclei in slices expanded using ProExM, nuclear staining was performed after the digestion stage to prevent loss of fluorescence. For unexpanded tissue slices that were stained for nuclei in combination with antibody labelling, nuclear staining was performed post-immunohistochemistry.

2.2.3. Immunohistochemistry for tau

100 μm slices were blocked using 10% normal goat serum (Vector Labs, #S-1000-20) in 0.3% TritonX-100 in PBS (blocking buffer) for >6 hours at room temperature (RT). Tissue slices were then incubated in primary antibodies for tau, diluted 1:500 in 0.1M PBS with 0.3% TritonX-100 and 1% normal goat serum. 4 slices were incubated per 2ml dilution within a well of a 6-well plate, and left overnight at RT and on a shaker at 20 rpm.

Monoclonal mouse primary antibodies were used which recognised different confirmations of tau protein. These included PG-5, PHF-1, MC-1 and DA9 (a gift from Professor Peter Davies, Albert Einstein College of Medicine, NY). PG-5 bound specifically to tau phosphorylated at ser409, immunolabelling both early and late tau aggregation in brain tissue (Jicha et al, 1999). PHF-1 bound to paired helical filaments of tau protein by recognising tau protein phosphorylated at Ser396 and Ser404 (Greenberg et al, 1992). MC-1 reacted with conformational epitopes of tau, visible in both early and late stage pathology (Ramsden et al, 2005). DA9 was conformation independent, binding to total tau (Zempel et al, 2010).

Following primary antibody incubation, tissue slices were washed 4 x 30 minutes in blocking buffer to remove unbound primary antibodies. All tau antibodies used were visualised using Alexa Fluor 488 goat-anti-mouse IgG (H+L) (Thermo Fisher, #A-11029). Tissue slices were incubated in this secondary antibody diluted 1:1000 in 0.1M PBS with 0.3% TritonX-100 and 1% normal goat serum overnight at 4°C. Tissue slices were shielded from light by covering 6-well plates in aluminium foil. Following secondary antibody incubation, sections were washed 4 x 30 minutes with blocking buffer in the dark to remove unbound secondary antibody. This was immediately proceeded by the gelation stage of Expansion Microscopy (2.3.2).

2.2.4. Immunohistochemistry for synaptic markers

Antibodies for a presynaptic and postsynaptic marker were used to visualise synapses in tissue slices. As a presynaptic marker, Bassoon polyclonal guinea pig primary antibody

(SYSY, #141004) was used, diluted 1:1000 in 0.1M PBS with 0.3% TritonX-100 and 1% normal goat serum. As a postsynaptic marker, Homer1 polyclonal rabbit antibody (SYSY, #160003) was used, diluted 1:200 in 0.1M PBS with 0.3% TritonX-100 and 1% normal goat serum. A Homer1 primary antibody dilution of 1:500 was initially tested but was suboptimal for immunolabelling as the signal was too weak to be easily detected. These antibodies for Bassoon and Homer1 were selected as they were previously demonstrated to be compatible with ProExM and other expansion microscopy variants (Tillberg et al, 2016; Truckenbrodt et al, 2018).

For Bassoon immunoreactivity, Alexa Fluor 555 goat anti-guinea pig secondary antibody was used (Thermo Fisher, #A-21435). For Homer1 immunoreactivity, Alexa Fluor 633 goat anti-rabbit secondary antibody (Thermo Fisher, #A-21070) was used as a default. In cases where Homer1 was used in combination with TO-PRO-3, which has a similar emission/excitation spectra as Alexa Flour 633 (Table 2.2), Alexa Flour 546 goat anti-rabbit secondary antibody (Thermo Fisher, #A-11035) was used. All secondary antibodies were diluted 1:1000 in 0.1M PBS with 0.3% TritonX-100 and 1% normal goat serum and tissue slices were incubated in this dilution overnight at 4°C.

2.2.5. Controls for immunohistochemistry

To control for non-specific fluorescence during immunohistochemistry, primary and secondary controls were established. Tissue slices were blocked as described in 2.2.3. For primary controls, secondary antibody incubation was omitted from the protocol so that only primary antibodies were bound to tissue. This controlled for any tissue autofluorescence that could be interpreted as specific secondary antibody fluorescence. For secondary controls, primary antibody incubation was omitted. This control tested for non-specific binding of secondary antibody i.e. binding to anything other than the primary antibody. This control also tested for the amount of background fluorescence compared to test slices.

2.3 Protein Retention Expansion Microscopy (ProExM)

2.3.1 Preparation of reagents and solutions

Reagents used in the ProExM protocol are summarised in Table 2.1. 5 mg Acryloyl-X SE (AcX) was dissolved in 500 μl anhydrous dimethylsulfoxide (DMSO) and stored as 20ul aliquots with drying agents at -20 °C. The monomer solution was comprised of 23.9% sodium acrylate (38g/100ml), 5.3% acrylamide (50g/100ml), 8.0% N,N'-methylenebisacrylamide (2 g/100ml), 42.6% sodium chloride (5M), 10.6% 10X PBS (1M), and 9.6% deionised water. This solution was stored as 1ml aliquots at -20 °C. Digestion buffer was comprised of 0.5% Triton-X 100, 0.2% EDTA (0.5 M, pH 8), 5% Tris.Cl (1M, pH8), 4.7% NaCl, and deionised water and stored as 1.5ml aliquots at -20°C.

2.3.2 Gelation

Following tissue labelling, PBS was replaced with 0.1mg/ml Acryloyl-X SE in 0.1M PBS
(1:100 dilution) and left overnight (>6hrs) at RT. Slices were then washed with 0.1M PBS 2
x 15mins. Gelling chambers were built so that a gel of fixed dimensions could be set evenly
around the tissue. These chambers were initially constructed using glass coverslips as
described in Asano et al, 2018. No. 1.5 coverslips were cut into 4 even sections using a
diamond knife and stacked to form spacers. To adhere spacers to one another, and to a glass
slide, a small droplet of water (<5ul) was used. Optimum height of the chamber was ~0.30-
0.38 mm (2 coverslips stacked). Chamber lids were assembled by wrapping a thick glass
coverslip in an even layer of parafilm.

Reagent	Abbreviation	Supplier	Catalogue Number
4-Hydroxy-TEMPO	4-HT	Sigma-Aldrich	176141-5G
acrylamide		Sigma Life Science	A88887-100G
Acryloyl-X, SE	AcX	Thermo Fisher	
Ammonium Persulfate	APS	Fisher BioReagents	BP179-100
Dimethyl sulfoxide	DMSO	Sigma-Aldrich	276855-100ML
Ethylenediaminetetraacetic acid disodium salt dihydrate	EDTA	Sigma Life Science	E5134-50G
N,N'-methylenebis(acrylamide)		Sigma-Aldrich	146072-100G
PBS tablets		VWR	E404-100TABS
Sodium Acylate		Aldrich	408220-25G
Triton® X-100		Sigma Life Science	T8787-100ML
UltraPure™ 1M Tris-HCL pH8.0	Tris-HCl	Thermo Fisher	15568-25
UltraPure™ N,N,N′,N′-tetramethylethylenediamine	TEMED	Thermo Fisher	15524010
Proteinase K, Molecular Biology Grade		New England Biolabs	P8107S

Table 2.1: List of reagents used for ProExM.

This gelling chamber set up was used for experiments described in 3.1.1. However, this
method was time consuming and unreliable as the water tension between coverslips was
easily broken when setting gels. Instead, a new design for gelation chambers was made and
3D printed with wells of 12*10*0.3 mm. This chamber was adhered to glass slides using
silicon grease (Figure 2.1.A). This adaptation applied to data in 3.1.2. onwards.

Gelling solution was made in a 1.5ml microcentrifuge tube on ice in a 47:1:1:1 ratio of
monomer solution, TEMED (10g/100ml), 4-HT (0.5g/100ml), and APS (10g/100ml) (Table
2.1). A 100 µm slice was transferred to this microcentrifuge tube and kept at 4°C and on ice
for 20 minutes to allow the solution to perfuse the tissue (monomer perfusion stage) (Figure

2.2.A). Initially, 30 minutes was trialled for monomer perfusion but this could sometimes result in premature gelation of the solution.

Following monomer perfusion, 20 µl of gelling solution was pipetted from the microcentrifuge tube into the gelling chamber (Figure 2.2.B). The tissue slice was transferred into the chamber using a paintbrush and placed on top of the gelling solution so that the bottom surface of the tissue was evenly coated. 40 µl of gelling solution was pipetted onto the tissue slice within the chamber, making small adjustments so that the chamber was not under/overfilled. The gelling chamber lid was placed over the sample gel carefully ensuring no air bubbles formed over the embedded tissue slice (Figure 2.2.C-D). Gelling chambers were then transferred to an incubator (37°C) for 2 hours to facilitate gel polymerisation.
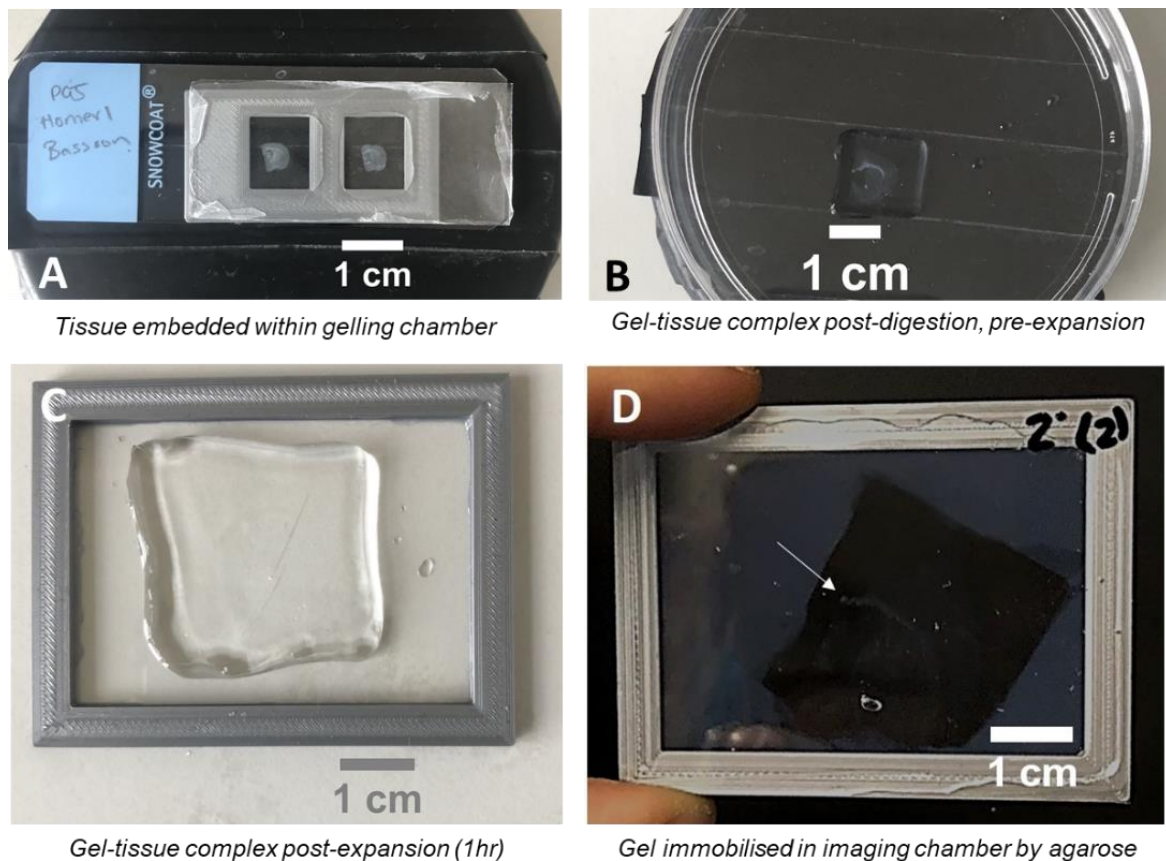
Figure 2.1: Photographs of gel-tissue expansion in the ProExM protocol.
(A) A gelling chamber adhered to a glass slide containing set polyacrylamide gels and embedded tissue slices. (B) Appearance of the gel-tissue complex post-digestion in proteinase K but prior to expansion in deionised water. (C) A fully expanded gel after 1 hour of dialysing in deionised water. The embedded gel at this stage is almost completely transparent. (D) Expanded gel-tissue complex within an imaging chamber and immobilised with 2% low melting point agarose. The arrow indicates white matter tracks which are still visible in adult mouse brain tissue post expansion.
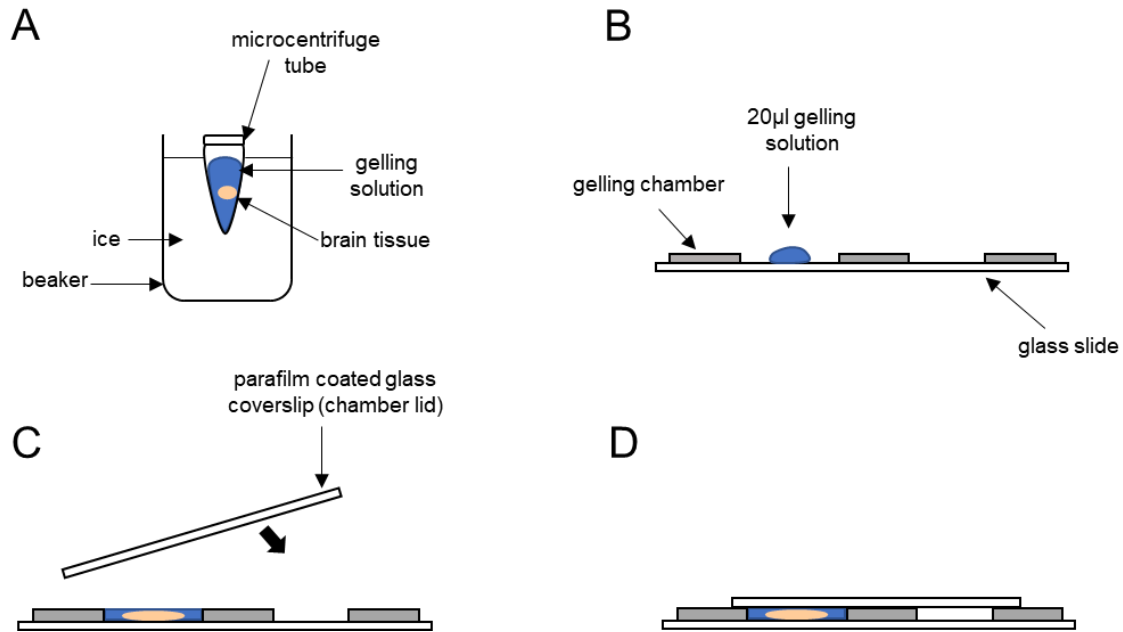
Figure 2.2: A diagram of the gelation stages of ProExM.

(A) Post AcX incubation a 100 µm tissue slice is transferred to gelling solution (=monomer solution +TEMED + 4-HT + APS) for 20 minutes on ice to allow monomer perfusion. (B) After 20 minutes 20ul of gelling solution is transferred to a well of the gelling chamber. (C) The tissue slice is placed on top of gelling solution and the remainder of space in the well is filled with gelling solution (~40 µl). A parafilm coated lid is placed over the gelling chamber. (D) The sealed gelling chamber containing gelling solution and brain tissue is placed in an incubator at 37°C for 2 hours to facilitate gel polymerisation. Adapted from Asano et al, 2018.

2.3.3 Digestion

Following the gelation stage of ProExM, polymerised gels were removed from gelling chambers. A blade was used to separate the chamber lid from the sample gel, and remove the plastic chamber mould from the glass coverslip.

Proteinase K was diluted 1:100 in digestion buffer. 2ml of this dilution was pipetted into wells of a 6-well plate. A small volume of this digestion solution was placed on the sample gel using a paintbrush to detach the sample gel from the glass coverslip. The sample gel was then transferred to the 6-well plate using a paintbrush and left in digestion solution overnight, approximately 16 hours, at RT and on a shaker at 20rpm.

2.3.4 Expansion

Post-digestion, the sample was ~1.5x its original size (Figure 2.1.B). Digestion solution was removed from the well of the 6-well plate using a pipette and replaced with 0.1M PBS. When the gel was ready for expansion, a coverslip and paintbrush was used to carefully transfer the gel to a petri dish containing deionised water. Deionised water was replaced in the petri dish every 20 minutes for 1hr. During this stage, the gel would expand and the embedded tissue within the gel would become almost completely transparent (Figure 2.1.C).

Post-expansion, the gel was ~4x its original size. To image expanded gels using confocal microscopy, an imaging chamber was designed. These 3D chambers (64*48*2 mm) were printed to fit over large glass coverslips (Figure 2.2.C-D). Chambers were secured onto coverslips using silicon grease.

A large glass coverslip (64x48 mm) and paintbrush was used to transfer the expanded gel into an imaging chamber. Any water transferred into the imaging chamber was removed using a pipette. The surrounding space in the imaging chamber was filled using 2% low melting point agarose that had cooled and set slightly (Figure 2.1.D). A large glass coverslip was then placed over the imaging chamber, sealing the expanded gel within.

2.3.   Microscopy

2.4.1. Widefield microscopy

Widefield microscopy was used to image DAPI-labelled cell nuclei in unexpanded and expanded tissue slices (Section 3.1.1.). A Leica DM IRB inverted widefield microscope was used with the filter range 340-380 nm (DAPI excitation/emission: 358/461 nm) and a 10x dry objective lens. Images were captured using NIS-Elements F software and saved as .tif files. Unless otherwise stated, all unexpanded and expanded DAPI-labelled slices were imaged free-floating in plastic 6-well plates or petri dishes.

2.4.2. Confocal microscopy

Confocal microscopy was used for imaging of immunolabelled and TO-PRO-3 labelled tissue slices in results 3.1.2. onwards. Immunolabelled tissue slices were imaged using a confocal laser scanning Olympus FV1200MP with an upright BX61 microscope. Excitation laser wavelengths used were 488 nm, 559 nm and 633 nm. Images were obtained using OLYMPUS FLUOVIEW Ver.4.2b software and saved as .oib files. A x25 XLPLN25XWMP2 water-immersive objective lens (numerical aperture, NA: 1.05) was used for the majority of confocal imaging, however during the process of collecting data, chromatic aberration of the Alexa Fluor 488 signal was observed (signal was axially displaced) when using this objective. Therefore, unless otherwise stated, tissue slices labelled with multiple fluorophores were imaged using a 60x LUMPLFLN60XW water-immersive

objective lens (NA: 1.00) was that was chromatically corrected at the visible wavelength range. The peak excitation/emission values for each fluorophore, in addition to the emission filter ranges used, is summarised in Table 2.2.

For confocal imaging of expanded tissue slices, 3D printed imaging chambers were used (Section 2.3.4., Figure 2.2.C-D). This chamber allowed both faces of the expanded gel-tissue complex to be imaged which optimised working distance.

Fluorophore	Peak excitation/emission (nm)	Emission filter range (nm)
Alexa Fluor 488	498/520	500-545
Alexa Fluor 546	556/573	570-625
Alexa Fluor 555	553/568	570-625
Alexa Fluor 633	649/666	655-755
TO-PRO-3	642/661	655-755

Table 2.2: Fluorophore excitation/emission values.

Summary of the peak excitation/emission values and the emission filter ranges used for the visualisation of fluorophores in confocal microscopy.

2.4. Image analysis

2.5.1. Quantifying size of the expansion of tissue slices

For quantification of the size of the expansion of tissue by ProExM, the software FIJI was used to manually segment nuclei and measure their size and properties. The Feret diameter (μm), area (μm^2) and perimeter (μm) of nuclei in layer II/III of the cortex were measured in unexpanded and expanded tissue. Circularity was derived from these measurements [circularity = 4pi(area/perimeter^2)], and used as confirmation that the expansion was linear. Expansion factor was calculated as the ratio of mean Feret diameter (μm) of cell nuclei per expanded tissue slice compared to the average mean Feret diameter of cell nuclei measured from 4 different unexpanded tissue slices. Nuclei in layer II/III cortex of unexpanded tissue slices were selected for measurement if they were in sharp focus. In both expanded and unexpanded tissue slices, non-circular nuclei (i.e., nuclei of pericytes) where excluded from measurement.

2.5.2. Identifying the number and widths of peaks in data

To compare the resolution of tau fibrils in images obtained from expanded and unexpanded PG-5-immunolabelled slices, images were taken of regions of somatic tau aggregation using 5x digital zoom for expanded slices, and x15 digital zoom for unexpanded slices to account for the difference in size post-expansion. Images were converted to .tif files, and the

'findpeaks' MATLAB function was used to identify local maxima in pixel intensity across fluorescence profile traversing the soma for each image file. The number of peaks and widths of peaks identified per image were obtained for statistical analysis.

Prominence measures how much a peak stands out based on its intrinsic height and its location relative to other peaks. To select a minimum peak prominence value (mppv) for identifying peaks in these data, a small, random sample of images (Expanded = 5, Unexpanded = 5) were tested with a mppv of 200, 250 and 300. For the majority of unexpanded images there was little difference in the number of peaks identified at these mppvs (Figure 2.3). There was evidence from the sample of expanded images that mppv of 200 was too sensitive, occasionally identifying peaks in the data which were not subjectively apparent in images (Figure 2.4). In addition, a mppv of 300 appeared to miss some peaks in data that were visible on the original image (Figure 2.5). Based on these findings, a mppv of 250 was selected.

2.6. Statistical analysis

For statistical analysis, the software IBM SPSS statistics 24 was used. For parametric analysis, datasets were tested for normal distribution of residuals and equality of variance between groups. If these assumptions were not met, non-parametric testing was used. Statistical significance was quoted by asymptotic P-values, set at $P<0.05$ (*$P<0.05$, **$P<0.01$, ***$P<0.001$).

To compare the size of DAPI-labelled nuclei from control (unexpanded) and expanded tissue slices (Results, Figure 3.3), two-way independent factorial ANOVAs were used with factors 'Condition' (Levels: Control, Expanded) and 'Run' (Levels: 1-3)). To compare the size of TO-PRO-3-labelled nuclei from control and expanded tissue slices (Results, Figure 3.6), Mann Whitney U tests were used for each measurement variable (Feret diameter, area, and circularity). To compare the size of nuclei post-expansion across different slices, a one-way ANOVA was used with factor 'Slice' (Levels: 1-4). Where an ANOVA test was used, the F ratio of this analysis was quoted.

The non-parametric Mann-Whitney U test was used to compare the difference in number of peaks, and widths of peaks, across the control and expanded condition as variance was unequal between groups and data from the unexpanded condition was not normally distributed. Where the Mann Whitney U test was used, the standardised test statistic was quoted.
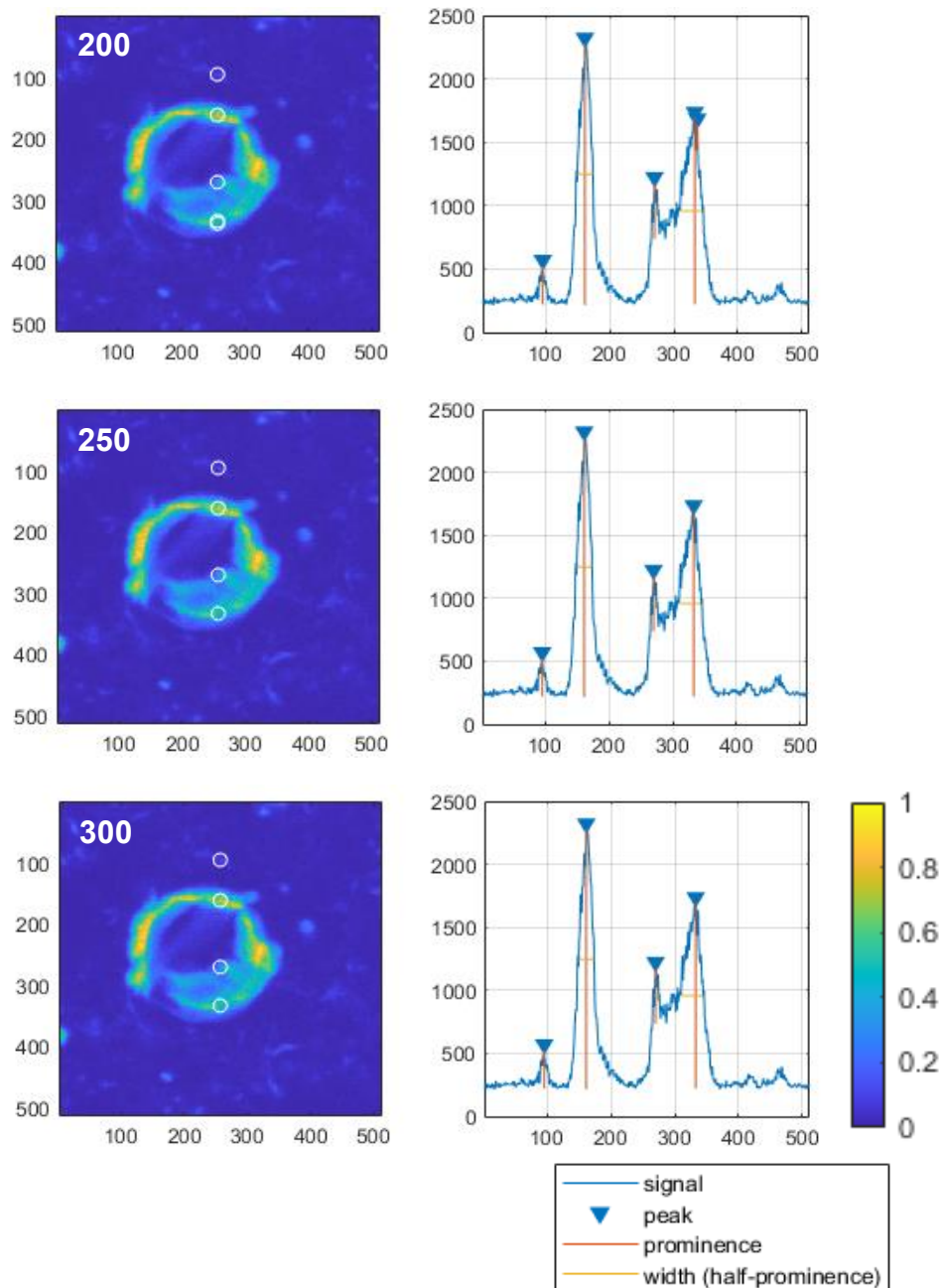
Figure 2.3: Sampling minimum peak prominence values (part 1).
Identification of peaks in pixel intensity from confocal images of tau aggregation in unexpanded rTg4510 PG-5 labelled tissue when applying a minimum peak prominence value of 200 (top), 250 (middle) and 300 (bottom). The location of peaks along the vertical midline are indicated by white circles on heatmap images, and blue arrowheads on corresponding plots of pixel intensity.
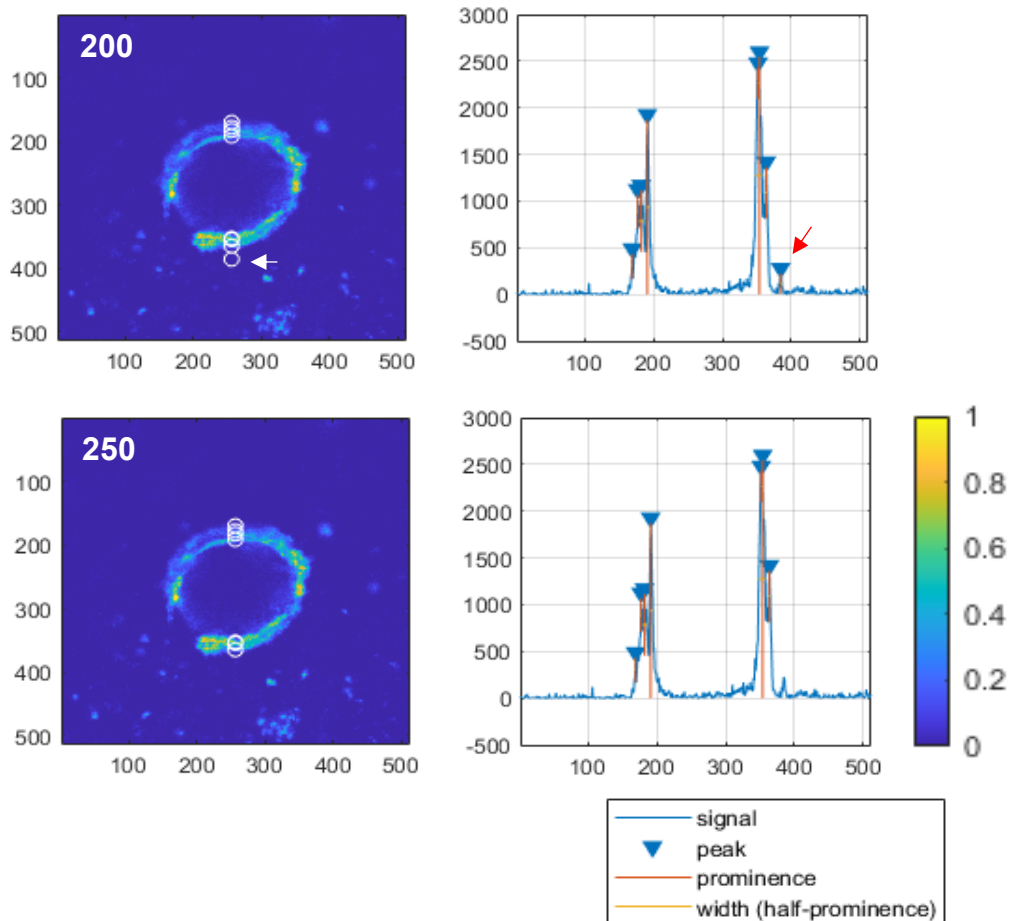
Figure 2.4: Sampling minimum peak prominence values (part 2).
Identification of peaks in pixel intensity from confocal images of tau aggregation in expanded rTg4510 PG-5 labelled tissue when applying a minimum peak prominence value of 200 (top) and 250 (bottom). The location of peaks along the vertical midline are indicated by white circles on heatmap images, and blue arrowheads on corresponding plots of pixel intensity. The red arrow indicates a peak identified with mppv=200 that cannot be seen on the corresponding heatmap image, indicating oversensitivity.
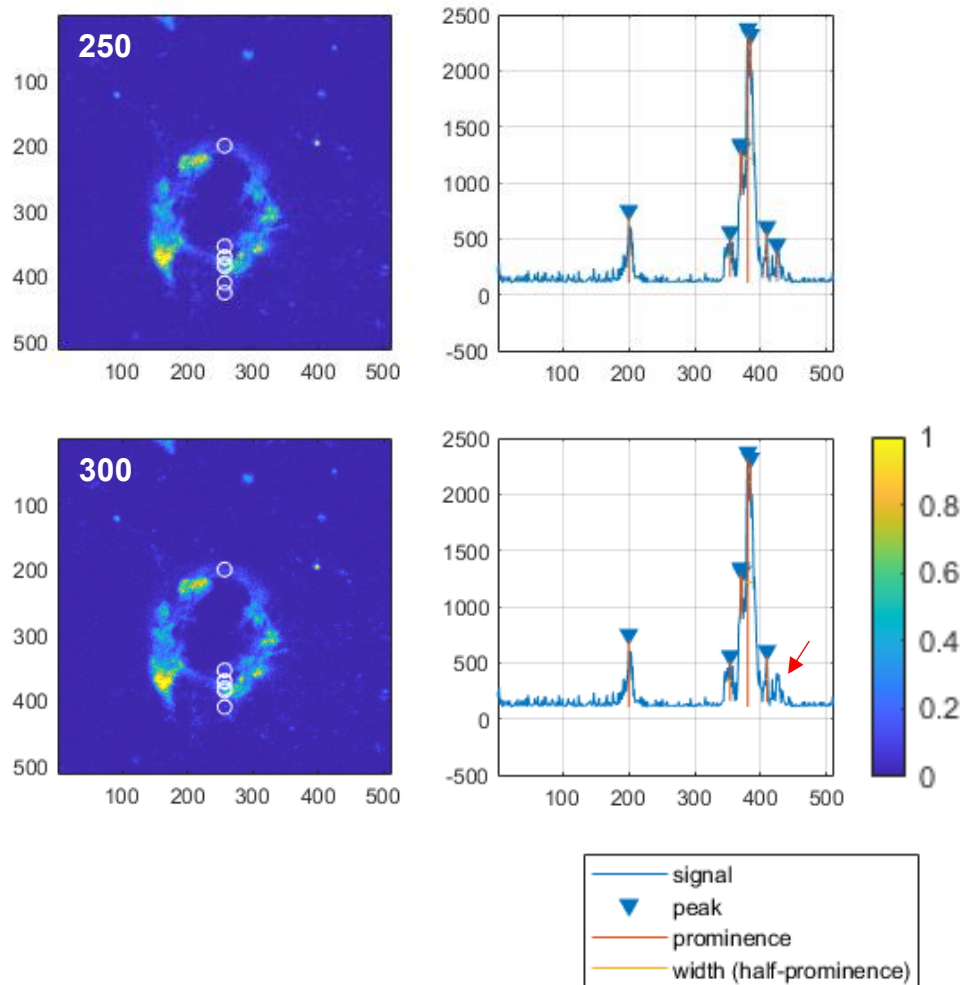
Figure 2.5: Sampling minimum peak prominence values (part 3).

Identification of peaks in pixel intensity from confocal images of tau aggregation in expanded rTg4510 PG-5 labelled tissue when applying a minimum peak prominence value of 250 (top) and 300 (bottom). The location of peaks along the vertical midline are indicated by white circles on heatmap images, and blue arrowheads on corresponding plots of pixel intensity. The red arrow indicates a peak that has not been identified with mppv=300 but can be seen on the corresponding heatmap image, and is detected by mppv=250.

3. Results

3.1. Set up of ProExM and measurement of the properties of tissue expansion

3.1.1 Optimising the ProExM protocol

The ProExM tissue expansion protocol can have common issues that require troubleshooting including loss of fluorescence post-expansion, premature gelation, and limited working distance when imaging due to the increased thickness of the expanded sample (Summarised in Asano et al, 2018). The first series of experiments run were therefore focused on:

1) Successfully expanding mouse tissue slices based on the Asano et al, 2018 protocol
2) Adjusting the protocol to improve reproducibility of expansion, mitigate common issues and improving ease of gel handling
3) Quantifying the size and properties of cell nuclei post-expansion compared to unexpanded tissue

In all optimisation trials, tissue slices from paraformaldehyde-fixed mouse brain were labelled with DAPI to visualise nuclei. The initial runs of ProExM are summarised in Table 3.1. Trial 1 was successful in that the gel-tissue complex did expand however the sample was too thick for imaging and therefore an adjustment was made to the gelling chamber thickness from ~0.6 mm (4 stacked glass coverslips) to ~0.3 mm (2 stacked glass coverslips). Reducing gel thickness increased the working distance for widefield imaging in trials 2-5.

| Trial	Tissue	Age	No. slices expanded	*DT (hrs)	Issues	Adjustments
1	C57BL/6J/Thy1-	~1m.o.	4	N/A	Gels were set too thick	Set gels in thinner chambers to increase working distance
2	C57BL/6J/Thy1-	~1m.o.	4	N/A	2/4 gels set prematurely	Adjust time of monomer perfusion to 20min
3	C57BL/6J/Thy1-	~1m.o.	2	18	Fragile gels	N/A
4	Emx1-ires-cre	P18	2	15.5	Limited working distance and aberration when imaging in plastic petri dishes	Design an imaging chamber where gels can be imaged from both sides via glass coverslips
5	Emx1-ires-cre	P18	3[†]	19	Fragile gels	Reduce the digestion time to ~16hrs

Table 3.1: Optimisation of ProExM protocol.

Summary of initial ProExM trials and the adjustments required to optimise the protocol.

*: Digestion time; the amount of time that gel-tissue complex was left in Proteinase K @RT.
†: 2 expanded slices were used for data acquisition. The additional slice was used to test the
glass imaging chamber (Figure 3.2).

Trial 2 flagged another common issue with ProExM as 50% of gels set prematurely during the monomer perfusion stage. To mitigate this, monomer perfusion time was reduced from 30 mins to 20 mins with regular agitation of the solution. This adjustment has also been made in subsequent ProExM protocols (Tillberg, 2021).

DAPI staining in expanded slices in trials 3-5 was imaged using widefield microscopy so that the post-expansion size of nuclei could be measured (Figure 3.1). There were still optimisations being made to the protocol during these trials as shown in Table 3.1, but these issues did not prevent gels from being imaged as was the case for trials 1-2. During this stage, it became apparent that an 'imaging chamber' needed to be constructed so that the expanded samples could be imaged from top to bottom in the z-plane (Section 2.3.4). Figure 3.2 compares DAPI-labelled expanded tissue imaged in a plastic petri dish vs the imaging chamber, and it was clear that the later improved the signal:background ratio significantly. Gel fragility was also an issue in trials 3-5 which made handling of the sample difficult as it was prone to breaking. Gel fragility can arise from over-digesting the sample or having insufficient crosslinker present (Tillberg, 2021; Campbell et al, 2020).
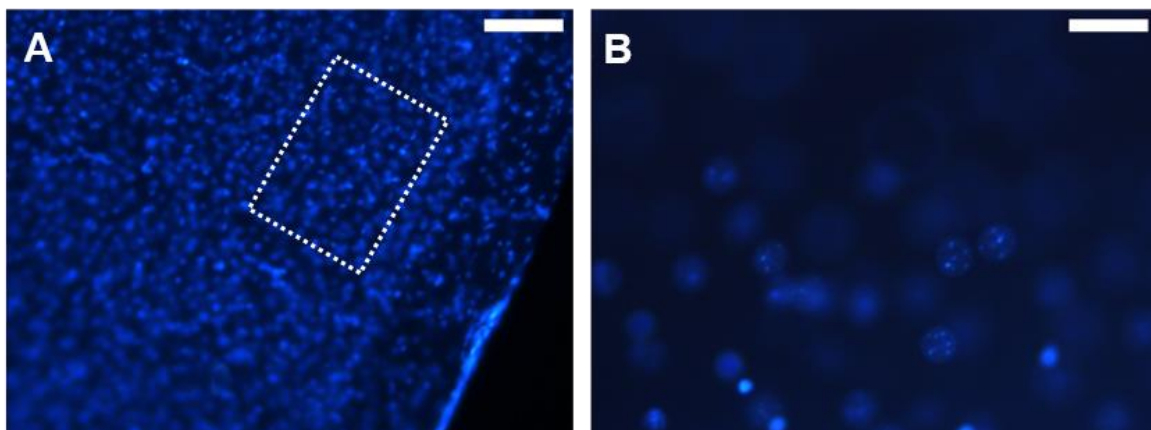
Figure 3.1: **Expansion of DAPI-stained cortical tissue.**
Example images obtained from widefield imaging of free-floating (A) unexpanded and (B) expanded tissue labelled with DAPI. The box in A represents the layer II/III cortical region where nuclei properties were measured for quantification of expansion, and corresponds to the approximate location in the cortex imaged in B. These images were obtained in trial 4 of Table 3.1. Scale bars: 100 μm. Magnification: x10.
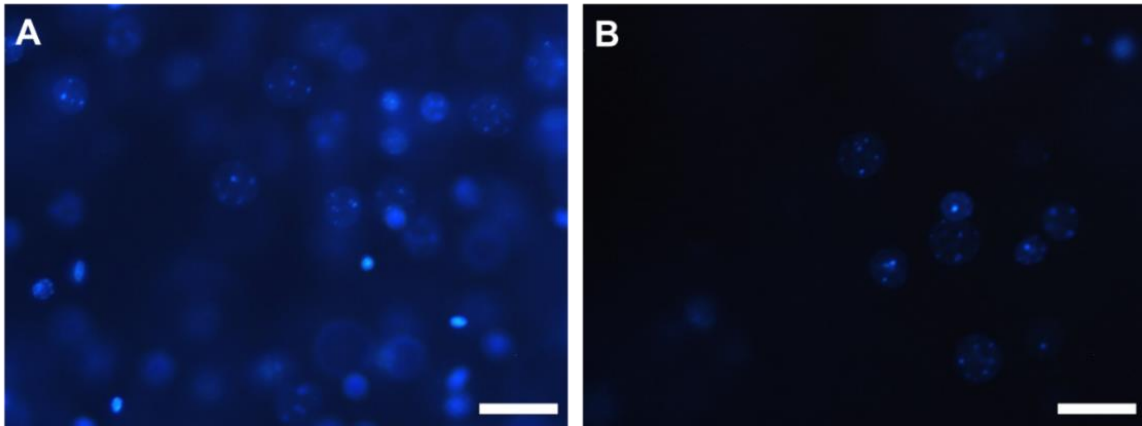
Figure 3.2: Improving image quality using custom glass chambers.
Example images obtained from widefield imaging of expanded tissue samples labelled with DAPI and imaged (A) free-floating in a plastic petri dish or (B) immobilised in a glass imaging chamber. These images were obtained in trial 5 of Table 3.1. Scale bars: 100 µm. Magnification: x10.

To assess the extent of expansion, the size and morphology of nuclei were measured in 6 control (unexpanded) and 6 expanded tissue sections from trials 3-5 (2 tissue sections per trial) (Figure 3.3). Trials 3-5 from table 3.1 are shown in Figure 3.3 as Runs 1-3. Averaged across runs 1-3, the mean Feret diameter of individual cell nuclei increased in the expanded tissue compared to control tissue, from 10.49 ± 0.10 µm to 49.83 ± 0.59 µm ($P<0.001$, F ratio = 5313.38) (Figure 3.3A, Figure 3.3B). There was also a significant increase in mean nuclei area post-expansion by ~23.8 fold ($P<0.001$, F ratio= 2444.84).

Circularity was compared in control and expanded groups as a measure of whether the expansion of nuclei was spatially linear (Figure 3.3). There was a significant increase in circularity of nuclei in expanded tissue although the effect size was very small with only a 0.006 increase in the circularity quotient post expansion, which ranges from 0 to 1 ($P<0.001$, F ratio= 13.459). This small increase in circularity post-expansion could be a result of increasing the ability to resolve nuclei or due to the cell types that were sampled.

Next, it was tested if there was a difference between runs 1-3 of ProExM tissue expansion in the Feret diameter, area, or circularity of expanded nuclei. The aim of this analysis was to test how consistent each run of ProExM tissue expansion was. It was found that there was a significant difference across runs 1-3 in Feret diameter ($P<0.001$, F ratio= 32.62) and area ($P<0.001$, F ratio=35.27) but not circularity ($P=0.815$, F ratio=0.20), indicating that the size of the expansion did vary between runs. This is reflected in the expansion factors calculated for each expansion (Section 2.5.1) which for runs 1-3 were 4.76 (control n = 117 nuclei, expanded n = 95), 4.26 (control n = 96, expanded n = 78) and 5.00 (control n = 164, expanded n = 135) respectively. These differences in the size of the expansion could have arisen due to small variations in the protocol (Table 3.1), different tissue types and ages that were used (Table 3.1), or due to the expected variability of ProExM between runs (Tillberg et al, 2016).
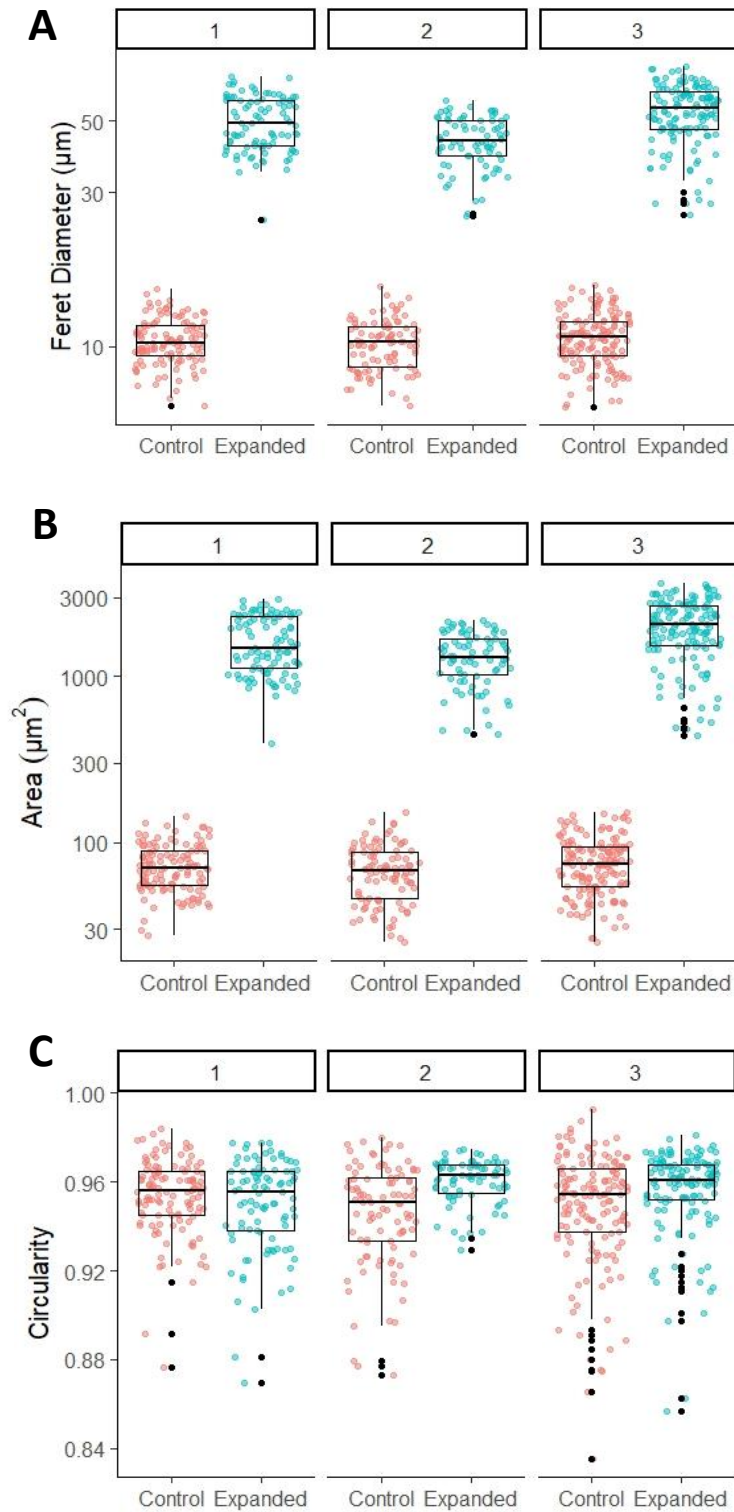
Figure 3.3: Quantifying the size and linearity of expansion.

Measurements of individual nuclei in control, unexpanded tissue (pink) and in tissue expanded by ProExM (blue). Measurements made to quantify nuclei size include (A) Feret Diameter (B) Area and (C) Circularity. 1-3 represents 3 separate runs of ProExM.

Within each run, 2 slices were expanded and imaged for data acquisition. Subsequent non-parametric analysis showed a significant difference in Feret diameter (P<0.001, standardised test statistic = 3.935, number of nuclei, n=130) and area (P<0.001, standardised test statistic = 3.669, number of nuclei, n=130), but not circularity (P>0.05, standardised test statistic = 1.696, number of nuclei, n=130), between two slices, denoted A and B, within the same run of ProExM (Figure 3.4). As a result, proceeding experiments used one slice per run to reduce the unaccounted variance in these data.
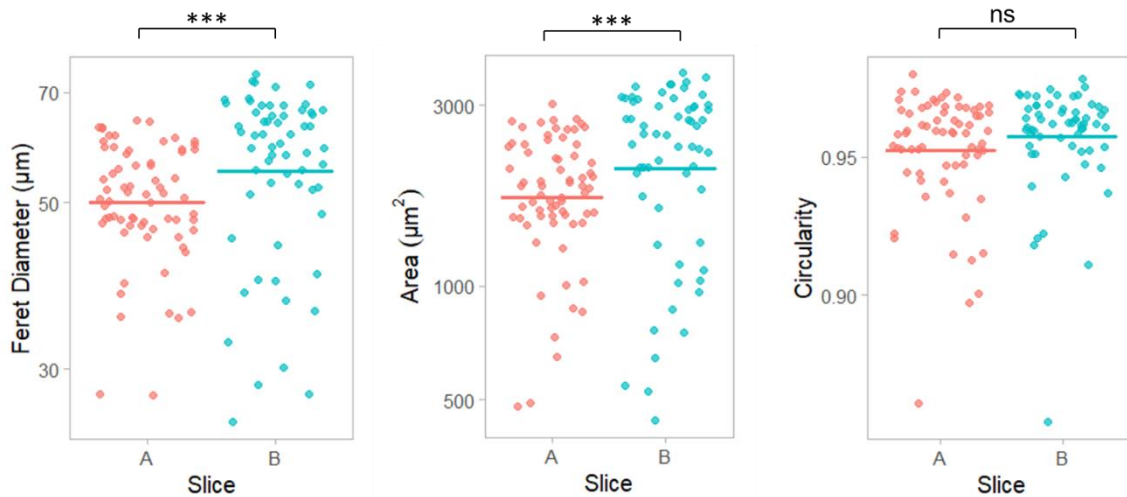
Figure 3.4: Comparing the size of expansion between two tissue slices.
Measurements of Feret diameter, area, and circularity of cell nuclei from two expanded slices, A (pink) and B (blue), within one run of ProExM. Measurements were made from DAPI-labelled nuclei imaged using widefield microscopy. ***p<0.001. ns = p>0.05.

3.1.2 Using a fixed protocol to determine the size of the expansion across multiple runs

The initial optimisation trials pooled data with several confounds including changes in the protocol, and different ages and types of mouse brain tissue (Table 3.1). Variability between individual expanded slices per run was also not accounted for (Figure 3.4). It was therefore necessary to quantify the size of the expansion using one fixed protocol based on the ProExM optimisations made in section 3.1.1, and to use one tissue type. Slices of rTg4510 mouse tissue used to model tauopathy-neurodegeneration was labelled with far red nuclear stain, TO-PRO-3, were expanded and imaged using confocal microscopy (Figure 3.5). For these experiments, expanded slices were placed in imaging chambers and immobilised using 2% agarose.
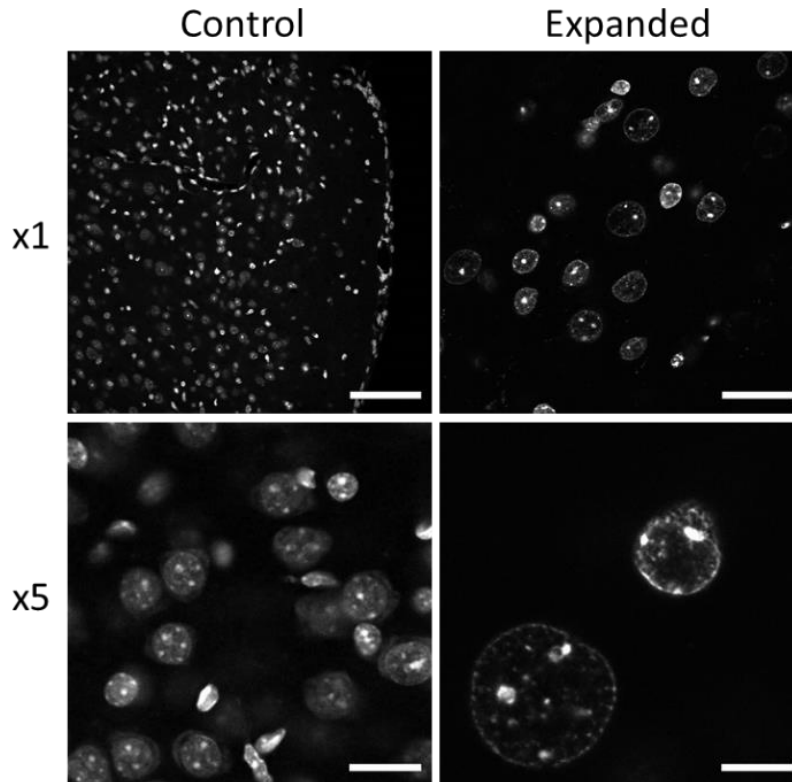
Figure 3.5: Expansion of TO-PRO-3-stained cortical tissue.
Confocal images of rTg4510 mouse LII/III neocortex showing TO-PRO-3 labelled nuclei in of unexpanded (control) and expanded tissue slices. Top row: images taken with no digital zoom, scale bar = 100 μm. Bottom: images taken with 5x digital zoom, scale bar = 20 μm.

Nuclei measurements of Feret diameter, area, and circularity were obtained from 4 control (unexpanded) slices and 4 expanded slices (Figure 3.6). These data confirmed that ProExM resulted in a significant increase in nuclei size (Feret diameter and area) following expansion compared to control slices (P<0.001, standardised test statistic = 8.83, Mann Whitney U).

There was also a significant difference in circularity between control and expanded groups (P<0.001, standardised test statistic: -4.287), but in contrast to Figure 3.3.C, a reduction in circularity was observed. Average circularity measured from control nuclei was 0.924, compared 0.888 from expanded nuclei. The size of the expansion calculated as the size of nuclei per expanded slice relative to the average size across all unexpanded slices ranged from 3.64-4.08 (Table 3.2).

To analyse how variable the expansion was between samples, nuclei measurements were compared between expanded slices 1-4. There was no significant difference in Feret diameter or area between the different expanded slices (P>0.05, F ratio = 0.523, one-way independent ANOVAs). In addition, variance was equal across expanded slices, demonstrating a consistency from run to run which contrasts with the initial optimisation trials shown from the data in Figure 3.3 As Figure 3.6.C would suggest, there was a significant difference in circularity across slices 1-4 (P=0.16, test statistic = 10.35, Kruskal-Wallis test). This could be

an indicator of non-linearity in the expansion, however other factors like the cell types sampled would need to be considered before making this assumption.
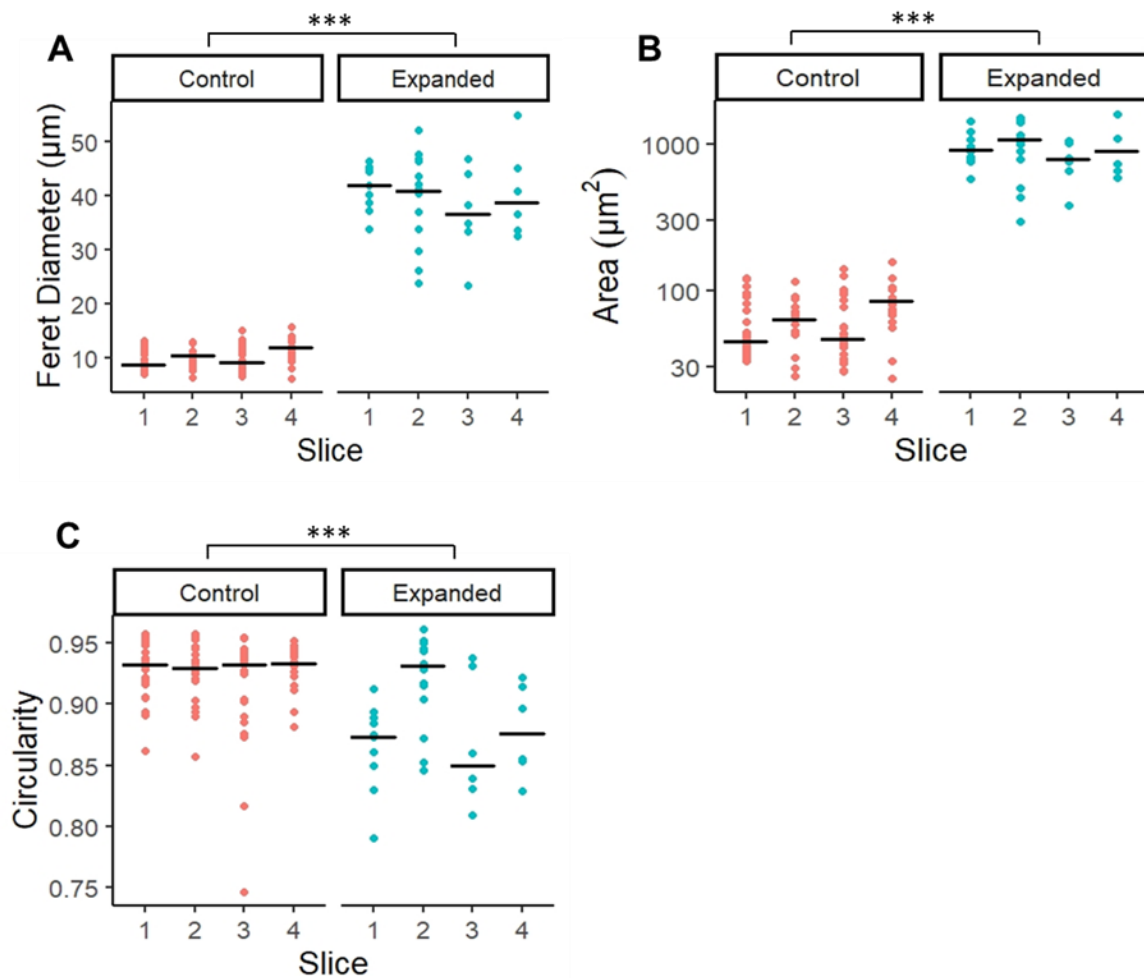
Figure 3.6: Quantifying the size and linearity of expansion across multiple tissue slices.
*Measurements of individual nuclei from layer II/III of neocortex in 4 control, unexpanded slices (pink) and 4 expanded slices (blue). Measurements made include (A) Feret Diameter (B) Area, and (C) Circularity. Crossbars show median values per slice. ***P<0.001.*

Expanded Slice	Mean Feret Diameter	Expansion Factor
1	41.22 ± 1.17	4.08
2	39.13 ± 2.23	3.87
3	36.83 ± 3.39	3.64
4	40.59 ± 3.47	4.02

Table 3.2: Expansion factors for Figure 3.6.
Expansion factors for expanded slices 1-4 as determined by the ratio of mean Feret diameter per slice to the total mean Feret diameter of all control slices (1-4).
Control mean Feret diameter= 10.10061 μm.

3.2. Expansion microscopy improves resolution of tau fibrils in rTg4510 mouse brain tissue

3.2.1. PG-5 immunohistochemistry is compatible with expansion microscopy

The next series of experiments aimed to demonstrate that ProExM was compatible with antibodies for tau, and that by applying ProExM, the ability to resolve tau fibrils is improved. These experiments used rTg4510 mouse brain tissue at 4 months of age, prior to significant cell loss or NFT accumulation (Ramsden et al, 2005; SantaCruz et al, 2005). As this was relatively early in tauopathy-driven neurodegeneration, the antibody PG-5 was selected for preliminary studies. This antibody binds to tau phosphorylated at the ser409 residue known to be an early indicator of hyperphosphorylation, but is not dependant on a specific conformation of tau misfolding (i.e. PHFs) (Ramsden et al, 2005).

Tau antibodies had not previously been used in combination with ProExM so first it was demonstrated that PG-5 was compatible with this technique and that signal was not degraded during the digestion phase of expansion. Confocal imaging of rTg4510 cortical slices immunolabelled with PG-5 and expanded via ProExM show fluorescence was retained post-expansion (Figure 3.7). Nuclei were also stained using TO-PRO-3 so that tau aggregates in the soma could be distinguished clearly from extra-somatic labelling. Imaging settings were adjusted from unexpanded to expanded conditions as overall fluorescence intensity post-expansion did decrease. This was done by keeping pixel fluorescence intensity distribution within the linear range of detectors. As an example of this, an expanded PG-5 and TO-PRO-3 labelled slice was imaged with the same settings as unexpanded tissue (Figure 3.8) which demonstrates that these settings were suboptimal.

Some interesting observations of PG-5 labelling in rTg4510 tissue were made when testing the compatibility of this antibody with ProExM. Firstly, somatic tau aggregation did appear relatively extensive throughout cortical layers II-V/VI, and across cortical regions that included the prefrontal cortex (PFC) and somatosensory cortex (SSC). This indicated that at this age moderate tau accumulation in the rTg4510 mouse cortex had taken place. In addition, the expansion did not clearly change the overall distribution and pattern of tau staining. Intracellular tau aggregation between cells within the same cortical area varied in extent and morphology (Figure 3.9).
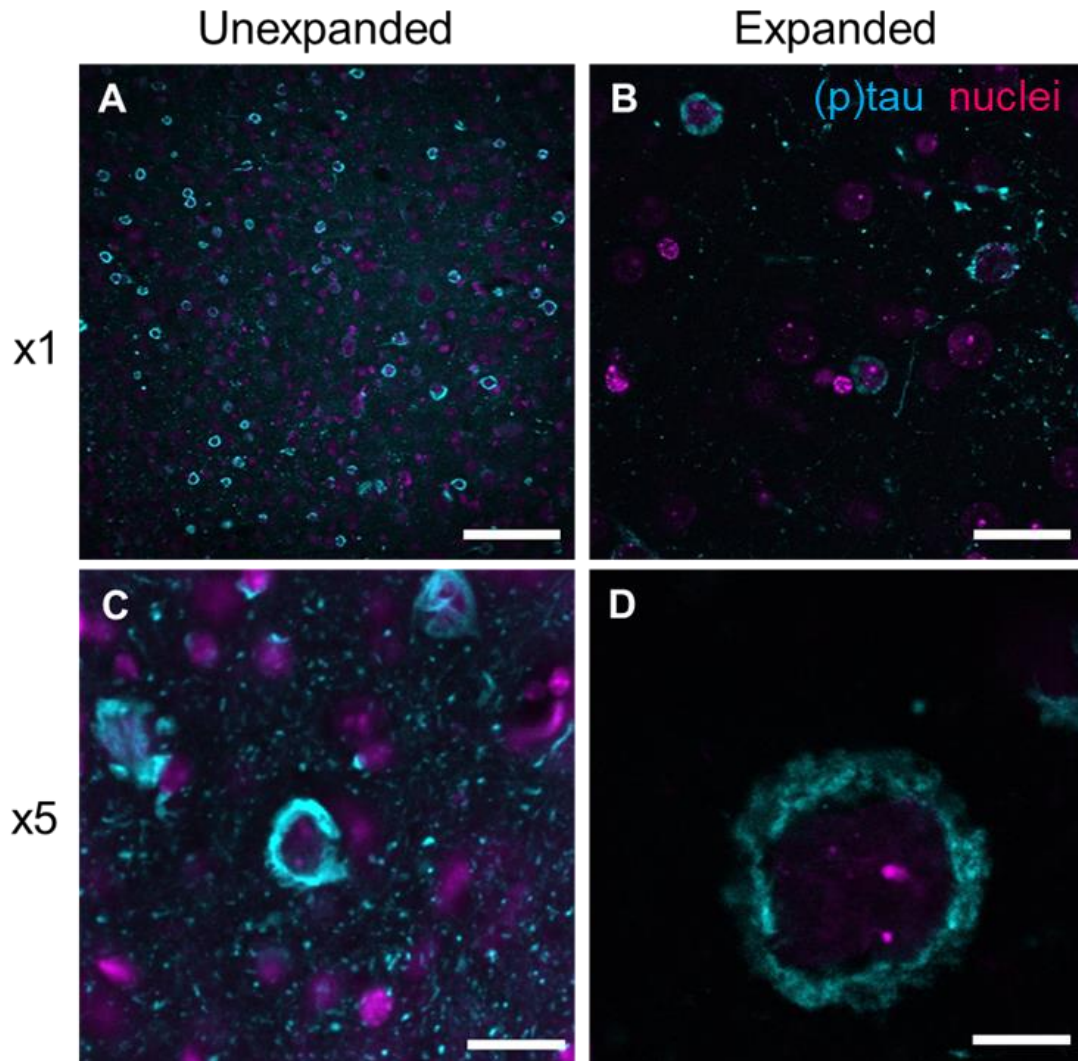
Figure 3.7: PG-5 and TO-PRO-3 labelled rTg4510 mouse cortex.

Confocal microscopy images of rTg4510 mouse cortex showing PG-5-labelled phosphorylated tau (cyan) and TO-PRO-3 labelled nuclei (magenta). Top row: images of (A) unexpanded and (B) expanded slices taken with no digital zoom, scale bar = 100um. Bottom row: images taken of (C) unexpanded and (D) expanded slices with 5x digital zoom focusing on a region of intracellular tau aggregation, scale bar = 20 μm. Expansion factor for (B) was 3.85. Expansion factor for (C) was 4.02.
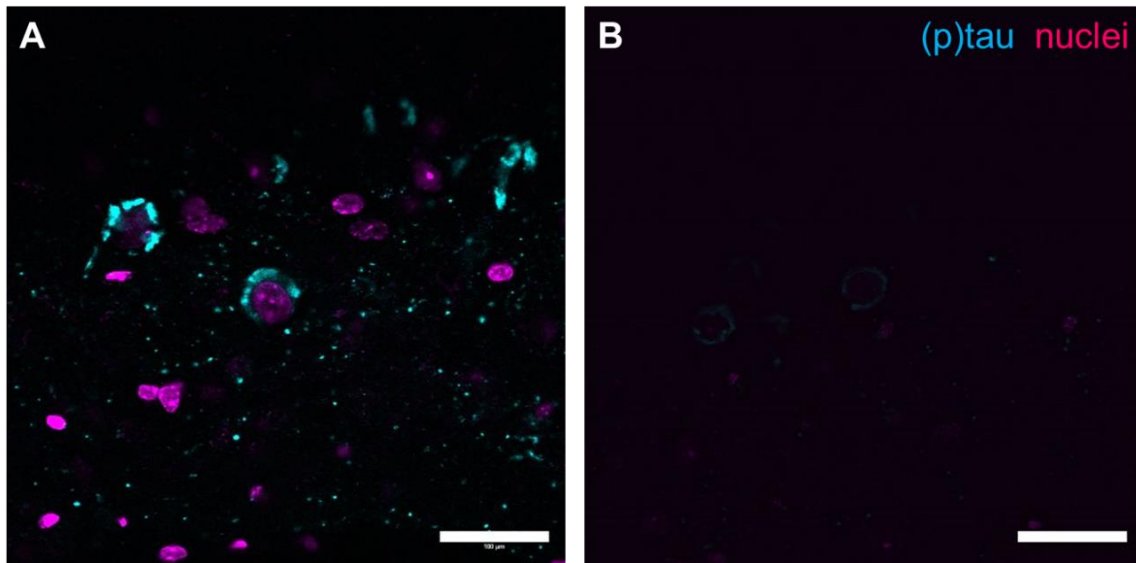
Figure 3.8: Adjustment of confocal imaging settings required for expanded tissue.
Confocal images of expanded tissue labelled with TO-PRO-3 (magenta) and PG-5 (cyan). This sample was imaged using (A) standard settings for expanded slices, and (B) settings that were applied to unexpanded tissue. Scale bars = 100 μm.
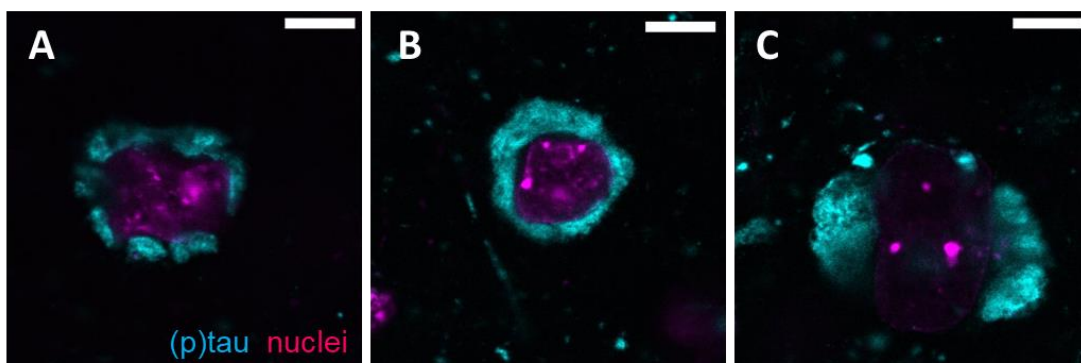
Figure 3.9: Intracellular tau aggregation in rTg4510 mouse cortex.
Confocal images of intracellular tau aggregation in different cells within L2 neocortex of an expanded tissue slice. Nuclei were labelled with TO-PRO-3 (magenta) and (p)tau was labelled with PG-5 immunohistochemistry (cyan). All images taken with 5x digital zoom. Scale bars = 20 μm. Expansion factor: 4.02.

3.2.2. Confirming specificity of PG-5 immunohistochemistry

Controls for PG-5 immunohistochemistry were performed to confirm that the labelling observed in Figure 3.7 and Figure 3.9 was specific to phosphorylated tau. Primary and

secondary controls were established where the standard immunohistochemistry protocol was followed (Section 2.2.5) but the secondary or primary antibody was omitted respectively. In doing so, the primary control for PG-5 tested whether there was autofluorescence from the tissue that could be mistaken for PG-5 labelling. The secondary control tested for non-specific staining of the secondary antibody in this tissue type as well as the degree of background labelling.

Primary controls from these results showed no autofluorescence from the tissue (Figure 3.10). Very limited non-specific labelling was present in the transgenic tissue. A small degree of background florescence was observed in both control and expanded slices yet this was clearly distinguishable from PG-5 immunolabelling.
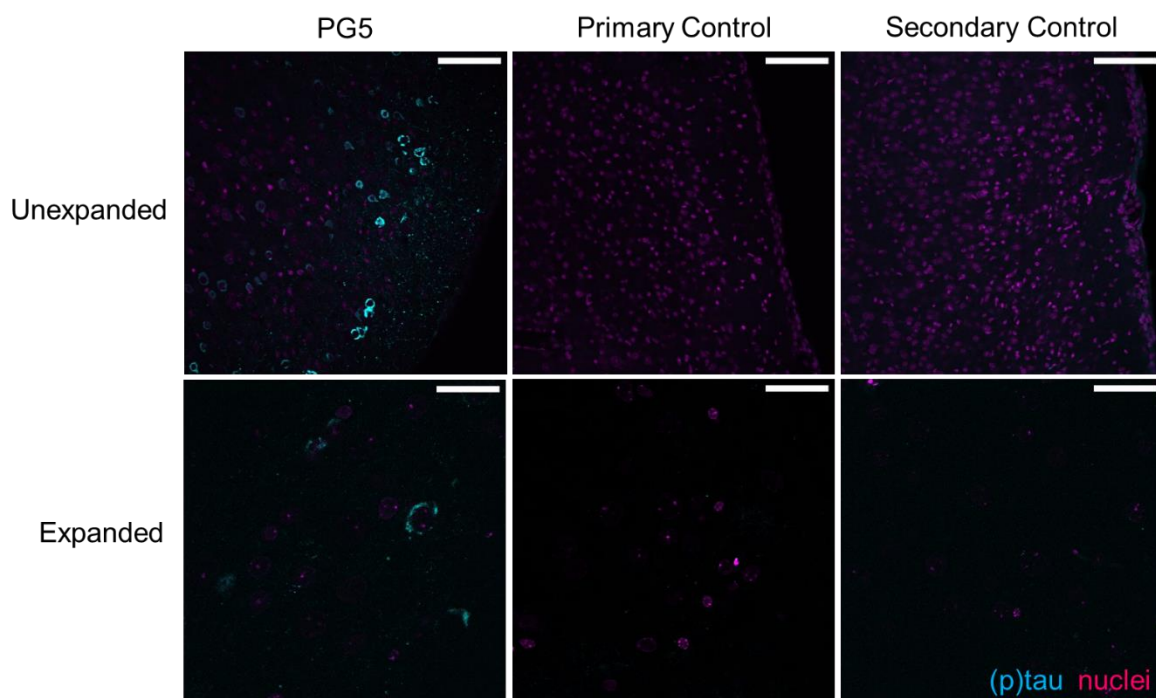
Figure 3.10: Controls for PG-5 immunohistochemistry.

Confocal images of layer 2 neocortex of primary (middle) and secondary (right) controls in relation to PG-5 immunohistochemistry (cyan). For reference, nuclei are shown in greyscale. Top row: controls for unexpanded tissue slices. Bottom row: controls for expanded tissue slices. Scale bar: 100 µm. Expansion factor: 3.85.

To confirm the specificity of tau staining, PG-5 immunohistochemistry was also tested on age-matched wildtype littermate tissue. In this tissue type, pathological tau accumulation would not be present under normal conditions. Results from this control support this, showing no tau-like staining (Figure 3.11). From these controls overall, it is clear that PG-5 immunohistochemistry in this protocol was specific to (p)tau.
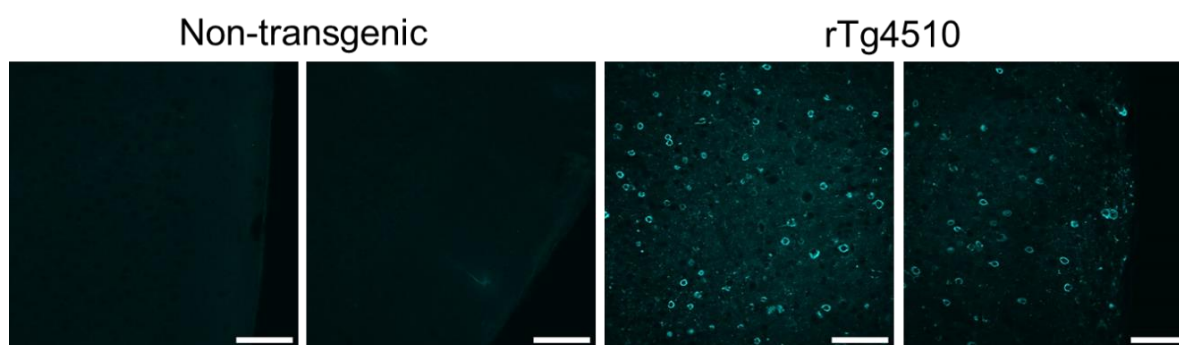
Figure 3.11: PG-5 immunolabelling in rTg4510 vs non-transgenic tissue.

Confocal images of mouse cortex immunolabelled for (p)tau (via PG-5) in non-transgenic wildtype tissue, and in rTg4510 tissue. These images were obtained from unexpanded tissue slices. Scale bar = 100 μm.

3.2.3. Applying alternative confirmation-dependant tau antibodies to 4-month-old rTg4510 mouse tissue

Based on the observation that PG-5-(p)tau immunolabelling at 4 months showed relatively extensive tau pathology, antibodies for different conformations of tau were used on this tissue type. The aim of these experiments was to characterise the type of tau aggregation based on the specificity of different primary antibodies. The following antibodies were used, as described in the methods (Section 2.2.3.):

- PHF-1: Specifically recognises tau protein phosphorylated at serine residues 396 and 404 (PHFs)
- MC-1: Confirmation dependant antibody that recognises both early and late stage tau pathology
- DA9: Total tau (phosphorylation independent)

Immunohistochemistry for PG-5, PHF-1, MC-1 and DA9 was performed in unexpanded tissue slices (Figure 3.12). Overall, the immunolabelling from these 4 antibodies was very similar to previous observations i.e. Figure 3.7. This was expected, as NFTs, pre-tangles and PHFs would be labelled with PG-5 which does not bind to a specific conformation of tau misfolding. At 4 months in these rTg4510 mice there was already significant pre-tangle and NFT accumulation as identified by PHF-1, MC-1 and PG-5 (Figure 3.12). As was initially observed with PG-5, the tau aggregation identified with all 4 antibodies was seen in cortical layers II-V/VI and with similar density of labelling.
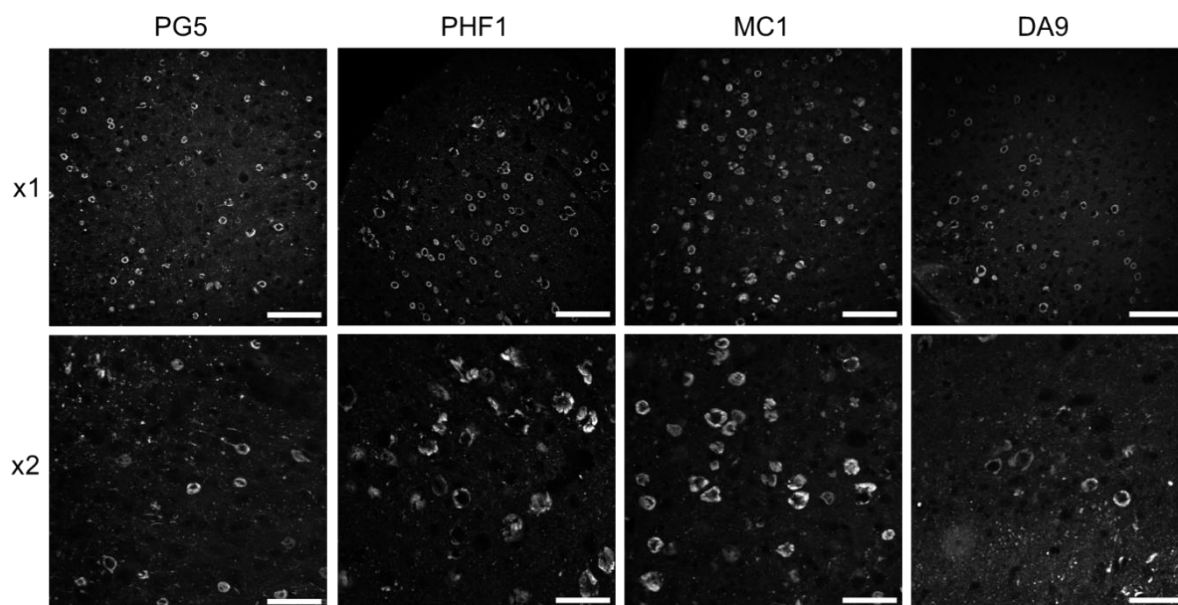
Figure 3.12: Immunoreactivity of alternative tau antibodies in rTg4510 mouse cortex.
Confocal images of layer 2 neocortex in unexpanded tissue labelled with PG-5, PHF-1, MC-1 and DA9 primary antibodies. Top row: no digital zoom, scale bars: 100 μm. Bottom row: x2 digital zoom, Scale bars: 100 μm.

3.2.4 Expansion microscopy improves resolution of PG-5 labelled tau fibrils

A key proof of concept for ProExM was to demonstrate that, by physically expanding labelled tissue, imaging resolution was improved beyond what could be achieved in unexpanded tissue slices with confocal microscopy. To demonstrate this, a quantitative technique was used to validate that ProExM improves the ability to resolve PG-5 labelled tau fibrils.

Images had been obtained from multiple runs of ProExM showing tau aggregation around a nucleus (i.e., Figure 3.9). The aim was to compare the resolution of tau fibrils achieved in these images to confocal images of tau aggregates in unexpanded tissue that had instead been digitally zoomed in to increase resolution. As such, images were collected such that the size of the intracellular tau aggregate and nucleus was approximately matched in images from both expanded and control tissue (Figure 3.13).
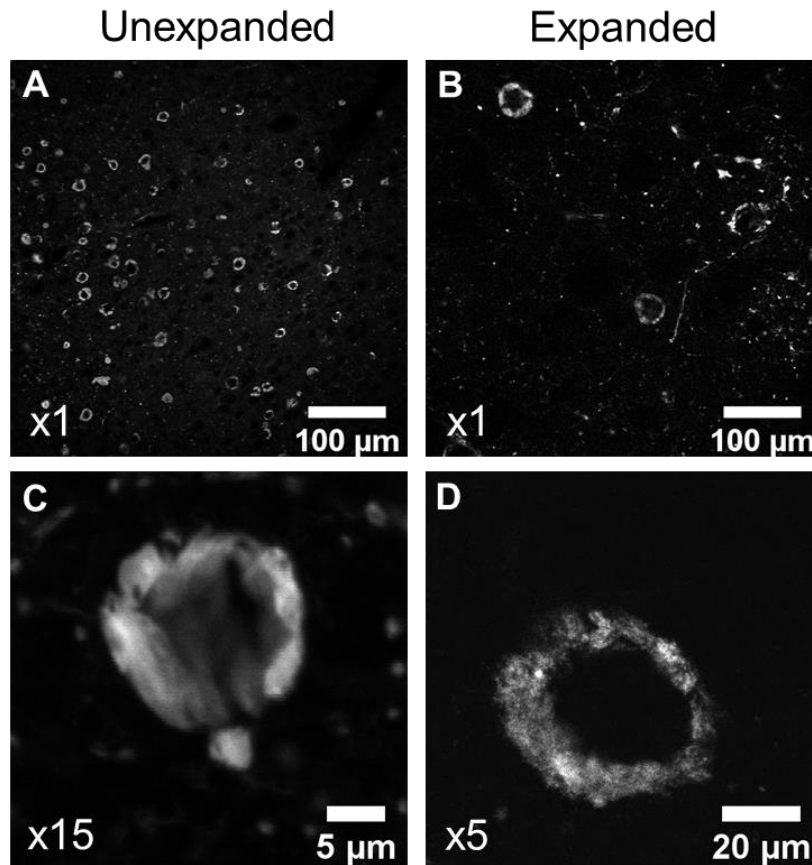
Figure 3.13: Resolution of tau in unexpanded vs expanded rTg4510 cortical tissue.
Confocal images of rTg4510 cortical tissue labelled with PG-5. Top row: a comparison of the field of view from an (A) unexpanded and (B) expanded sample. Bottom row: aggregation of tau fibrils that had been imaged (C) in unexpanded tissue using x15 digital zoom, and (D) in expanded tissue using x5 digital zoom.

Images were obtained from multiple slices of one rTg4510 mouse brain (Expanded, x5 zoom = 4 slices; Unexpanded; x15 zoom = 5 slices). To assess the resolution of PG-5 labelled tau structures in the images, the fluorescence intensity profile was measured across intersecting lines through the cell body (Methods, 2.5.2). This allowed detection of local maxima (of pixel intensity) of the PG-5 signal. Since tau structures are molecular filaments, higher resolving power would allow detection of narrower and more numerous fluorescence peaks as greater detail is revealed.

Overall, a sample of 38 unexpanded images across 5 slices and 23 expanded images across 4 slices were used. Images from the unexpanded condition were clearly more blurred, indicating lower resolution of tau fibrils as expected. To quantify this, peaks were identified on these images along the vertical and horizonal midlines. The total number of peaks per image, and the widths of each peak per image, was obtained (Figure 3.14).
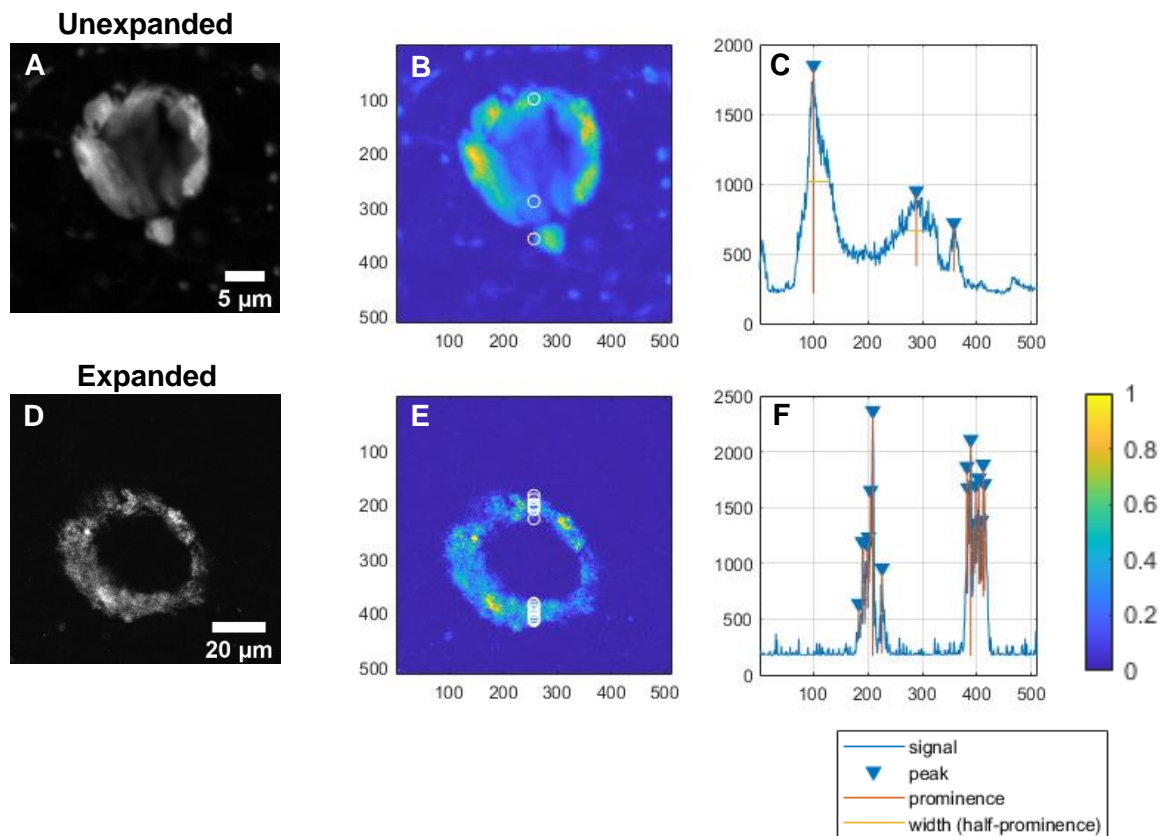
Figure 3.14: Identification of peaks in the intensity profile of confocal images of tau fibrils.

Identification of peaks in pixel intensity from confocal images of tau aggregation from (A-C) unexpanded and (D-F) expanded rTg4510 PG-5 labelled tissue. The location of peaks along the vertical midline of images A and D are indicated by white circles on the corresponding heatmap images B and E. Plots of pixel intensity are shown for the (C) unexpanded and (F) expanded conditions.

Measurement of fluorescence intensity peaks showed that significantly more peaks were identified in images from the expanded condition compared to unexpanded (P<0.001, Standardised test statistic: 5.135, Mann Whitney U, number of images, n=61) (Figure 3.15.A). Mean values for the total number of peaks identified per image from the unexpanded condition were 7.41 ± 0.61, and from the expanded condition were 18.17 ± 1.91, suggesting that expansion allowed the detection of approximately 2.5x more individual tau structures. In addition, there was no significant difference in the number of peaks identified between expanded slices 1-4 (P=0.204, F ratio = 1.686 number of images, n=23, one-way ANOVA) (Figure 3.15.A).

The width of the peaks identified was compared in expanded and unexpanded conditions as an alternative measure of improved resolution. The mean width of peaks in the expanded

condition was significantly less than mean peak width from the unexpanded condition (P<0.001, standardised test statistic = -15.224, Mann-Whitney U, number of images, n=61). For unexpanded and expanded images, mean peak width was 20.41 ± 1.02 pixels, and 3.8 ± 0.22 pixels respectively (Figure 3.14.B). The detection of significantly narrower peaks in intensity after tissue expansion demonstrated an improved ability to resolve narrow tau filaments when using ProExM to improve resolution. For each expanded slice, expansion factor and mean peak widths values are summarised in Table 3.3.
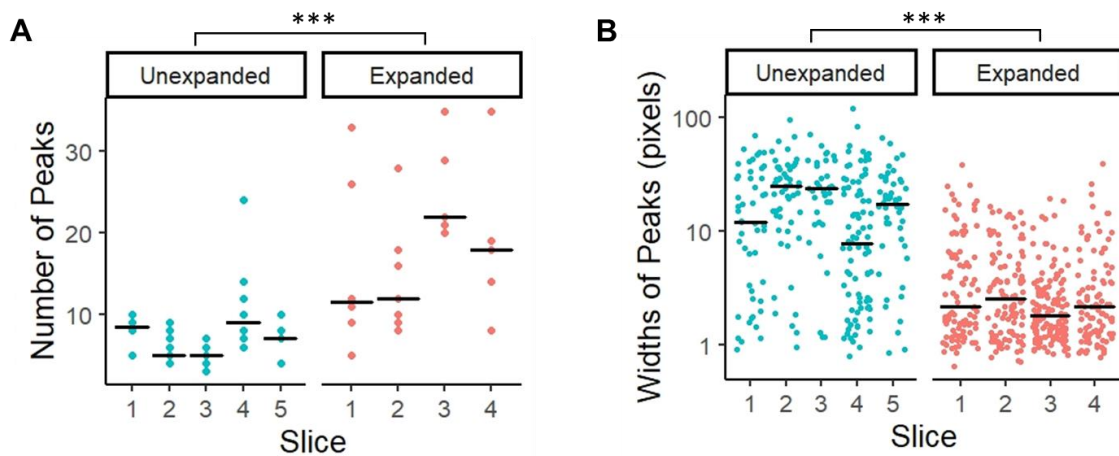
Figure 3.15: Improved resolution of tau fibrils post expansion.

*Measurements of (A) total number of peaks and (B) width of peaks identified from confocal images of rTg4510 PG-5 labelled mouse tissue that was either unexpanded and imaged with x15 digital zoom (blue), or expanded and imaged with x5 digital zoom (pink). Total number of peaks in (A) was the sum of peaks identified across the horizontal and vertical midline per image. Crossbars reflects the median values from these data. ***P<0.001.*

Slice	Expansion factor	Mean no. of peaks	Mean peak width
1	4.02	16.00 ± 4.47	5.05 ± 0.64
2	3.98	14.43 ± 2.65	3.80 ± 0.44
3	4.38	25.40 ± 2.87	2.66 ± 0.24
4	3.85	18.80 ± 4.49	4.08 ± 0.42

Table 3.3: Expansion factors for Figure 3.15.

Comparison of expansion factor to the mean number of peaks and mean peak width identified in confocal images of tau aggregation. Mean values are displayed ±SEM.

3.3. Demonstrating the presence of (p)tau at synapses using ProExM

3.3.1. Using ProExM and immunohistochemistry to identify (p)tau at synapses in 4-month-old rTg4510 mouse brain tissue

Evidence from biochemical and physiological studies have indicated that when P301L tau is overexpressed, (p)tau is mislocated to dendritic spines and disrupts postsynaptic function (Hoover et al, 2010; Miyamoto et al, 2017; Pallas-Bazarra et al, 2019). This is concomitant with an increase in synaptic turnover and reduction in dendritic spine size *in vivo* (Jackson et al, 2017). However, at present anatomical studies demonstrating the presence of (p)tau at dendritic spines have been limited by light resolution as synapses and tau fibrils are too small to resolve with conventional fluorescence microscopy. In this section, ProExM was used to increase resolution of ultrastructure in rTg4510 tissue so that the presence of (p)tau at synapses could be shown in greater detail.

rTg4510 mouse tissue was expanded using the ProExM tissue expansion protocol outlined in 3.1 and 3.2, and labelled with PG-5 and TO-PRO-3. Expanded tissue showed somato-dendritic localisation of (p)tau in LII cortex (Figure 3.16) consistent with pre-tangle and NFT formation (Figure 1.2.A-B). To test whether tau was specifically located at dendritic spines, colocalisation analysis of (p)tau with a marker for dendritic spines or synapses was required. Antibodies for synaptic proteins Bassoon and Homer1 were used as markers for the presynaptic and postsynaptic site respectively as previous studies had demonstrated that this was compatible with expansion microscopy (Chang et al, 2017; Truckenbrodt et al, 2018). Where Bassoon and Homer1 were identified in close proximity, i.e. <1 μm in expanded tissue, equivalent to 0.25-0.28 μm when adjusted for expansion, suggested the presence of a synapse.
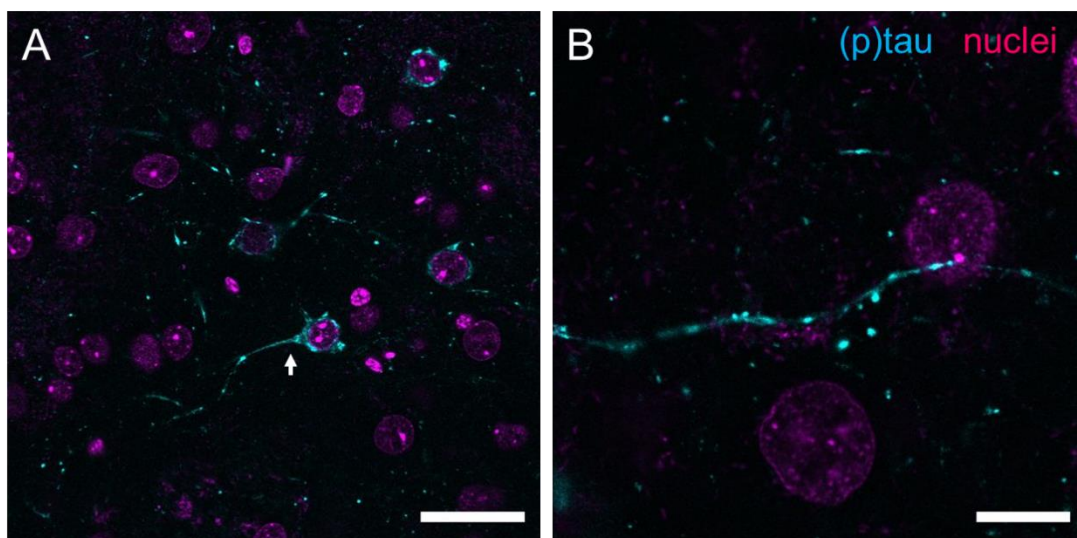
Figure 3.16: Somato-dendritic localisation of tau.
Confocal microscopy images of rTg4510 mouse cortex showing somato-dendritic

Prior to expanding tissue, immunohistochemistry was optimised by triple-labelling rTg4510 tissue with PG-5, Bassoon and Homer1 (Figure 3.17). Bassoon and Homer1 could be visualised in rTg4510 tissue throughout all brain regions observed. When channels were overlayed, it became clear that areas of PG-5 immunolabelling overlapped extensively with Bassoon and to a lesser extent Homer1 (Figure 3.17; overlay). Controls for immunohistochemistry of Homer1 and Bassoon in rTg4510 mouse tissue are presented in Figure 3.23 and will be discussed further in section 3.3.2.
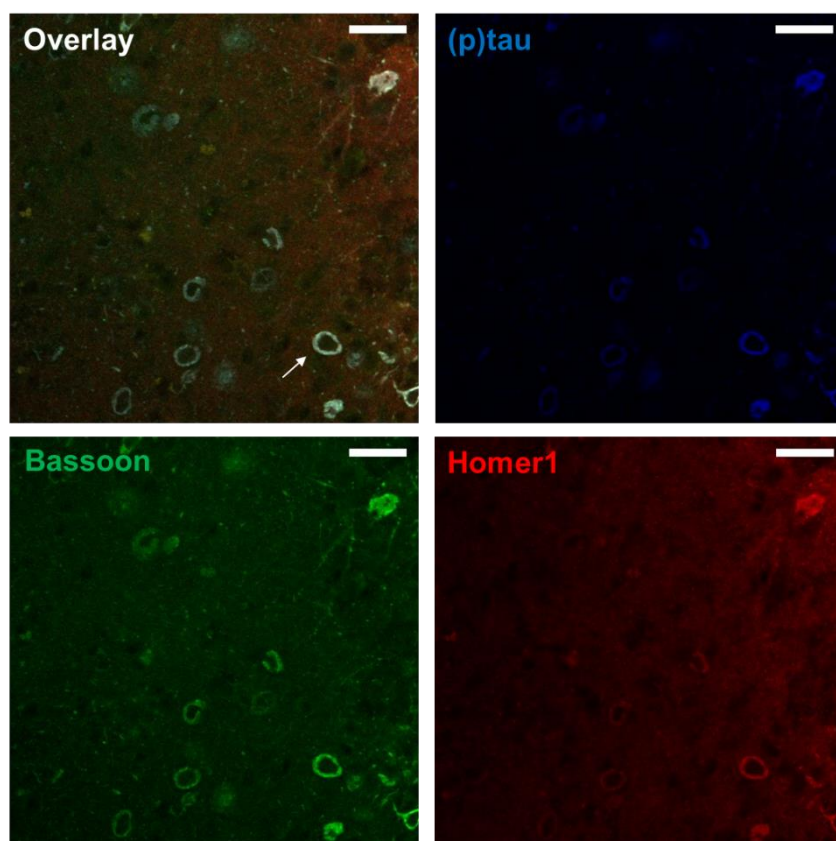
Figure 3.17: PG-5, Homer1 and Bassoon immunolabelling in rTg4510 mouse cortex.
Confocal images of rTg4510 mouse cortex (unexpanded) labelled with antibodies for (p)tau (PG-5, blue), Bassoon (green) and Homer1 (red). Images represent the same field of view as the overlay (top left) but each channel is also shown separately. The white arrow shows a region of overlapping signal from all 3 channels. Scale bar: 30 μm.

Direct overlapping signal of PG-5, Bassoon and Homer1 as seen in Figure 3.17 posed a significant issue in reliably demonstrating (p)tau presence at synapses as it was not clear at

this stage if this observation was an artefact from immunohistochemistry. Potential reasons as to why this occurred include:

1. Crosstalk between channels
2. Homer1 and Bassoon immunolabelling was real / finding was not an artefact of immunohistochemistry
3. Non-specific binding of primary antibodies for Bassoon and Homer1 to areas of PG-5 labelling (Figure 3.23)
4. Non-specific binding of secondary antibodies to PG-5/(p)tau (Figure 3.23)
5. Autofluorescence of the tissue (Figure 3.23; 3.24)

Channel crosstalk was ruled out early on by using sequential scanning on the confocal microscope and narrowing the range of emission light received for each fluorophore. To investigate the overlapping signal between all three channels shown in Figure 3.1, higher magnification images were taken on unexpanded, triple-labelled tissue (Figure 3.18). By increasing the magnification, Homer1 and Bassoon puncta could be resolved (Figure 3.18.B). It did not appear that PG-5, Bassoon and Homer1 immunolabelling were directly overlapping, but that in areas where (p)tau was present, there was a higher density of synaptic marker staining that could not clearly resolved in lower magnification images (Figure 3.18.C-E).

(p)tau   **Bassoon**   **Homer1**
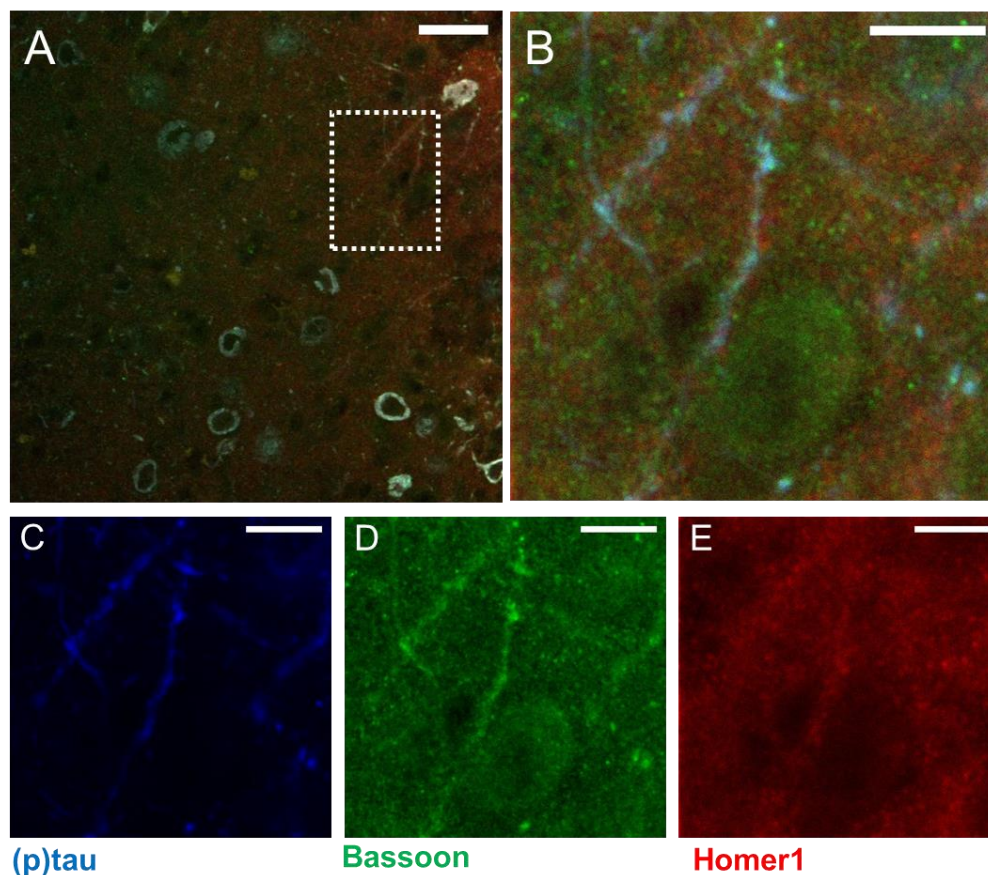
Figure 3.18: Higher magnification confocal images of PG-5, Homer1 and Bassoon.
Confocal images of rTg4510 mouse cortex labelled with antibodies for (p)tau (PG-5, blue),

Another region of interest was selected in addition to Figure 3.18.B and these images were enlarged to study the extent to which synaptic markers and (p)tau could be resolved in unexpanded rTg4510 tissue (Figure 3.19). By zooming into regions of interest, punctate Homer1 and Bassoon immunolabelling could be seen in relation to (p)tau (Figure 3.19.B-C,E-F). However, the resolution of these images was poor and co-localised puncta of Bassoon and Homer1, indicating synapses, could not clearly be distinguished from background signal.

(p)tau Bassoon Homer1
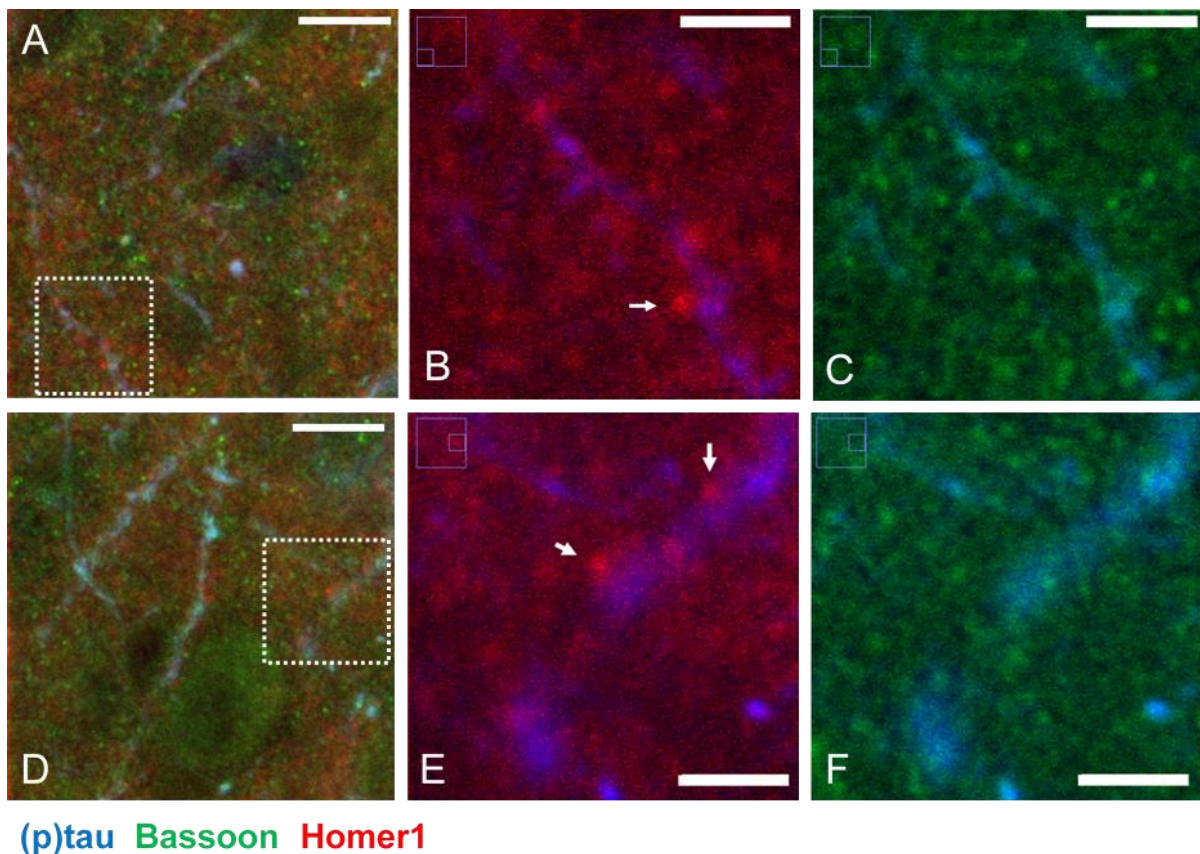
Figure 3.19: Colocalisation of (p)tau to Homer1 or Basoon.
Confocal images of rTg4510 mouse cortex labelled with antibodies for (p)tau (PG-5, blue), Bassoon (green) and Homer1 (red). (A) and (D) show two different fields of view within one tissue slice; white boxes correspond to the enlarged view of these images in (B-C) and (E-F) respectively. In (B) and (E), (p)tau and Homer 1 signal is overlayed; arrows show colocalisation of Homer1 and (p)tau. In (C) and (F) Bassoon and (p)tau signal is overlayed. Scale bar for (A,D): 10 μm, (B,C,E,F): 4 μm.

To increase resolution of synaptic markers and (p)tau immunolabelling, tissue slices were expanded using ProExM. Figure 3.20 compares the field of view for unexpanded and expanded tissue triple labelled with PG-5, Bassoon and Homer1. Individual channels for Figure 3.20.B are shown in Figure 3.20.C-E. By increasing the size of the tissue sample with ProExM, individual synaptic markers could now be resolved at a lower magnification (Figure 3.20.B).
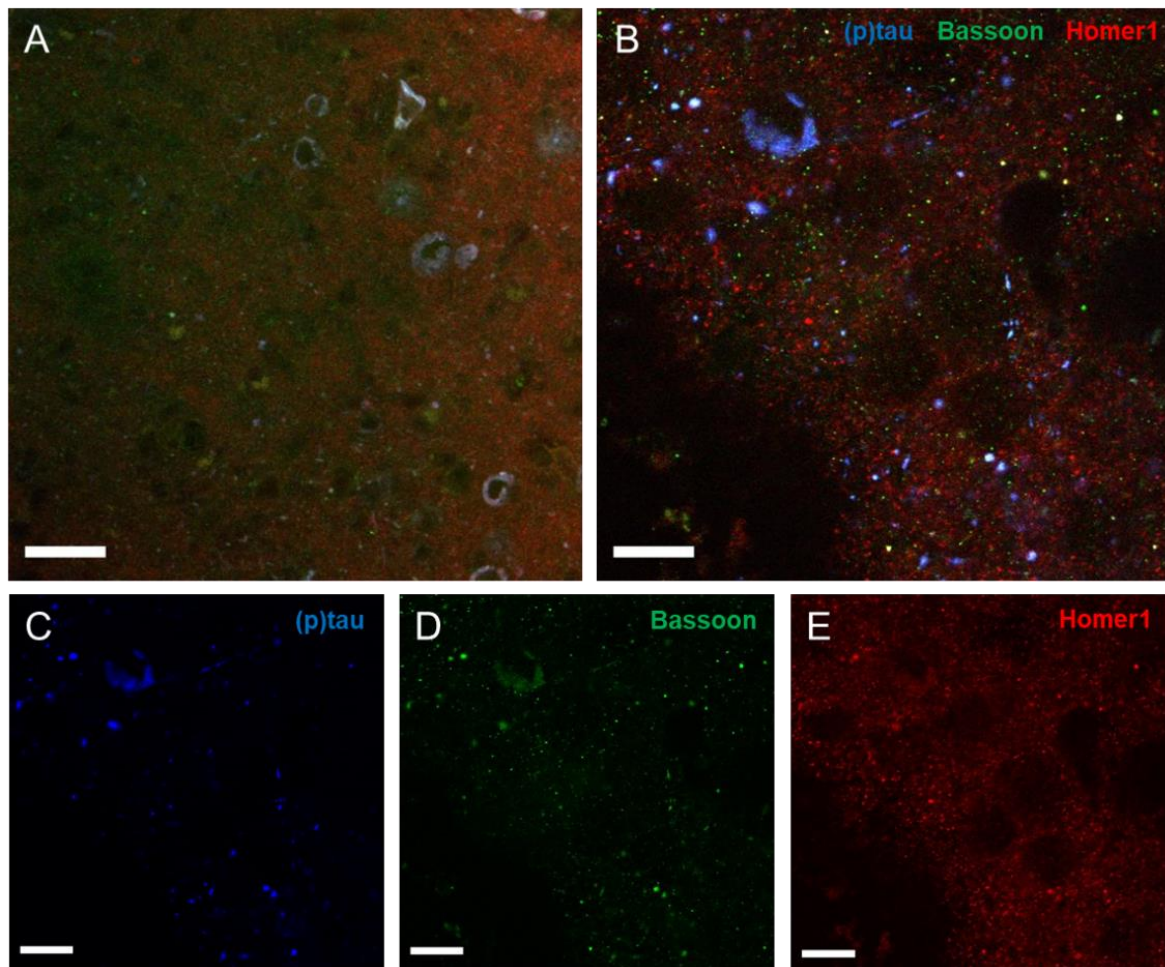
Figure 3.20: PG-5, Bassoon and Homer1 labelled rTg4510 cortex post-expansion (x60).
Confocal images of rTg4510 mouse cortex labelled with antibodies for (p)tau (PG-5, blue), Bassoon (green) and Homer1 (red) in (A) unexpanded and (B) expanded rTg4510 mouse cortical tissue. Each channel in (B) is displayed separately in (C-E). Scale bar: 30 μm.

Figure 3.21 shows the same expanded sample as in Figure 3.20.B, but imaged with a 25x objective. This objective benefitted from a higher numerical aperture, and had a correction collar that could match the glass used in the imaging chamber so that more out of focus light could be excluded than when using the 60x objective in Figure 3.20. Using this objective, it was possible to resolve Bassoon and Homer1 labelled putative synapses (Figure 3.21.B; arrows). However, this objective was not corrected for blue-green emmission wavelengths so

chromatic abberation caused axial displacement of (p)tau signal. As a result, colocalisation of (p)tau to putative synapses identified in Figure 3.21.B would not be reliable using this set up. Individual channels for Figure 3.21.A are shown in Figure 3.21.C-E.
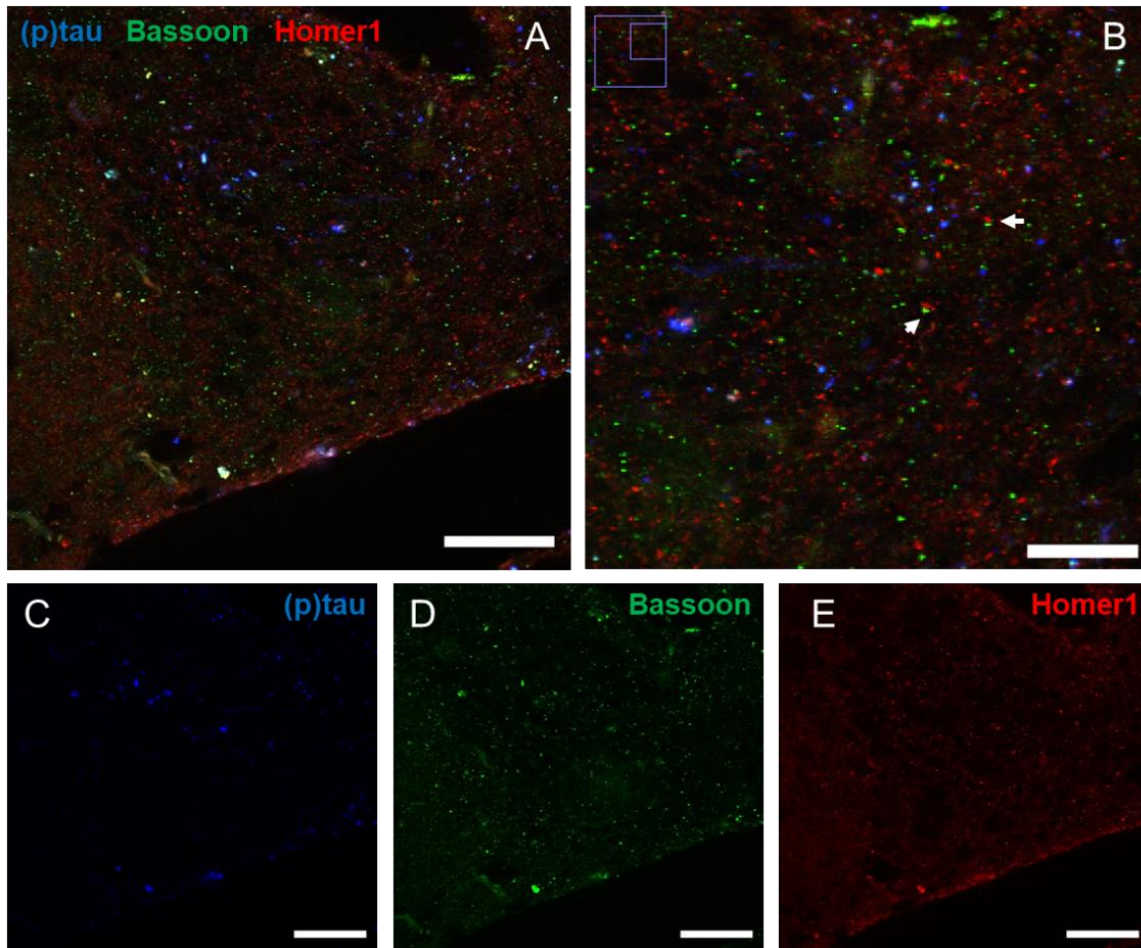
Figure 3.21: PG-5, Bassoon and Homer1 labelled rTg4510 cortex post-expansion (x25). *Confocal images of rTg4510 mouse cortex labelled with antibodies for (p)tau (PG-5, blue), Bassoon (green) and Homer1 (red) and expanded using ProExM. Images were taken using a 25x objective. Arrows in (B) indicate putative synapses due to the close coupling of Bassoon (presynaptic) and Homer1 (postsynaptic) proteins. Each channel in (A) is displayed separately in (C-E). Scale bar for (A): 100 μm, (B): 50 μm.*

The expanded rTg4510 tissue sample in Figure 3.20.B and Figure 3.21 was used to test whether (p)tau could be located to synapses. Initially, using the 60x objective and high digital zoom, putative synapses were identified by colocalisation of Bassoon and Homer1 (Figure 3.22.B, white arrow). It was possible to observe phosphorylated tau at putative synapses although this was not extensive throughout the expanded cortical tissue (Figure 3.22.C-D).

In Figure 3.22.A, red arrows indicate regions where a high degree of colocalisation was observed in all three channels. This signal was similar to non-sepcific autofloroscence observed in controls for immunohistochemistry (Section 3.3.2: Figure 3.23, Figure 3.24).
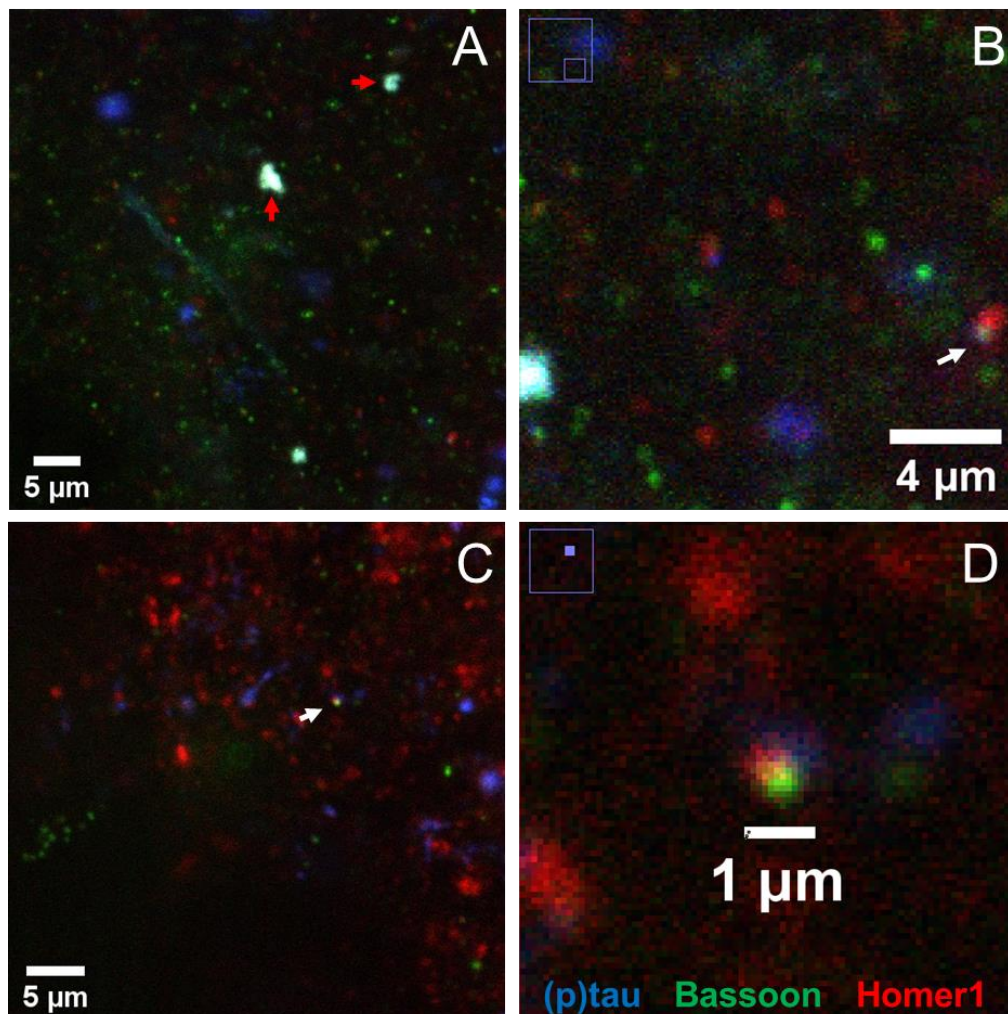
Figure 3.22: (p)tau at putative synapses in expanded rTg4510 mouse cortex.
Confocal images of rTg4510 mouse cortex labelled with antibodies for (p)tau (PG-5, blue), Bassoon (green) and Homer1 (red) and expanded using ProExM. (B) and (D) show enlarged images of a region of interest in (A) and (C) respectively. Red arrows indicate regions where immunolabelling has a high degree of overlap in all three channels. White arrows show couples of Bassoon and Homer1 indicating synapses.

3.3.2. Testing the specificity of Bassoon and Homer1 immunohistochemistry in rTg4510 mouse tissue

In 3.3.1 (p)tau was shown to be located at/near some synapses using immunohistochemistry and ProExM. However, as shown in Figure 3.17.A and Figure 3.22.A (red arrows), there was an unexpectedly high degree of overlapping signal from all three channels in specific areas of

(p)tau labelling. To some extent, this could be due to a higher density of synaptic marker labelling at regions containing (p)tau as suggested in Figure 3.18. However, immunohistochemistry controls were established to test for autofluorescence or non-specific binding (Figure 3.23).

Secondary controls were used to test for non-specific binding of secondary antibody. Bassoon and Homer1 were visualised using Alexa Fluor 555 and Alexa Fluor 633 conjugated secondary antibodies respectively. In both instances, non-specific fluorescence was observed (Figure 3.23.B,E). However, this signal did not resemble intracellular tau aggregation, such as the typical 'ring-shaped' tau aggregation in cell bodies (Figure 3.16).

To test whether this non-specific signal in Figure 3.23.B,E was a result of tissue autofluorescence, blocked, unlabelled tissue was imaged using the same excitation laser wavelengths that were used for detecting Homer1 and Bassoon immunohistochemistry (Figure 3.23.C,F). Autofluorescence emission was observed in channels for both Bassoon and Homer1, and was also visible post-expansion (Figure 3.24). Given that the autofluorescence emitted from the tissue was long ranging, appearing in both Bassoon and Homer1 channels (Figure 3.23.E; 3.23.F), it might have accounted for some regions within unexpanded and expanded cortical tissue slices where a high degree of overlap between PG-5, Bassoon and Homer1 was observed (i.e., Figure 3.22.A, red arrows).
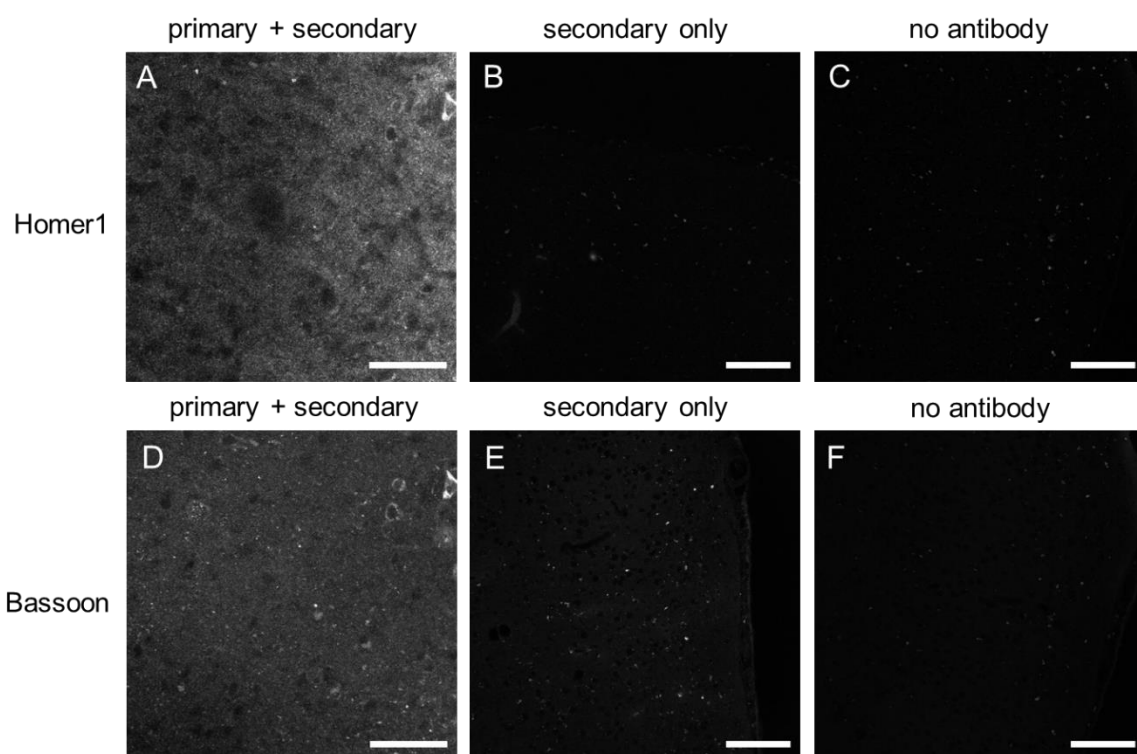
Figure 3.23: Controls for Homer1 and Bassoon immunohistochemistry pre-expansion.
Confocal images of controls for immunohistochemistry of Homer1 and Bassoon synaptic proteins in rTg4510 mouse cortex. rTg4510 mouse tissue was immunolabelled using primary antibodies for (A) Homer1 and (B) Bassoon and were visualised using secondary antibodies.

Figure 3.24: Controls for Homer1 and Bassoon immunohistochemistry post-expansion.
Confocal images of unlabelled, blocked rTg4510 tissue slices expanded using ProExM and imaged using laser settings for (C) Bassoon/Alexa Fluor 555 and (D) Homer1/Alexa Fluor 633. Expanded rTg4510 tissue immunolabelled with (A) Bassoon and (B) Homer1 are shown for comparison. Scale bar: 100 μm.

Immunohistochemistry for (p)tau, Bassoon and Homer1 was also performed on age matched wildtype tissue primarily to compare the specificity of immunolabelling of Bassoon and Homer1 to immunolabelling in transgenic tissue (Figure 3.25). As was the case for Figure 3.8, no (p)tau was detected in wildtype tissue (Figure 3.25.A). Bassoon and Homer1

immunolabelling was extensive throughout the sample (Figure 3.25.B; 3.25.C) in a similar manner to what was observed in immunolabelled unexpanded rTg4510 mouse tissue (Figure 3.17; 3.18). At some areas of the cortex, 'rings' of Bassoon signal was observed around where cell nuclei would be present (Figure 3.25.D; 3.25.E). This Bassoon immunolabelling would overlap with (p)tau aggregation around the nuclei of cells, and could to some extent account for the overlap in signal observed in Figure 3.17.
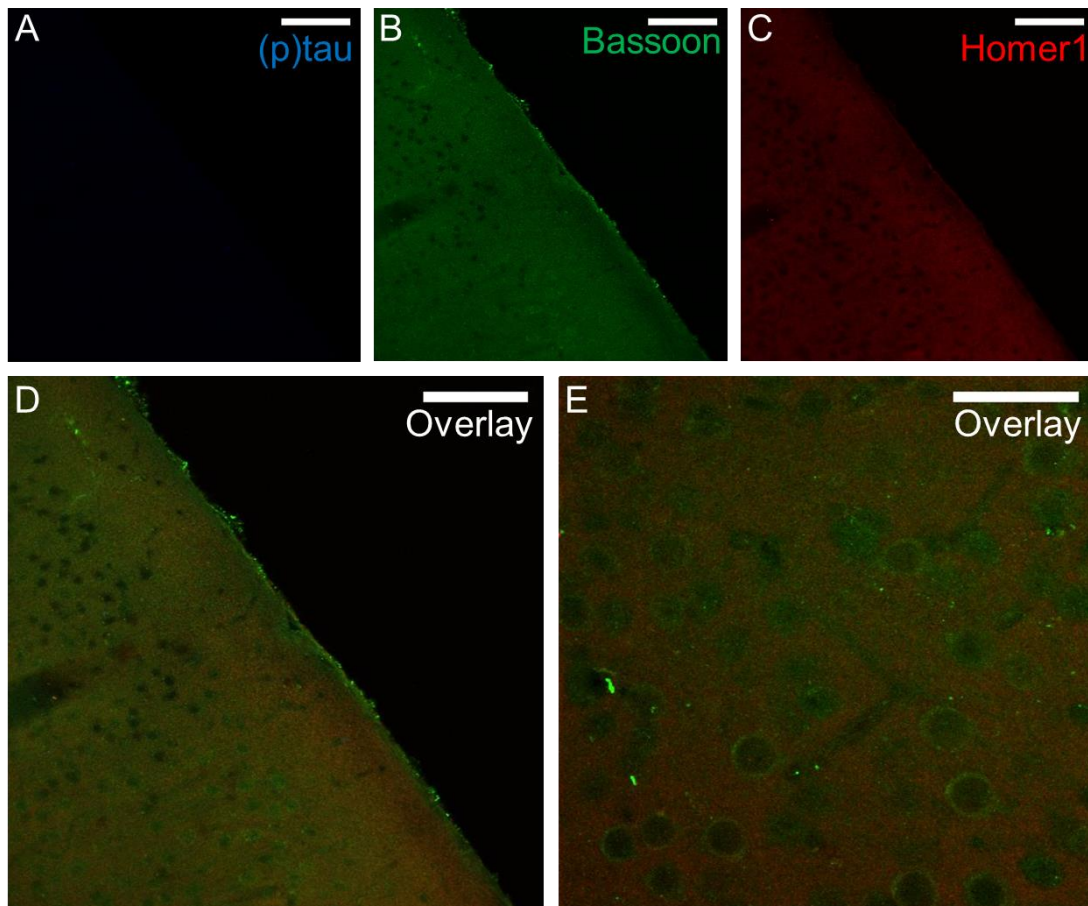
Figure 3.25: PG-5, Bassoon and Homer1 immunolabelling in wildtype age-matched tissue.
Confocal images of wildtype, unexpanded tissue immunolabelled with PG-5 (blue; (p)tau), Bassoon (green) and Homer1 (red). (A-C) show each channel from the same field of view and (D) shows overlay of all three channels. (E) shows overlay of all three channels at a higher magnification. Scale bar for (A-D): 100 µm, (E): 50 µm.

3.3.3. Resolving synaptic markers in young mouse tissue

A secondary series of experiments was set up to address whether synapses identified in Figure 3.22.C-D were similar in appearance to synapses labelled in alternative tissue types where there was less autofluorescence/non-specific fluorescence. If in both tissue types,

putative synapses were morphologically similar, it would support the finding that (p)tau was localised to synapses, as opposed to non-specific fluorescence, in rTg4510 tissue (Figure 3.22.D).

To contrast 4-month old rTg4510 transgenic mice, young P16 mouse tissue was used. Immunohistochemistry for Bassoon and Homer1 was initially performed in unexpanded P16 tissue slices (Figure 3.26). Homer1 immunolabelling in P16 tissue was consistent with what was observed in 4-month old wildtype tissue (Figure 3.26.C; Figure 3.25.C). In contrast, Bassoon immunolabelling seemed a higher density at cell bodies/nuclei compared to extra-somatic areas that would have a higher synaptic density (Figure 3.26.B). Primary and secondary controls for Homer1 and Bassoon immunohistochemistry in this tissue type are shown in Figure 3.29.
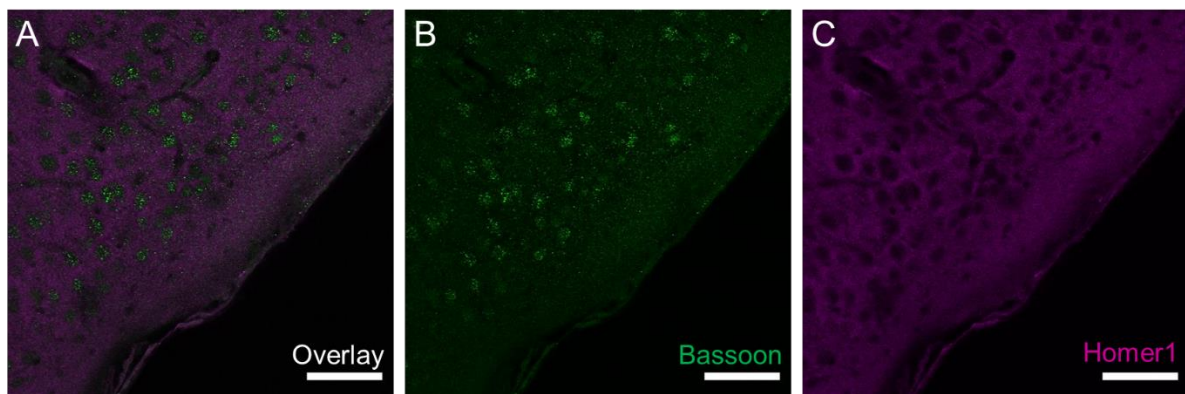
Figure 3.26: Bassoon and Homer1 immunolabelling in young tissue.
Confocal images of unexpanded P16 mouse cortex immunolabelled with (B) Bassoon (green) and (C) Homer1 (magenta). An overlay of both channels is shown in (A). Scale bar: 100 μm.

The findings in Figure 3.26 were explored further by labelling tissue slices with either Bassoon and TO-PRO-3, or Homer1 and TO-PRO-3 (Figure 3.27). This tested the immunoreactivity of primary antibodies in isolation from each other, and the density of synaptic marker immunolabelling in relation to cell nuclei. This confirmed that Homer1 immunolabelling was denser in extra-somatic regions, as expected, and that the converse was true for Bassoon immunohistochemistry (Figure 3.27.A,D).

At this stage it was unclear what was causing increased reactivity of Bassoon at cell bodies/nuclei in P16 non-transgenic tissue, but this was not observed in any trials using 4-month old rTg4510 tissue (Figure 3.17-3.24) or 4-month old wildtype tissue (Figure 3.25).

P16 mouse tissue immunolabelled with Bassoon and Homer1, as in Figure 3.26, was expanded using ProExM to visualise individual synaptic markers and identify co-localised puncta of Homer1 and Bassoon where putative synapses were present (Figure 3.28). Overall, a relatively low proportion of putative synapses were identified (Figure 3.28.B, white arrows) post-expansion, which was surprising however likely explained by the unexpectedly low

density of Bassoon immunolabelling in extra-somatic regions as shown in Figure 3.26 and Figure 3.27. Alternatively, this could have been a result of loss of fluorescence post-expansion.
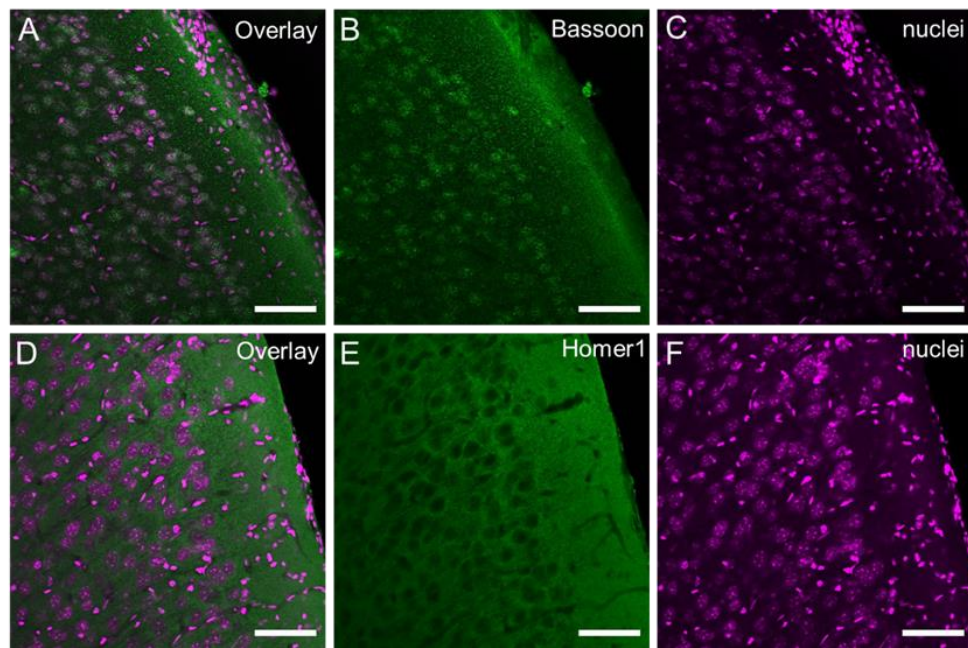
Figure 3.27: Distribution of Homer1 and Bassoon in relation to nuclei in young tissue.
Confocal images of unexpanded P16 mouse cortical tissue labelled with antibodies for Bassoon (A,B, green) or Homer1 (D,E, green) and TO-PRO-3 (magenta). Scale bar: 100 μm.
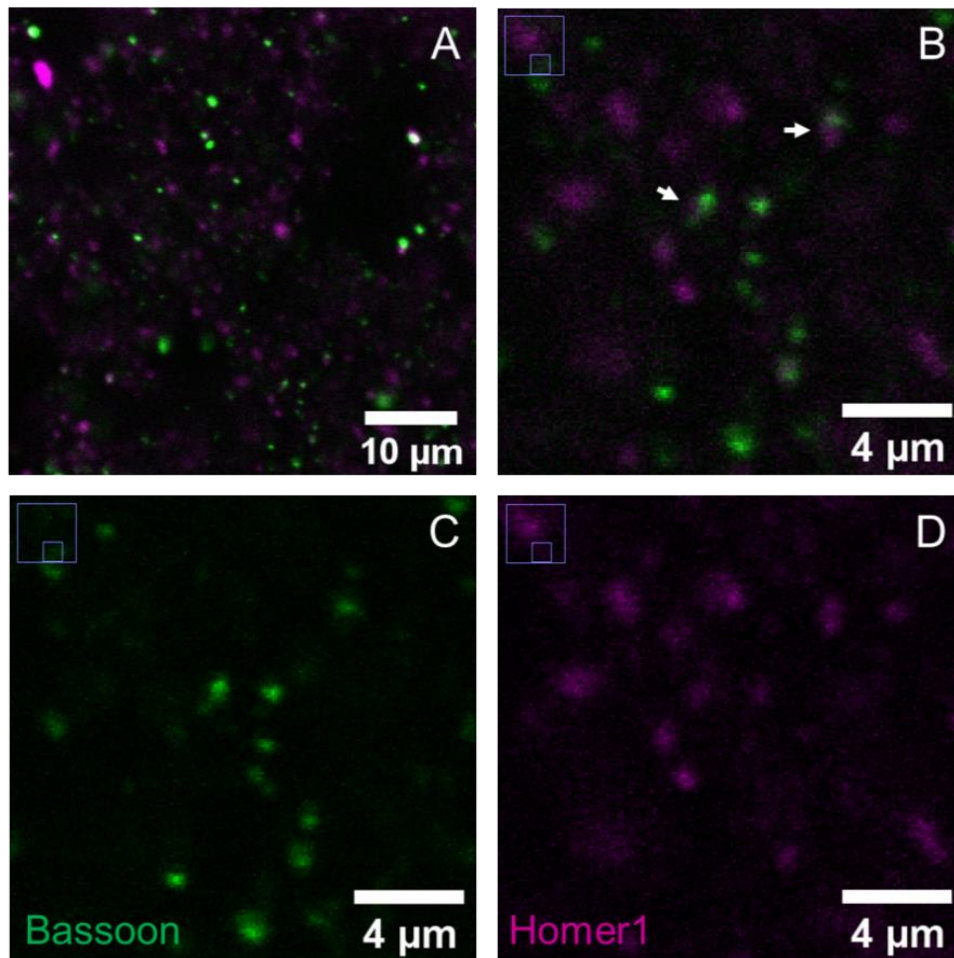
Figure 3.28: Putative synapses in young cortical tissue.
Confocal images of P16 mouse cortical tissue immunolabelled for Bassoon (green) and Homer1 (magenta) and expanded via ProExM. (A) and (B) show overlay of both channels. Arrows indicate putative synapses based on the colocalisation of Bassoon and Homer1. Both channels shown in (B) are displayed separately to show resolution of (C) Bassoon and (D) Homer1. Scale bar: 100 μm.

To test for specificity of Bassoon and Homer1 immunohistochemistry in P16 mouse tissue, primary and secondary controls were established (Figure 3.29). Homer1 immunolabelling was visualised using secondary antibodies conjugated to Alexa Fluor 633 in Figure 3.26; 3.28, and Alexa Fluor 546 in Figure 3.27 (Section 2.2.4), so controls were performed for both conditions. Blood vessels were visable in primary and secondary controls however no tissue autofluorescence resembling Figure 3.23 was observed.
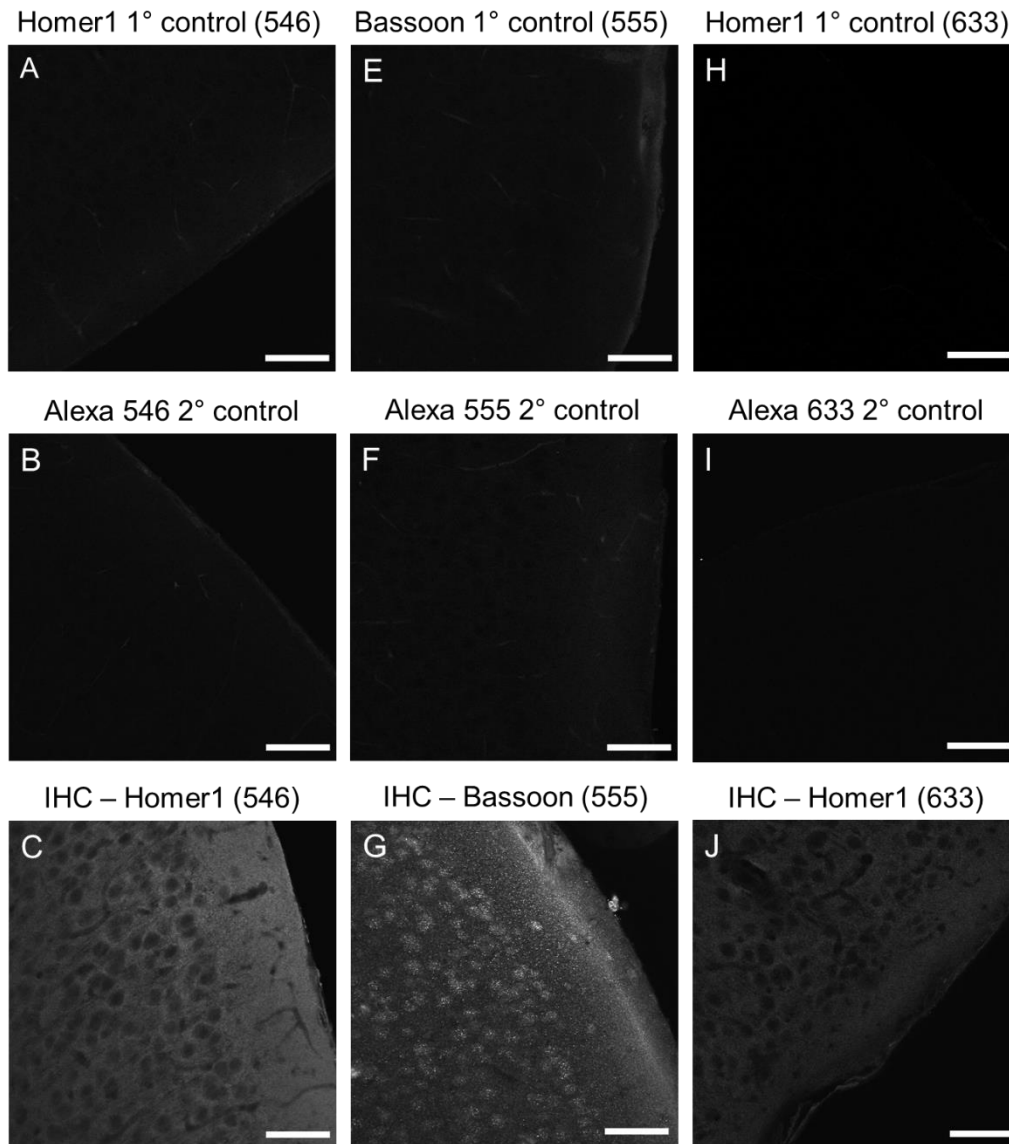
Figure 3.29: Controls for Bassoon and Homer1 immunohistochemistry in young tissue.
Primary and secondary controls for immunohistochemistry (IHC) of Bassoon and Homer1 in unexpanded P16 mouse cortical tissue. (A-C) controls for Homer1 when visualised with Alexa Fluor 546. (E-G) controls for Bassoon. (H-J) controls for Homer1 when visualised with Alexa Fluor 633. (C,G,J) show P16 tissue immunolabelled with Homer1 and Bassoon for comparison. Scale bar: 100 µm.

Overall, the morphology of putative synapses identified in young, non-transgenic expanded tissue slices was similar to what was observed in rTg4510 tissue (Figure 3.22; 3.28). This demonstrates a consistency in immunolabelling of Homer1 and Bassoon co-localised puncta across different tissue types, however overall Bassoon immunohistochemistry was strikingly different in young non-transgenic tissue compared to rTg4510 tissue (Figure 3.17; 3.26.B; 3.27.B). As the labelling of Bassoon was less dense in extra-somatic regions compared to Homer1, the proportion of putative synapses identified in this tissue type was low compared to rTg4510 tissue (Figure 3.21; 3.22; 3.28).

4. Discussion

The aims of this research were to demonstrate that ProExM tissue expansion was a reliable and effective technique to improve resolution for light microscopy. Then, to apply this technique to rTg4510 brain tissue from 4-month-old mice to demonstrate the presence of phosphorylated tau at synapses early in tauopathy neurodegeneration.

The key findings were:

1. ProExM can be used to expand fixed tissue slices ~3.6-4.0 fold, as determined by the post-expansion size increase in Feret diameter of nuclei.
2. Applying ProExM to tissue slices improves the resolution of tau fibrils compared to imaging unexpanded slices with a higher magnification.
3. Moderate tau deposition is present in rTg4510 mice at 4 months of age throughout cortical layers II-V/VI and from PFC to SSC.
4. Phosphorylated tau can be located to synapses using antibodies for synaptic proteins Bassoon and Homer1 in rTg4510 brain tissue from 4-month-old mice, however the reliability of these data is limited by the presence of tissue autofluorescence.

4.1. ProExM tissue expansion is a reliable and effective technique to increase the resolution of ultrastructure

4.1.1. Modifications to the ProExM protocol

The initial series of experiments (Section 3.1.1) aimed to demonstrate that ProExM could expand tissue slices within a range of 4.0-4.5 fold and that the expansion of tissue was linear, which have both previously been shown (Tillberg et al, 2016).

Although modifications needed to be made to successfully image tissue slices after they were expanded via ProExM (Table 3.1), tissue slices were successfully expanded in the very first run of the Asano et al, 2018 ProExM protocol trialled in this study (Asano et al, 2018). This demonstrates that ProExM can be employed relatively easily and quickly compared to other super-resolution light microscopy techniques that require extensive time or training to establish.

Some key changes that were made to optimise ProExM is this study were:

1. To design 3D-printed, plastic, reusable gelling chambers instead of constructing gelling chambers out of glass coverslips
2. To reduce the time for monomer perfusion through the tissue sample from 30 minutes to 20 minutes and to agitate the microcentrifuge tube regularly (~5-10 minutes)

3. Keep the digestion time, when the gel-tissue sample is left overnight in Proteinase K, consistent (i.e., ~16 hours)

Gelling chambers assembled from glass coverslips were effective but also fragile. This was because the water tension that adhered glass slides to coverslips could be easily broken when pipetting gelling solution into chambers. After switching to plastic gelling chambers adhered to glass slides using silicon grease, this issue was resolved. Comparably, a recently published ProExM protocol used laser-cut adhesive-backed silicone sheet as an alternative to glass coverslip gelling chambers (Tillberg, 2021). This protocol also specified a monomer perfusion time for fixed tissue slices of 20 minutes as long as tissue thickness was ≤300 μm, and in this study 100 μm thick tissue slices were used. (Tillberg, 2021).

Recent studies have shown that expansion factor, measured as the ratio of cell soma area before and after expansion, increased with the longer durations of proteinase K digestion (digestion time) (Campbell et al, 2020). In addition, increasing digestion time from 8 to 16 hours resulted in a significant decrease in fluorescence intensity of GFP+ neurons (Campbell et al, 2020). As a result of these findings, digestion time was restricted to 16 hours in results shown in 3.1.2 onwards.

In future studies, if fluorescence loss became a limiting factor for confocal imaging of expanded slices, digestion time could be reduced to 8hrs≤x<16hrs, which would reduce the size of the expansion factor but prevent a significant decrease in fluorescence intensity.

4.1.2. Immunolabelling of tissue prior to expansion

Protocols for expansion microscopy have typically implemented pre-expansion immunolabelling as this follows the existing workflow for antibody staining (Chen et al, 2015; Tillberg et al, 2016; Gao et al, 2017). This allows previously immunolabelled tissue samples to be subsequently expanded for direct pre- and post-expansion comparison which is required for measuring sample distortion (Tillberg et al, 2016). However, pre-expansion immunolabelling does result in a substantial loss of florescence (Figure 1.7.B).

Protocols of expansion microscopy have also been established in which the digestion and expansion of tissue occurs before immunolabelling. This reduces the florescence loss observed when immunolabelling pre-expansion, however during the mechanical homogenization of tissue epitopes can be degraded (Gao et al, 2017). Ku et al, 2016 showed immunolabelling of tissue post-expansion was compatible with just 82% of the antibodies tested as a result of epitope loss (Ku et al, 2016). For this reason, and because of the difficulty in handling expanded hydrogels, a pre-expansion immunolabelling protocol was implemented.

4.1.3. Micro expansion factor range was ~3.6-4.0 fold

In this study, expansion factors were calculated as the ratio of mean nuclei Feret diameter in expanded tissue slice compared to mean nuclei Feret diameter from all unexpanded slices. Cell nuclei were selected for measurement as nuclear staining was performed in the majority of expanded tissue slices. Also, cell nuclei have a roughly spherical morphology, therefore the circularity of nuclei could be measured and any changes in circularity could be indicative of a non-linear expansion.

From these measurements, expansion factors were calculated between ~3.6-4.0x. This is ~0.5 fold less than the range of 4.0-4.5 fold reported in early ProExM papers (Chen et al, 2015: Tillberg et al, 2016). However, these papers determined expansion factor based on the degree of expansion of the hydrogel (macro expansion factor) measured by comparing low magnification epifluorescence images of whole tissue sections before and after expansion. Subsequent research has demonstrated that macro expansion factor was consistently larger than micro expansion factor measured by comparing cell soma area using the formula: linear expansion factor $= \frac{\sqrt{cell\ area}}{\sqrt{avg\ non.expanded\ cell\ area}}$ (Campbell et al, 2020). This likely explains the discrepancy between micro expansion factor size measured in this study to previously reported expansion factors, and also highlights that the two forms of quantification should be clearly distinguished from one another in future studies.

Differences in micro and macro expansion factor have also been observed when using nuclear pore measurements as microscopic reporters of expansion (Pesce et al, 2019; Büttner et al, 2021). It has also been observed that different organelles within one cell can expand differently (Büttner et al, 2021) and that expansion of organelles varies depending on tissue type (Pernal et al, 2020). In the future, this issue could be mitigated by imaging the same tissue or cells before and after expansion.

4.1.4. Using changes in circularity as a measurement of linearity of expansion

Results from 3 runs of ProExM tissue expansion summarised in Figure 3.3.C indicate that there was a small but significant increase in circularity in expanded nuclei compared to unexpanded nuclei. This could reflect the improved resolution of nuclei in expanded tissue in comparison with 100 µm free floating slices imaged using widefield microscopy (Figure 3.1).

Contrary to this, Figure 3.6.C showed a significant reduction in circularity in expanded tissue when imaged using confocal microscopy. Whilst it is not possible to rule out non-linear expansion based on the difference in circularity in Figure 3.6.C, many previous studies have confirmed that if the embedded tissue is sufficiently digested, there is nanoscale isotropy of expansion (Chen et al, 2015; Tillberg et al, 2016; Gambarotto et al, 2019).

It would seem more likely that a reduction in circularity post-expansion is not based on the chemistry of ExM but on biological variation of nuclei within the expanded tissue samples.

Firstly, data in Figure 3.6 are limited by a small sample size of nuclei; it is clear from Figure 3.9 that the morphology of nuclei varied from cell to cell within the sample. These data also do not account for differences in nuclei size/circularity between different cell types i.e., neurons vs glia. In future studies, calculating the circularity of smaller spherical structures such as nucleoli could limit variation within groups (expanded and unexpanded), but it would also be necessary to increase the sample size to ≥30 to improve the measurement of the distribution of datapoints, or to image the same structures (i.e., nuclei) before and after expansion.

4.1.5. ProExM tissue expansion increases resolution of tau fibrils compared to unexpanded tissue

It was observed qualitatively that confocal images of tau aggregation in expanded tissue slices were less blurry than from unexpanded slices, and hence the expansion improved resolution of (p)tau aggregation (Figure 3.13). When this was tested quantitively, it was confirmed that ProExM tissue expansion resulted in increased detection of narrower and more numerous fluorescence peaks, therefore applying ProExM increases the resolving power of tau fibrils (Figure 3.14; 3.15). A similar technique has been used to demonstrate that a 4x expansion of cultured cells improves the resolution of individual actin filaments that were otherwise too densely packed to resolve individually (Figure 1.8) (Park et al, 2020).

The width of peaks in Figure 3.15.B was measured in pixels as this was standardised for both conditions (image size: 512*512), and the primary aim was to accurately demonstrate improved resolution post-expansion. It was hypothesised that width in pixels could be converted to μm and compared with the actual size of tau filaments measured using EM (Crowther, 1991; Sadqi et al, 2002; Morozova et al, 2013). This would test whether the resolving power of ProExM tissue expansion was enough to accurately measure tau fibrils. However, this analysis would have required adjusting the peak widths measured in the expanded condition by the expansion factor. This could have been problematic as expansion factor was based on nuclei measurements, and as discussed in 4.1.3., subcellular features can expand differentially within the same cell (Büttner et al, 2021).

A limitation of the analysis in Figure 3.14 and Figure 3.15 is that factors other than increased resolving power post-expansion could explain the difference between unexpanded and expanded groups, such as the extent or density of tau aggregation in each image. In addition, the size of the expansion factor varies per slice. To improve this analysis, regions of tau aggregation should be imaged before and after expansion within the same slice, as in Figure 1.8. In doing so, the same molecular structures can be compared, allowing pairwise comparisons and reduced unaccounted variance in the data.

4.2. (p)tau localised to synapses in 4-month-old rTg4510 mouse tissue but findings limited by resolution and non-specific fluorescence

4.2.1. Moderate (p)tau deposition at 4 months in rTg4510 mouse brain tissue compared to wildtype littermates

PG-5 immunohistochemistry in rTg4510 tissue from 4-month-old mice showed moderate (p)tau deposition throughout the cortex which was not observed in age-matched wildtype littermates (Figure 3.7; 3.11). There was variability in the extent of (p)tau from cell to cell within expanded slices as expected, but all mice used in this study showed significant (p)tau across the cortical regions studied, from PFC to SSC, and from cortical layers II-V/VI. Similar observations were found using MC-1 and PHF-1 (Figure 3.12).

The results in Figure 3.7 were consistent with previous findings showing PG-5+ labelling of pre-tangles in the cortex of rTg4510 as early as 2.5 months of age, and this immunolabelling is moderate by 4-5 months (Ramsden et al, 2005;Santa-Cruz et al, 2005). This correlates with the development of cognitive impairments in rTg4510 at ~4 months of age. (Ramsden et al, 2005; Blackmore et al, 2017).

4.2.2. Assessing the evidence that (p)tau is present at synapses in rTg4510 mouse tissue

rTg4510 mouse tissue immunolabelled for Bassoon, Homer1 and PG-5 and expanded using ProExM allowed (p)tau to be identified in close proximity to putative synapses, marked by co-localisation of Bassoon and Homer1 (Figure 3.22). This was not possible to observe in unexpanded tissue due to the limited resolution and high density of synaptic marker labelling.

However, this evidence is limited, primarily due to technical difficulties that arose when imaging these triple-labelled expanded slices. Firstly, the signal from Bassoon and Homer1 was relatively dim post-expansion. Therefore, when imaging the expanded tissue sample, fluorescence was prone to bleaching due to the high laser excitation required. Secondly, despite ProExM tissue expansion, the resolution of synaptic marker pairings was still limited to ~70 nm. For comparison, the size of the synaptic cleft is approximately 20-40 nm, and would not therefore be resolvable after tissue expansion.

Recent variants of Expansion Microscopy have overcome this by designing protocols that have increased expansion factors up to 20 fold (Chang et al, 20f17; Truckenbrodt et al, 2018; Damstra et al, 2021) (Table 1.1). Iterative expansion microscopy, or iExM, describes a tissue expansion twice in series, in which a second polyacrylamide gel is formed in the newly opened space from the first expansion and expanded (Chang et al, 2017). In doing so, the final expansion factor is the product of each expansion i.e. (4.5*4.5 = 20.25x macroscopic

expansion factor). This would reach a resolution limit as low of 20 nm, at which point the synaptic cleft of synapses is resolvable (Figure 4.1.(i))(Chang et al, 2017).

Iterative expansion microscopy is more technically difficult to implement than ProExM as it requires custom oligonucleotide probes conjugated to fluorophores for visualisation of ultrastructure, as described in the original Expansion Microscopy protocol (Chen et al, 2015). An alternative expansion microscopy technique that is still compatible with conventional antibodies and fluorescence proteins is x10 expansion microscopy (X10) (Truckenbrodt et al, 2018; 2019). In X10 microscopy, an improved superabsorbent hydrogel recipe is used that results in a ten-fold expansion whilst retaining native proteins in the sample (Truckenbrodt et al, 2018). This results in a ~30 nm resolution limit, allowing improved resolution of synapses compared to a 4x expansion using ProExM (Figure 4.1, bottom panel) (Truckenbrodt et al, 2018).

Updated protocols continue to be published to reduce the technical limitations of preceding protocols whilst retaining a ten-fold expansion of tissue. For example, tenfold expansion microscopy, or TREx, addresses the limitations of x10 microscopy by designing a gel that has improved mechanical integrity and can be applied to thick tissue slices (Damstra et al 2021). In future studies, a protocol of expansion microscopy that produces a larger expansion of tissue than ProExM whilst remaining compatible with conventional antibodies, such as X10 or TREx, could be applied to improve the ability to resolve (p)tau at synapses.

Original data; adapted from Figure 3.26
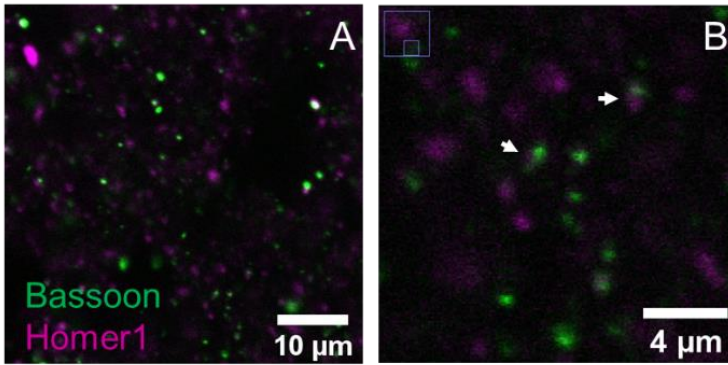
iExM. Adapted from Chang et al, 2017
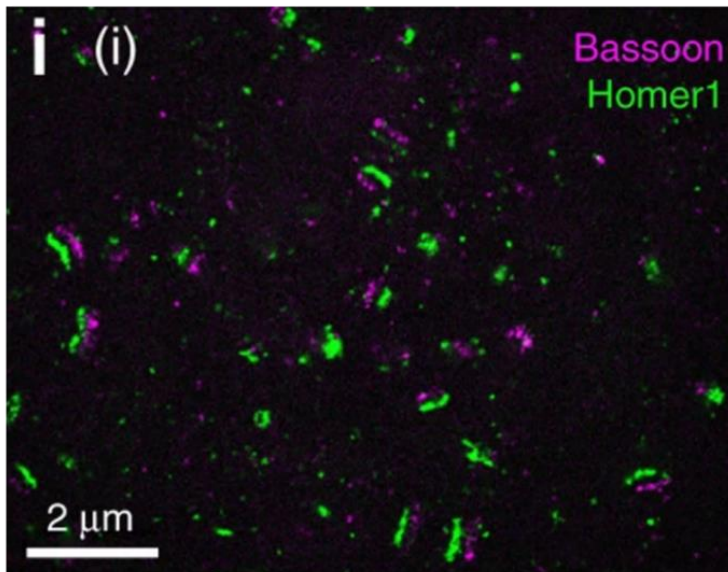
X10 ExM. Adapted from Trunckenbrodt et al, 2018
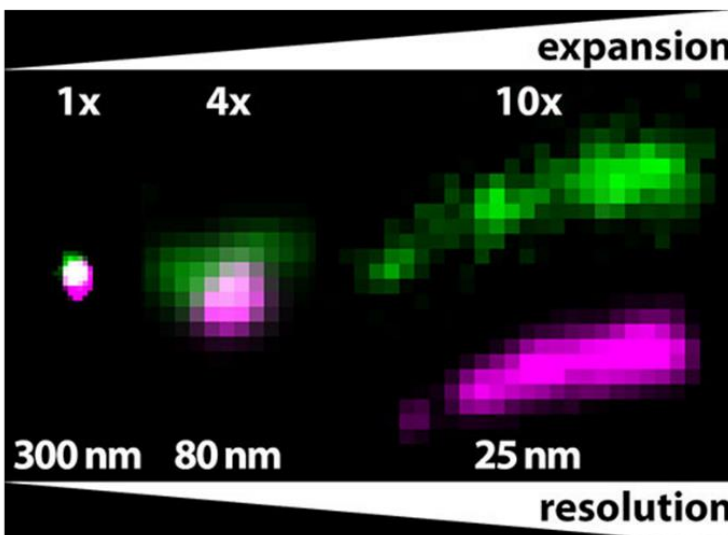
Figure 4.1: Resolution of putative synapses using different ExM methods. *Comparing the resolution of synaptic markers Bassoon and Homer1 using ProExM (top panel, original data), iterative expansion microscopy (middle panel, adapted from Chang et al, 2017) and x10 expansion microscopy (bottom panel, adapted from Truckenbrodt et al, 2018).*

(Top panel): Confocal images of P16 mouse cortical tissue immunolabelled for Bassoon (green) and Homer1 (magenta) and expanded via ProExM. See Figure 3.28.

(Middle panel): Confocal X-Y image primary somatosensory cortex of P56 coronal mouse brain slice after labelling with anti-Bassoon (magenta) and anti-Homer1 (green) and 16-fold expansion via iExM. (Adapted from Chang et al, 2017).

(Bottom panel): Multi-colour imaging of Homer1 (magenta) and Bassoon (green) immunolabelling in cultured rat hippocampal neurons with no expansion (left), x4 expansion via ProExM (middle), and 11x expansion via x10 ExM (right). (Adapted from Truckenbrodt et al, 2018).

4.2.3. Non-specific fluorescence observed in rTg4510 tissue immunolabelled for Bassoon, Homer1 and (p)tau.

Overall, the results in 3.3 show that in expanded 4-month-old rTg4510 mouse cortical tissue (p)tau can be resolved at putative synapses identified by the colocalisation of Homer1 and Bassoon. However, several limitations of immunohistochemistry of Bassoon and Homer1 were identified in this series of experiments. Initially, a very high degree of overlap was detected for synaptic markers to areas of (p)tau immunolabelling. This could be a result of increased density of synaptic marker labelling as suggested by Figure 3.18; 3.19, however later experiments in non-transgenic age matched tissue identified 'ring-shaped' Bassoon immunolabelling around nuclei/cell bodies which would also likely contribute (Figure 3.25.E).

Autofluorescence was also observed throughout rTg4510 tissue (Figure 3.23) however this was not seen in tissue from rTg4510 littermates in earlier experiments (Figure 3.10). This autofluorescence was long ranging, visible in both channels using emission filter ranges for Bassoon and Homer1, and also tissue samples post-expansion (Figure 3.24.C-D). It is possible that this autofluorescence was caused by the presence of lipofuscin, an autofluorescent lipopigment formed by lipids, metals and misfolded proteins which accumulates in neurons during normal aging and neurodegenerative diseases (Moreno-García et al, 2018). The emission spectra of lipofuscin in rat brain tissue ranges from 400 nm-700 nm, with the emission maximum at 540-570 nm (Mochizuki et al, 1995). In Figure 3.22.A, red arrows denote regions of dense, long-ranging fluorescent signal that would fit this profile for lipofuscin.

Considering this evidence in totality, it is difficult to conclude that fluorescent signal detected for Homer1 and Bassoon in Figures 3.17-3.25 was specifically identifying synapses. Immunohistochemistry for Bassoon and Homer1 was also tested on young (P16), healthy mouse tissue to see if the morphology of synapses identified by Bassoon and Homer1 coupling was similar. In this instance, there was no autofluorescence detectable in the tissue (other than from blood remaining in capillaries due to drop fixation), supporting the hypothesis that autofluorescence in rTg4510 mouse tissue could have been due to neurodegeneration/lipofuscin aggregation. In this young mouse tissue, Homer1 immunolabelling looked consistent to what was observed in rTg4510 mouse tissue, but as discussed in 4.2.2, resolution of synapses was limited even after ProExM tissue expansion.

Surprisingly, a different issue with Bassoon immunohistochemistry was observed in P16 tissue. There was a higher density of Bassoon labelling colocalising with the nucleus and the cell body than in the extra-somatic space which would have a higher synaptic density (Figure 3.26; 3.27).

It has been shown in rat hippocampal neuronal cultures that Bassoon and Piccolo (another large presynaptic scaffolding protein) colocalise at the golgi complex and that this is required for transport out of the soma and synaptic targeting (Dresbach et al, 2006; Zhai et al, 2001). Therefore, during bulk synaptogenesis in neurodevelopment, Bassoon and other presynaptic

scaffolding proteins may be located and assemble at the golgi complex, explaining the observations in Figure 3.27. However, it is also possible that the observation in Figure 3.27 is due to non-specific immunoreactivity, and this could only be conclusively ruled out by repeating this experiment using a Bassoon knockout mouse.

4.3. Limitations, future work, and conclusions

4.3.1. Advantages and limitations of ProExM

ProExM has been shown to be a relatively easy, quick method to achieving resolution up to ~60 nm in fixed tissue slices. In this study, the micro expansion factor of tissue slices consistently fell in a range of 3.6-4.0x. It is clear from images comparing unexpanded and expanded brain tissue slices that ExM improves resolution of fluorescently labelled structures and reduces background signal (i.e. Figure 3.7). It was also demonstrated quantitively that the resolution of tau fibrils in expanded tissue was improved post-expansion.

Other methods of super-resolution light microscopy (SRLM) can achieve greater resolution, down to limits of ~20-30 nm, such as STED (Hell & Wichmann, 1994) and PALM/STORM microscopy (Betzig et al, 2006; Hess et al, 2006; Rust et al, 2006). However, these SRLM techniques have disadvantages, for example, they require fluorophores that can withstand high laser intensities (STED) or light exposure for several thousand frames in rapid succession (PALM/STORM) (Truckenbrodt & Rizzoli, 2021). Since the increased resolution with ProExM is a result of increasing the size of the physical tissue sample rather than optics, ProExM can and has been combined with optical super resolution techniques including STED (Gao et al, 2018), Structured illumination microscopy (SIM) (Halpern et al., 2017), PALM (Tillberg et al, 2016) and STORM (Xu et al, 2019).

There are also disadvantages of ProExM to consider when selecting suitable SRLM techniques. Firstly, ProExM can be applied to fixed tissue or cultured cells only (Chen et al, 2015; Tillberg et al, 2016). There is also ~50% loss of fluorescence post-expansion as a result of less fluorophores per unit volume of tissue or cultured cells, or due to over-digestion of the sample with Proteinase K (Figure 1.7.B) (Tillberg et al, 2016; Klimas et al, 2019).

This discounts fluorophores that are incompatible with ProExM as loss of fluorescence post-expansion is too extensive. For example, Cyanine family dyes and Alexa Fluor 647 are degraded during the polymerisation step of ExM (Gaudreau-Lapierre et al, 2021), as well as iRFP which is degraded during Proteinase K digestion (Tillberg et al, 2016). This issue can be easy to circumvent however as many alternative dyes/fluorophore probes are available.

Finally, imaging expanded tissue samples can be limited by working distance due to the increased thickness of the gel post-expansion. This is particularly the case when combining tissue expansion with SRLM optical techniques such as STED and PALM/STORM, in which case only expanded cells are compatible due to the short working distance objectives used

with these microscopy techniques (Gallagher et al, 2021). Expanded tissue slices can be imaged using SIM however (Halpern et al, 2017).

4.3.2. Limitations of the rTg4510 mouse model

Rodent models are used to mimic one or several aspects of disease, such as protein aggregation or behavioural impairments associated with a specific gene mutation. Whilst these models are not equivalent to the progression of human disease, they provide great insight, often allowing causal relationships to be demonstrated between cellular features (i.e., pathological protein occlusions) and their functional consequences. However, many aspects of disease can be lost when modelled in animals, and disruption of a gene/s may not produce the expected result due to developmental compensation and plasticity (Dawson et al, 2018).

The rTg4510 model phenotypically resembles human tauopathies, including the pathological aggregation of tau into NFTs, cognitive impairments and age-related neuronal loss (Ramsden et al, 2005; Blackmore et al, 2017). It has been demonstrated that suppression of tauP301L gene by doxycycline halts neuronal loss and allows for the recovery of memory function (SantaCruz et al, 2005; Spires et al, 2006), which has been used as evidence of a causal relationship between tauP301L overexpression and the tauopathy phenotype of rTg4510 mice.

However, it has since been shown that tauP301L overexpression is not sufficient alone to drive the early tau pathology observed in rTg4510 mice (Gamache et al, 2019). It was found that a targeted insertion of tauP301L (rT2/T2 mice) did not have the significant forebrain atrophy observed in the rTg4510 mouse model (as seen in Figure 1.4), despite rT2/T2 mice having higher overall P301L forebrain expression than transgenic rTg4510 mice (Gamache et al, 2019). This shows that the overexpression of human tauP301L alone is not sufficient to drive full rTg4510 pathology.

In addition, whole genome sequence analysis identified that tauP301L insertion in rTg4510 mice disrupted fibroblast growth factor 14 (Fgf14) expression (Gamache et al, 2019). Finally, it was shown that the tTA Tg-INDEL allele, which drives tauP301L expression in both rTg4510 and rT2/T2 mice, is approximately a 7-copy tTA-trans gene insertion in a ~500 kb deletion that disrupts five other genes and results in accelerated tau pathology compared to T2 hemizygous mice (Gamache et al, 2019).

These findings do not negate hypotheses that have previously or are still being drawn from experiments utilising the rTg4510 mouse line. However, confounding factors that result in accelerated tauopathy should be considered. With regards to the experiments conducted in this thesis, tau protein has been identified at human synapses in patients with AD (Tai et al, 2012). In addition, synapse disfunction and loss is a strong correlate of cognitive decline in AD. Therefore, studying the mislocation of tau to synapses in animal models could have interesting implications for early-stage cognitive decline in AD and other tauopathies.

However, the mechanism for mutant tau mislocation in rTg4510 mice may differ to that of endogenous tau in human tauopathies. Also, if in an extended study, a correlation between the functional properties of cells to the synaptic tau load, or the size of synapses to synaptic tau load in rTg4510 mice were to be made, it would be necessary to account for the confounding disruption of Fgf14 and other genes. In this instance, it would seem appropriate to compare to an alternative mouse model of tauopathy.

4.3.3. Future work

In this study, ProExM was limited in resolving the association between Bassoon and Homer1. There were also multiple issues identified with immunolabelling Homer1 and Bassoon in both transgenic and wildtype tissue. As an alternative to immunohistochemistry for synaptic markers, dendrites and dendritic spines could be visualised for the localisation of (p)tau to the post-synapse, as performed in Kopeikina et al, 2013 (Figure 1.5.A-C).

This could be achieved by filling cells with biocytin during whole cell patch clamp electrophysiological recordings which would have the advantage of obtaining electrophysiological data from rTg4510 cortical cells, but would be time consuming and relatively low yield. Alternatively, a sparce viral injection of fluorescence protein (i.e. GFP, YFP) could be used to visualise neurons and their processes. GFP and YFP have been shown to be compatible with expansion microscopy (Tillberg et al, 2016; Wassie et al, 2018).

This experimental design could also utilise alternative expansion microscopy protocols with a higher expansion factor, such as x10 microscopy or TREx. By improving resolving power, down to 20-30 nm, more detailed anatomical measurements of the association of (p)tau to synapses could be made. For example, measurements could be made as to whether:

(1) Cells with significant NFT deposition at the soma have a higher incidence of (p)tau at dendrites.
(2) The size of dendritic spines, an indirect measure of synaptic strength, is related to the proximity of nearby (p)tau.
(3) The spine density of a given length of dendrite is inversely proportional to the amount of nearby tau aggregation and/or synaptic tau presence.

This study could also be carried out across a wider age range, i.e., from 2.5 months to 8-10 months, depending on the mouse model selected. This would provide some insight into how the association of (p)tau at dendritic spines progresses over time, and the impact this has on dendritic spine morphology.

4.3.4. Conclusions

In conclusion, ProExM tissue expansion is a reproducible and effective method to increase resolving power of ultrastructural detail in fixed immunolabelled tissue slices. However, protocols need to be optimised, and the size of expansion should be calculated for specific organelles which may expand differentially from one another. Some recommendations have been made in 4.1.1 which improve the ease of handling and imaging of ExM gels, but if new protocols with higher expansion factors are to be tested in the future, these will need to be independently troubleshooted.

By implementing ProExM tissue expansion to increase the resolving power of tau fibrils and synaptic markers, (p)tau was located to some putative synapses in 4 month old rTg4510 mice. However, there were limitations in immunohistochemistry, including the presence of tissue autofluorescence. In the future, using labelled neurons and identifying (p)tau associated with dendritic spines would allow a more quantitative approach to be taken (Section 4.3.3).

Tau has been shown at pre- and post-synapses in human AD brain tissue. Therefore, further studying intracellular tau distribution in mouse tauopathy models may provide significant insight into how early (p)tau isoforms are mislocated to synapses, and whether its location impacts dendritic spines or dendrites morphologically. This could have a downstream impact on a cells' ability to receive and integrate afferent signal, potentially contributing to synapse and neuron loss that occurs in tauopathy-driven neurodegeneration.

5. References

Agrawal, M., & Biswas, A. (2015). Molecular diagnostics of neurodegenerative disorders. *Frontiers in molecular biosciences* 2, 54.

Aizenstein, H.J., Nebes, R.D., Saxton, J.A., Price, J.C., Mathis, C.A., Tsopelas, N.D., Ziolko, S.K., James, J.A., Snitz, B.E., Houck, P.R., Bi, W., Cohen, A.D., Lopresti, B.J., DeKosky, S.T., Halligan, E.M., Klunk, W.E. (2008). Frequent amyloid deposition without significant cognitive impairment among the elderly. *Arch Neurol.* 65(11), 1509-17.

Alonso, A.C., Zaidi, T., Grundke-Iqbal, I., Iqbal, K. (1994). Role of abnormally phosphorylated tau in the breakdown of microtubules in Alzheimer disease. *Proc Natl Acad Sci U S A.* 91(12), 5562-6.

Alzforum. (2019). Research Models: rTg(tauP301L)4510. Retrieved from https://www.alzforum.org/research-models/rtgtaup301l4510.

Alzheimer, A. (1906). Über einen eigenartigen schweren Erkrankungsprozeβ der Hirnrincle. *Neurol Central.* 25, 1134.

Alzheimer's society. (2020). How much does dementia care cost? Retrieved from https://www.alzheimers.org.uk/blog/how-much-does-dementia-care-cost.

Arendt, T., Stieler, J.T., Holzer, M. (2016). Tau and tauopathies. *Brain Research Bulletin*, 126(Pt 3), 238-292.

Arriagada, P.V., Growdon, J.H., Hedley-Whyte, E.T., Hyman, B.T. (1992). Neurofibrillary tangles but not senile plaques parallel duration and severity of Alzheimer's disease. *Neurology* 42(3 Pt 1), 631-9.

Bancher, C., Grundke-Iqbal, I., Iqbal, K., Fried, V.A., Smith, H.T., Wisniewski, H.M. (1991). Abnormal phosphorylation of tau precedes ubiquitination in neurofibrillary pathology of Alzheimer disease. *Brain Res.* 539(1), 11-8.

Barbier, P., Zejneli, O., Martinho, M., Lasorsa, A., Belle, V., Smet-Nocca, C., Tsvetkov, P.O., Devred, F., Landrieu, I. (2019). Role of Tau as a Microtubule-Associated Protein: Structural and Functional Aspects. *Front Aging Neurosci.* 11, 204.

Betzig, E., Patterson, G. H., Sougrat, R., Lindwasser, O. W., Olenych, S., Bonifacino, J. S., Davidson, M. W., Lippincott-Schwartz, J., & Hess, H. F. (2006). Imaging intracellular fluorescent proteins at nanometer resolution. *Science*, *313*(5793), 1642–1645.

Bierer, L. M., Hof, P. R., Purohit, D. P., Carlin, L., Schmeidler, J., Davis, K. L., & Perl, D. P. (1995). Neocortical neurofibrillary tangles correlate with dementia severity in Alzheimer's disease. Archives of neurology, 52(1), 81–88.

Binder, L.I., Frankfurter, A., Rebhun, L.I. (1985). The distribution of tau in the mammalian central nervous system. *J Cell Biol.* 101(4), 1371-8.

Black, M.M., Slaughter, T., Moshiach, S., Obrocka, M., Fischer, I. (1996). Tau is enriched on dynamic microtubules in the distal region of growing axons. *J Neurosci.* 16(11), 3601-19.

Blackmore, T., Meftah, S., Murray, T.K. et al. (2017) Tracking progressive pathological and functional decline in the rTg4510 mouse model of tauopathy. *Alz Res Therapy* 9, 77.

Brunello, C.A., Merezhko, M., Uronen, RL. et al. (2020). Mechanisms of secretion and spreading of pathological tau protein. *Cell. Mol. Life Sci.* 77, 1721–1744.

Büttner, M., Lagerholm, C. B., Waithe, D., Galiani, S., Schliebs, W., Erdmann, R., Eggeling, C., & Reglinski, K. (2021). Challenges of Using Expansion Microscopy for Super-resolved Imaging of Cellular Organelles. *Chembiochem : a European journal of chemical biology*, 22(4), 686–693.

Calafate, S., Buist, A., Miskiewicz, K., Vijayan, V., Daneels, G., de Strooper, B., de Wit, J., Verstreken, P., & Moechars, D. (2015). Synaptic Contacts Enhance Cell-to-Cell Tau Pathology Propagation. *Cell reports*, *11*(8), 1176–1183.

Chang, JB., Chen, F., Yoon, YG. et al. (2017). Iterative expansion microscopy. *Nat Methods* 14, 593–599.

Chen, F., Tillberg, P.W., Boyden, E.S. (2015). Optical imaging. Expansion microscopy. *Science.* 347(6221), 543-8.

Collingridge, G., Peineau, S., Howland, J. et al. (2010). Long-term depression in the CNS. *Nat Rev Neurosci* 11, 459–473.

Crimins, J.L., Rocher, A.B., & Luebke, J.I. (2012). Electrophysiological changes precede morphological changes to frontal cortical pyramidal neurons in the rTg4510 mouse model of progressive tauopathy. *Acta neuropathologica* 24(6), 777–795.

Crimins, J.L., Rocher, A.B., Peters, A., Shultz, P., Lewis, J., Luebke, J.I. (2011). Homeostatic responses by surviving cortical pyramidal cells in neurodegenerative tauopathy. *Acta Neuropathol.* 122(5), 551-64.

Crowther R. A. (1991). Straight and paired helical filaments in Alzheimer disease have a common structural unit. *Proceedings of the National Academy of Sciences of the United States of America*, *88*(6), 2288–2292.

Damstra, H., Mohar, B., Eddison, M., Akhmanova, A., Kapitein, L.C., Tillberg, P.W. (2021). Visualizing cellular and tissue ultrastructure using Ten-fold Robust Expansion Microscopy (TREx). *bioRxiv* 428837.

Dawson, T.M., Golde, T.E. & Lagier-Tourenne, C. (2018). Animal models of neurodegenerative diseases. *Nat Neurosci* 21, 1370–1379.

Delaère, P., Duyckaerts, C., Masters, C., Beyreuther, K., Piette, F., Hauw, J.J. (1990). Large amounts of neocortical beta A4 deposits without neuritic plaques nor tangles in a psychometrically assessed, non-demented person. *Neurosci Lett* 116(1-2), 87-93.

DeTure, M.A., Dickson, D.W. (2019). The neuropathological diagnosis of Alzheimer's disease. *Mol Neurodegeneration.* 14, 32.

Ding, H., Matthews, T.A., Johnson, G.V. (2006). Site-specific phosphorylation and caspase cleavage differentially impact tau-microtubule interactions and tau aggregation. *J Biol Chem.* 281(28), 19107-14.

Dresbach, T., Torres, V., Wittenmayer, N., Altrock, W. D., Zamorano, P., Zuschratter, W., Nawrotzki, R., Ziv, N. E., Garner, C. C., & Gundelfinger, E. D. (2006). Assembly of active zone precursor vesicles: obligatory trafficking of presynaptic cytomatrix proteins Bassoon and Piccolo via a trans-Golgi compartment. *The Journal of biological chemistry*, *281*(9), 6038–6047.

Dugger, B.N., & Dickson D.W. (2017). Pathology of Neurodegenerative Diseases. *Cold Spring Harbor perspectives in biology* 9(7), a028035.

Gallagher, B. R., & Zhao, Y. (2021). Expansion microscopy: A powerful nanoscale imaging tool for neuroscientists. *Neurobiology of disease*, *154*, 105362.

Gambarotto, D., Zwettler, F. U., Le Guennec, M., Schmidt-Cernohorska, M., Fortun, D., Borgers, S., Heine, J., Schloetel, J. G., Reuss, M., Unser, M., Boyden, E. S., Sauer, M., Hamel, V., & Guichard, P. (2019). Imaging cellular ultrastructures using expansion microscopy (U-ExM). *Nature methods*, *16*(1), 71–74.

Gao, R., Asano, S.M. & Boyden, E.S. (2017). Q&A: Expansion microscopy. *BMC Biol*, 15, 50.

Gao, M., Maraspini, R., Beutel, O., Zehtabian, A., Eickholt, B., Honigmann, A., & Ewers, H. (2018). Expansion Stimulated Emission Depletion Microscopy (ExSTED). *ACS nano*, *12*(5), 4178–4185.

Goedert, M., Spillantini, M.G., Jakes, R., Rutherford, D., Crowther, R.A. (1989). Multiple isoforms of human microtubule-associated protein tau: sequences and localization in neurofibrillary tangles of Alzheimer's disease. *Neuron.* 3(4), 519-26.

Greenberg, S. G., Davies, P., Schein, J. D., & Binder, L. I. (1992). Hydrofluoric acid-treated tau PHF proteins display the same biochemical properties as normal tau. *The Journal of biological chemistry*, *267*(1), 564–569.

Halpern, A. R., Alas, G., Chozinski, T. J., Paredez, A. R., & Vaughan, J. C. (2017). Hybrid Structured Illumination Expansion Microscopy Reveals Microbial Cytoskeleton Organization. *ACS nano*, *11*(12), 12677–12686.

Hansson, O. (2021). Biomarkers for neurodegenerative diseases. *Nat Med.* 27, 954–963.

Hess, S. T., Girirajan, T. P., & Mason, M. D. (2006). Ultra-high resolution imaging by fluorescence photoactivation localization microscopy. *Biophysical journal*, *91*(11), 4258–4272.

Hippius, H., Neundörfer, G. (2003). The discovery of Alzheimer's disease. *Dialogues Clin Neurosci.* 5(1), 101-108.

Hoover, B.R., Reed, M.N., Su, J., Penrod, R.D., Kotilinek, L.A., Grant, M.K., Pitstick, R., Carlson, G.A., Lanier, L.M., Yuan, L.L., Ashe, K.H., Liao, D. (2010). Tau mislocalization to dendritic spines mediates synaptic dysfunction independently of neurodegeneration. *Neuron.* 68(6), 1067-81.

Hou, Y., Dan, X., Babbar, M. et al. (2019). Ageing as a risk factor for neurodegenerative disease. *Nat Rev Neurol* 15, 565–581.

Hunsberger, H.C., Weitzner, D.S., Rudy, C.C., Hickman, J.E., Libell, E.M., Speer, R.R., Gerhardt, G.A., Reed, M.N. (2015). Riluzole rescues glutamate alterations, cognitive deficits, and tau pathology associated with P301L tau expression. *J Neurochem.* 135(2), 381-94.

Iba, M., Guo, J. L., McBride, J. D., Zhang, B., Trojanowski, J. Q., & Lee, V. M. (2013). Synthetic tau fibrils mediate transmission of neurofibrillary tangles in a transgenic mouse model of Alzheimer's-like tauopathy. *The Journal of neuroscience : the official journal of the Society for Neuroscience*, *33*(3), 1024–1037.

Ittner, A., Chua, S. W., Bertz, J., Volkerling, A., van der Hoven, J., Gladbach, A., Przybyla, M., Bi, M., van Hummel, A., Stevens, C. H., Ippati, S., Suh, L. S., Macmillan, A., Sutherland, G., Kril, J. J., Silva, A. P., Mackay, J. P., Poljak, A., Delerue, F., Ke, Y. D., … Ittner, L. M. (2016). Site-specific phosphorylation of tau inhibits amyloid-β toxicity in Alzheimer's mice. *Science* 354(6314), 904-908.

Ittner, A., Ittner, L.M. (2018). Dendritic Tau in Alzheimer's Disease. *Neuron* 99(1), 13-27.

Ittner, L.M., Ke, Y.D., Delerue, F., Bi, M., Gladbach, A., van Eersel, J., Wölfing, H., Chieng, B.C., Christie, M.J., Napier, I.A., Eckert, A., Staufenbiel, M., Hardeman, E., Götz, J. (2010). Dendritic function of tau mediates amyloid-beta toxicity in Alzheimer's disease mouse models. *Cell* 142(3), 387-97.

Jack, C.R. Jr, Knopman, D.S., Jagust, W.J., Petersen, R.C., Weiner, M.W., Aisen, P.S., Shaw, L.M., Vemuri, P., Wiste, H.J., Weigand, S.D., Lesnick, T.G., Pankratz, V.S., Donohue, M.C., Trojanowski, J.Q. (2013). Tracking pathophysiological processes in Alzheimer's disease: an updated hypothetical model of dynamic biomarkers. *Lancet Neurol.* 12(2), 207-16.

Jack, C.R. Jr, Knopman, D.S., Jagust, W.J., Shaw, L.M., Aisen, P.S., Weiner, M.W., Petersen, R.C., Trojanowski, J.Q. (2010). Hypothetical model of dynamic biomarkers of the Alzheimer's pathological cascade. *Lancet Neurol.* 9(1), 119-28.

Jackson, J.S., Witton, J., Johnson, J.D., Ahmed, Z., Ward, M., Randall, A.D., Hutton, M.L., Isaac, J.T., O'Neill, M.J., Ashby, M.C. (2017). Altered Synapse Stability in the Early Stages of Tauopathy. *Cell Rep.* 18(13), 3063-3068.

Jeganathan, S., von Bergen, M., Mandelkow, E.M., Mandelkow, E. (2008). The natively unfolded character of tau and its aggregation to Alzheimer-like paired helical filaments. *Biochemistry* 47(40), 10526-39.

Jicha, G. A., Weaver, C., Lane, E., Vianna, C., Kress, Y., Rockwood, J., & Davies, P. (1999). cAMP-dependent protein kinase phosphorylations on tau in Alzheimer's disease. *The Journal of neuroscience : the official journal of the Society for Neuroscience*, *19*(17), 7486–7494.

Kent, S.A., Spires-Jones, T.L. & Durrant, C.S. (2020). The physiological roles of tau and Aβ: implications for Alzheimer's disease pathology and therapeutics. *Acta Neuropathol* 140, 417–447.

Kimura, T., Whitcomb ,D.J., Jo, J., Regan, P., Piers, T., Heo, S., Brown, C., Hashikawa, T., Murayama, M., Seok, H., Sotiropoulos, I., Kim, E., Collingridge, G.L., Takashima, A., Cho, K. (2013). Microtubule-associated protein tau is essential for long-term depression in the hippocampus. *Philos Trans R Soc Lond B Biol Sci.* 369(1633), 20130144.

Klimas, A., Gallagher, B., & Zhao, Y. (2019). Basics of Expansion Microscopy. *Current protocols in cytometry*, *91*(1), e67.

Kopeikina, K.J., Polydoro, M., Tai, H.C., Yaeger, E., Carlson, G.A., Pitstick, R., Hyman, B.T., Spires-Jones, T.L. (2013). Synaptic alterations in the rTg4510 mouse model of tauopathy. *J Comp Neurol.* 521(6), 1334-53.

Ku, T., Swaney, J., Park, JY. et al. (2016), Multiplexed and scalable super-resolution imaging of three-dimensional protein localization in size-adjustable tissues. *Nat Biotechnol* 34, 973–981.

Ludvigson, A.E., Luebke, J.I., Lewis, J., Peters, A. (2011). Structural abnormalities in the cortex of the rTg4510 mouse model of tauopathy: a light and electron microscopy study. *Brain Struct Funct.* 216(1), 31-42.

Menkes-Caspi, N., Yamin, H.G., Kellner, V., Spires-Jones, T.L., Cohen, D., Stern, E.A. (2015). Pathological tau disrupts ongoing network activity. *Neuron* 85(5), 959-66.

Micheva, K.D., Smith, S.J. (2007). Array tomography: a new tool for imaging the molecular architecture and ultrastructure of neural circuits. *Neuron.* 55(1), 25-36. Erratum in: Neuron. (2007) 55(5), 824.

Miyamoto, T., Stein, L., Thomas, R. et al. (2017). Phosphorylation of tau at Y18, but not tau-fyn binding, is required for tau to modulate NMDA receptor-dependent excitotoxicity in primary neuronal culture. *Mol Neurodegeneration* 12, 41.

Mochizuki, Y., Park, M. K., Mori, T., & Kawashima, S. (1995). The difference in autofluorescence features of lipofuscin between brain and adrenal. *Zoological science,* 12(3), 283–288.

Moreno-García, A., Kun, A., Calero, O., Medina, M., & Calero, M. (2018). An Overview of the Role of Lipofuscin in Age-Related Neurodegeneration. *Frontiers in neuroscience,* 12, 464.

Morozova, O. A., March, Z. M., Robinson, A. S., & Colby, D. W. (2013). Conformational features of tau fibrils from Alzheimer's disease brain are faithfully propagated by unmodified recombinant protein. *Biochemistry,* 52(40), 6960–6967.

Neve, R.L., Harris, P., Kosik, K.S., Kurnit, D.M., Donlon, T.A. (1986). Identification of cDNA clones for the human microtubule-associated protein tau and chromosomal localization of the genes for tau and microtubule-associated protein 2. *Brain Res.* 387(3), 271-80.

Orr, M.E., Sullivan, A.C., Frost, B. (2017). A Brief Overview of Tauopathy: Causes, Consequences, and Therapeutic Strategies. *Trends Pharmacol Sci.* 38(7), 637-648.

Pallas-Bazarra, N., Draffin, J., Cuadros, R et al. (2019). Tau is required for the function of extrasynaptic NMDA receptors. *Sci Rep* 9, 9116.

Park, C. E., Cho, Y., Cho, I., Jung, H., Kim, B., Shin, J. H., Choi, S., Kwon, S. K., Hahn, Y. K., & Chang, J. B. (2020). Super-Resolution Three-Dimensional Imaging of Actin Filaments in Cultured Cells and the Brain *via* Expansion Microscopy. *ACS nano*, *14*(11), 14999–15010.

Perl, D.P. (2010). Neuropathology of Alzheimer's disease.*Mt Sinai J Med.* 77(1):32-42.

Pernal, S.P., Liyanaarachchi, A., Gatti, D.L. et al. (2020). Nanoscale imaging using differential expansion microscopy. *Histochem Cell Biol* 153, 469–480.

Pesce, L., Cozzolino, M., Lanzanò, L., Diaspro, A., & Bianchini, P. (2019). Measuring expansion from macro- to nanoscale using NPC as intrinsic reporter. *Journal of biophotonics,* 12(8), e201900018.

Prince, M.J. (2015). World Alzheimer Report 2015: the global impact of dementia: an analysis of prevalence, incidence, cost and trends (Alzheimer's Disease International). Retrieved from https://www.alzint.org/u/WorldAlzheimerReport2015.pdf.

Ramsden, M., Kotilinek, L., Forster, C., Paulson, J., McGowan, E., SantaCruz, K., Guimaraes, A., Yue, M., Lewis, J., Carlson, G., Hutton, M., Ashe, K.H. (2005). Age-dependent neurofibrillary tangle formation, neuron loss, and memory impairment in a mouse model of human tauopathy (P301L). *J Neurosci.* 25(46), 10637-47.

Regan, P., Piers, T., Yi, J.H., Kim, D.H., Huh, S., Park, S.J., Ryu, J.H., Whitcomb, D.J., Cho, K. (2015). Tau phosphorylation at serine 396 residue is required for hippocampal LTD. *J Neurosci.* 35(12), 4804-12.

Rocher, A.B., Crimins, J.L., Amatrudo, J.M., Kinson, M.S., Todd-Brown, M.A., Lewis, J., Luebke, J.I. (2010). Structural and functional changes in tau mutant mice neurons are not linked to the presence of NFTs. *Exp Neurol.* 223(2), 385-93.

Ross, C., Poirier, M. (2004). Protein aggregation and neurodegenerative disease. *Nat Med.* 10, S10–S17.

Rust, M. J., Bates, M., & Zhuang, X. (2006). Sub-diffraction-limit imaging by stochastic optical reconstruction microscopy (STORM). *Nature methods*, *3*(10), 793–795.

Sadqi, M., Hernández, F., Pan U., Pérez, M., Schaeberle, MD., Ávila J., Muñoz V. (2002). α-Helix Structure in Alzheimer's Disease Aggregates of Tau-Protein. *Biochemistry* 41 (22), 7150-7155.

Saha, P., & Sen, N. (2019). Tauopathy: A common mechanism for neurodegeneration and brain aging. *Mechanisms of ageing and development*, *178*, 72–79.

SantaCruz, K., Lewis, J., Spires, T., Paulson, J., Kotilinek, L., Ingelsson, M., Guimaraes, A., DeTure, M., Ramsden, M., McGowan, E., Forster, C., Yue, M., Orne, J., Janus, C., Mariash, A., Kuskowski, M., Hyman, B., Hutton, M., & Ashe, K. H. (2005). Tau suppression in a neurodegenerative mouse model improves memory function. *Science* 309(5733), 476–481.

Spires, T. L., Orne, J. D., SantaCruz, K., Pitstick, R., Carlson, G. A., Ashe, K. H., & Hyman, B. T. (2006). Region-specific dissociation of neuronal loss and neurofibrillary pathology in a mouse model of tauopathy. *The American journal of pathology*, *168*(5), 1598–1607.

Spires, T.L., Orne, J.D., SantaCruz, K., Pitstick, R., Carlson, G.A., Ashe, K.H., Hyman, B.T. (2006). Region-specific dissociation of neuronal loss and neurofibrillary pathology in a mouse model of tauopathy. *Am J Pathol.* 168(5), 1598-607.

Spires-Jones, T.L., Stoothoff, W.H., de Calignon, A., Jones, P.B., Hyman, B.T. (2009). Tau pathophysiology in neurodegeneration: a tangled issue. Trends Neurosci. 32(3), 150-9.

Hell, SW., & Wichmann, J. (1994). Breaking the diffraction resolution limit by stimulated emission: stimulated-emission-depletion fluorescence microscopy *Opt. Lett.* 19, 780-782.

Tai, H.C., Serrano-Pozo, A., Hashimoto, T., Frosch, M.P., Spires-Jones, T.L., Hyman, B.T. (2012). The synaptic accumulation of hyperphosphorylated tau oligomers in Alzheimer disease is associated with dysfunction of the ubiquitin-proteasome system. *Am J Pathol.* 181(4), 1426-35. Erratum in: *Am J Pathol.* (2012); 181(5), 1889-90.

Terry, R.D., Masliah, E., Salmon, D.P., Butters, N., DeTeresa, R., Hill, R., Hansen, L.A., Katzman, R. (1991). Physical basis of cognitive alterations in Alzheimer's disease: synapse loss is the major correlate of cognitive impairment. *Ann Neurol.* 30(4), 572-80.

Tillberg, P. (2021). Protein-retention expansion microscopy: Improved sub-cellular imaging resolution through physical specimen expansion. *Methods in Cell Biology* 161, 1-14.

Tillberg, P., Chen, F., Piatkevich, K. et al. (2016). Protein-retention expansion microscopy of cells and tissues labeled using standard fluorescent proteins and antibodies. *Nat Biotechnol* 34, 987–992.

Truckenbrodt, S., & Rizzoli, S. O. (2021). Simple multi-color super-resolution by X10 microscopy. *Methods in cell biology*, *161*, 33–56.

Truckenbrodt, S., Maidorn, M., Crzan, D., Wildhagen, H., & Kabatas, S., & Rizzoli, S. (2018). X10 expansion microscopy enables 25-nm resolution on conventional microscopes. *EMBO reports* 19, e45836.

Truckenbrodt, S., Sommer, C., Rizzoli, S.O. et al. (2019). A practical guide to optimization in X10 expansion microscopy. *Nat Protoc* 14, 832–863.

Villemagne, V.L., Pike, K.E., Chételat, G., Ellis, K.A., Mulligan, R.S., Bourgeat, P., Ackermann, U., Jones, G., Szoeke, C., Salvado, O., Martins, R., O'Keefe, G., Mathis, C.A., Klunk, W.E., Ames, D., Masters, C.L., Rowe, C.C. (2011). Longitudinal assessment of Aβ and cognition in aging and Alzheimer disease. *Ann Neurol.* 69(1), 181-92.

Damstra, H., Mohar, B., Eddison, M., Akhmanova, A., Kapitein, LC., Tillberg, PW. (2021) Visualizing cellular and tissue ultrastructure using Ten-fold Robust Expansion Microscopy (TREx). bioRxiv 2021.02.03.428837.

Wassie, A.T., Zhao, Y. & Boyden, E.S. (2019). Expansion microscopy: principles and uses in biological research. *Nat Methods* 16, 33–41.

Weingarten, M.D., Lockwood, A.H., Hwo, S.Y., Kirschner, M.W. (1975). A protein factor essential for microtubule assembly. *Proc Natl Acad Sci U S A.* 72(5), 1858-62.

Wilson, R.S., Leurgans, S.E., Boyle, P.A., Schneider, J.A., & Bennett, D.A. (2010). Neurodegenerative basis of age-related cognitive decline. *Neurology* 75(12), 1070–1078.

Wittenberg, R., Knapp, M., Hu, B. et al. (2019) The costs of dementia in England. *Int J Geriatr Psychiatry.* 34(7), 1095-1103.

Xu, H., Tong, Z., Ye, Q., Sun, T., Hong, Z., Zhang, L., Bortnick, A., Cho, S., Beuzer, P., Axelrod, J., Hu, Q., Wang, M., Evans, S.M., Murre, C., Lu, L., Sun, S., Corbett, K.D., Cang, H. (2019). Molecular organization of mammalian meiotic chromosome axis revealed by expansion STORM microscopy. *Proceedings of the National Academy of Sciences,* 116(37), 18423-18428.

Zempel, H., Thiesm E., Mandelkow, E., Mandelkow, E.M. (2010). Abeta oligomers cause localized Ca(2+) elevation, missorting of endogenous Tau into dendrites, Tau phosphorylation, and destruction of microtubules and spines. *J Neurosci.* 30(36), 11938-50. Erratum in: *J Neurosci. (2012);* 32(17), 6052.

Zhai, R. G., Vardinon-Friedman, H., Cases-Langhoff, C., Becker, B., Gundelfinger, E. D., Ziv, N. E., & Garner, C. C. (2001). Assembling the presynaptic active zone: a characterization of an active one precursor vesicle. *Neuron*, *29*(1), 131–143.

6. Appendix

Protocol for Protein Retention Expansion Microscopy

This protocol describes the expansion of 100 μm fixed mouse brain tissue sections post-immunolabelling, and is adapted from Asano et al, 2018.

Materials

Table 2.1: List of reagents used for ProExM

24 x 50 mm No. 1.5 coverslips (Fisher Scientific, #NC1034527)

3D printer (optional)

64x48 mm glass coverslips (Agar Scientific, #AGL464864-15)

6-well plate (ThermoFisher, #140675)

Laboratory incubator

Low melting point agarose (Sigma-Aldrich, #A4018-100G)

Microcentrifuge tubes (ThermoFisher, #69715)

Microscope slides (VWR, #631-1553P)

Paintbrush

Parafilm (Sigma-Aldrich, #P7793-1EA)

Petri dishes (Fisher Scientific, #11901518)

Razor blade

Silicon grease (if using 3D printer)

Preparation

1. Dissolve 5 mg Acryloyl-X SE (AcX) in 500 μl anhydrous dimethylsulfoxide (DMSO) and store as 20 μl aliquots with drying agents at -20 °C.
2. Prepare the monomer solution using 23.9% sodium acrylate (38 g/100 ml), 5.3% acrylamide (50 g/100 ml), 8.0% N,N'-methylenebisacrylamide (2 g/100 ml), 42.6% sodium chloride (5 M), 10.6% 10X PBS (1 M), and 9.6% deionised water. Store this solution as 1 ml aliquots at -20 °C.

3. Prepare the digestion buffer using 0.5% Triton X-100, 0.2% EDTA (0.5 M, pH 8), 5% Tris.Cl (1 M, pH 8), 4.7% NaCl, and deionised water. For example, to make up 100 ml of digestion buffer, use 0.5 g Triton X-100, 0.2 ml EDTA, 5 ml Tris.Cl, 4.676 g NaCl, and top up to 100 ml total volume using deionised water. Store as 1.5 ml aliquots at -20 °C.

4. If using gelling and imaging chambers as described in 2.3, these need to be designed and 3D printed in advance. For this protocol, gelling chambers were designed to contain 2 wells (12*10*0.3 mm) (Figure 2.1.A). For imaging chambers, this protocol used 3D chambers with external dimensions of 64*48*2 mm and internal dimensions of 63x47x2 mm to fit over 64*48 mm glass coverslips (Figure 2.1.C-D). If a 3D printer is not available, other methods of constructing gelling chambers and imaging expanded tissue samples are described in Asano et al, 2018 and Tillberg, 2021.

Gelation

5. Following tissue preparation and immunolabelling, replace PBS used to store tissue slices (i.e. in a 6 well plate) with 0.1 mg/ml Acryloyl-X SE in 0.1 M PBS (1:100 dilution) and leave overnight in the dark (>6hrs) at RT.

6. Wash tissue slices with 0.1 M PBS 2 x 15mins.

7. To assemble the gelling chamber, adhere the 3D printed chamber to a microscope slide using silicon grease. Additionally, coat a glass coverslip in a thin even layer of parafilm which will be used as a lid to seal the chamber (Figure 2.2.).

8. In a 1.5 ml microcentrifuge tube on ice, prepare gelling solution as a ratio of 47:1:1:1 monomer solution, TEMED (10 g/100 ml), 4-HT (0.5 g/100 ml), and APS (10 g/100 ml). For example, 1 ml of gelling solution would be comprised of 940 µl monomer solution, 20 µl TEMED, 20 µl 4-HT , 20 µl APS, but this can be scaled as appropriate. It is important to add TEMED, 4-HT and APS to the monomer solution in this order to prevent premature gelation of the solution. This process should be completed in <5 minutes.

9. Transfer the tissue slice to this microcentrifuge tube and keep at 4 °C and on ice for 20 minutes to allow the solution to perfuse the tissue. Agitate the solution regularly (~every 5 minutes) (Figure 2.2.A).

10. Pipette 20 µl of gelling solution from the microcentrifuge tube into the well of the gelling chamber (Figure 2.2.B).

11. Transfer the tissue into the chamber using a paintbrush, ensuring the bottom surface of the tissue is evenly coated in gelling solution.

12. Pipette 40 µl, or the volume that is required to fill a custom chamber fully, of gelling solution onto the tissue slice within the well of the chamber.

13. Place the gelling chamber lid over the sample carefully ensuring no air bubbles form over the embedded tissue slice (Figure 2.2.C).

14. Transfer the sealed gelling chambers to an incubator (37 °C) for 2 hours to facilitate gel polymerisation.

Digestion

15. Dilute Proteinase K 1:100 in digestion buffer and pipette 2 ml of this dilution into the wells of a 6-well plate.
16. Remove the lid of the gelling chamber using a razor blade, and then disassemble the gelling chamber from the microscope slide that it is adhered to.
17. Place a small volume of this digestion solution on the sample gel using a paintbrush to detach the sample gel from the microscope slide.
18. Transfer the sample gel to the 6-well plate containing the Proteinase K dilution using a paintbrush, and leave the gel-tissue complex in the digestion solution overnight in the dark, approximately 16 hours, at RT and on a shaker at 20 rpm.

Expansion

19. Post-digestion, the sample should appear ~1.5x its original size (Figure 2.1.B). Remove the digestion solution from the well of the 6-well plate using a pipette and replaced with 0.1 M PBS.
20. When ready to begin the expansion, use a coverslip and paintbrush to carefully transfer the gel to a petri dish containing deionised water. Replace the deionised water in the petri dish using a pipette every 20 minutes for 1 hour. During this stage, the tissue embedded within the gel will become almost completely transparent (Figure 2.1.C).
21. Whilst performing step 20, construct imaging chambers by adhering 3D-printed chambers to 64x48 mm glass coverslips using silicon grease.

Imaging

22. Use a 64x48 mm glass coverslip and paintbrush to transfer the expanded gel into an imaging chamber. Remove any water transferred into the imaging chamber using a pipette.
23. Fill the surrounding space in the imaging chamber with 2% low melting point agarose that has cooled and set slightly. Seal the imaging chamber using a 64x48 mm glass coverslip (Figure 2.1.D).
24. Use a water droplet between the objective lens and the surface of the imaging chamber if index matching to a water immersive objective (which is optimal to use for imaging expanded hydrogels that are >99% water). Working distance for imaging the expanded sample can be optimised by having a chamber with two glass faces that can be flipped over to allow the gel sample to be imaged from both sides.